

Searches for Magnetic Monopoles and  
Highly Ionising Particles at  $\sqrt{s} = 13$  TeV  
at the LHC with MoEDAL

by

Ameir Shaa

A thesis submitted in partial fulfillment of the requirements  
for the degree of

Doctor of Philosophy

Department of Physics  
University of Alberta

# Abstract

The standard model of particle physics describes the experimental data collected to date remarkably well. However, this theory (the standard model of particle physics) does not provide a complete description of reality. What is dark matter and what is the origin of dark matter? How do we explain the hierarchy between the masses of the elementary particles? Is it possible to describe all the interactions in a coherent way within the same theory? Why is there an asymmetry between electricity and magnetism? Why is there an asymmetry between matter and anti-matter? These are some of the fundamental questions left unanswered by the standard model. Many new physical theories, such as supersymmetry, have been proposed to answer these questions, but they need to be experimentally verified.

Built in a 27km tunnel at CERN in Geneva, Switzerland, the Large Hadron Collider (LHC) accelerated and collided beams of protons with a center of mass energy of 13TeV (with a luminosity of  $6.46\text{fb}^{-1}$  at Interaction Point 8) in 2018. These high impact collisions enable us to study the structure of matter at its fundamental. In particular, they enable the production of massive particles that were previously inaccessible to us.

In this report, the data of the MoEDAL detectors at the LHC are exploited to search for a certain class of particles whose existence is predicted by certain theories: highly ionizing particles (HIPs) that is to say particles whose lifetime is long enough to leave a trace in the detector along their trajectory.

---

Although this research is designed to be sensitive to different types of HIPs in a generic way, the discovery or exclusion of particles that carry a fundamental magnetic charge, called magnetic monopoles, is the major objective of this report. The magnetic monopole was postulated by Paul Dirac in 1931 [1] as an elegant way to explain quantization of electric charge, among other virtues. One of the results of the Dirac calculations is that the fundamental unit of magnetic charge must correspond to many electrical charge units and the expected signature of a monopole in a detector is therefore a loss of energy by very high ionization along its trajectory. The presence of monopoles is scanned every time a new particle collider is built. With the LHC, we have the opportunity to explore the multi-TeV energy regime for the first time.

In this thesis, new simulations have been developed to emulate and understand the detector response to highly ionizing particles. MoEDAL uses an array of Magnetic Monopole Trappers (MMTs) and Nuclear Track Detectors (NTDs) to trap and track these monopoles respectively and this method is used to distinguish the signals of new physics at the LHC.

With MoEDAL, an unprecedented concept called the monopole trap was designed to specifically look for the magnetic monopoles produced in LHC collisions. The idea is unconventional, but very simple: Aluminum bars placed near an LHC interaction point (in the LHCb experiment cavern at Interaction Point 8) are exposed to collisions before being transported to a Laboratory in Zurich to detect the presence of magnetic charges trapped with a superconducting magnetometer. In a way that is unique, the trapped monopole would be transportable and its properties can be studied in much detail.

---

# Preface

This thesis is exclusively based on work completed for the MoEDAL (the Monopole and Exotics Detector at the LHC) experiment at CERN for which my supervisor, James Pinfold, is the spokesperson.

The analyses presented in Chapter 3 of this thesis is my own original work with the exception of the etching and scanning of the Nuclear Track Detectors which was done by the Bologna group led by Laura Patrizii. The results for 3.3 and 3.4 have been published in [2] and [3] respectively.

The model implementation of HIPs into MadGraph5 were written by myself originally and updated by Stephanie Baines, Arka Santra, James Pinfold, Nick Mavramatos and Vasiliki Mitsou.

---

to my mother and father who taught me the importance of  
seeking knowledge

---

# Acknowledgements

Many thanks to my supervisor James Pinfold without whom my PhD would not have been possible. Many thanks for believing in me from the start and being so enthusiastic about me joining the MoEDAL collaboration when I was only 22 years of age. Your support and constant encouragement has helped shaped me into a better academic as well as this unique thesis. I am grateful you trusted me to take the lead on many different projects and analyses and you always trusted my input and decision-making. For thoroughly reading my thesis, your valuable insights, the hours we spent conversing in your office, making me feel welcome in Edmonton and many other things, I am eternally grateful.

My deepest gratitude to Albert De Roeck for introducing MoEDAL, taking me under his tutelage and providing the impetus for much learning and discussion from a topic, wrought with difficulty, I did not foresee during my undergraduate years.

Many thanks to Phillipe Mermod for the many insightful discussions, feedback, clarification and most importantly, clearing misconceptions and enforcing details in the reasoning process thus allowing me to gain further insight into the analysis techniques in HEP.

Many thanks to Marc de Montigny, my co-supervisor, who has been nothing but encouraging and providing me with funding so that my time could be better spent on research. I am extremely grateful for all that you have done for me.

---

I would also like to thank Veronique Wedlake from CERN for all the administrative help and making my stay at CERN as smooth as possible.

I would also like to extend my gratitude to CERN, the CN Yang Scholars' Programme and Nanyang Technological University for sparking the interest in research and particle physics in me. You have ignited a flame that is inextinguishable.

Many thanks to my parents who supported me throughout this journey which started when I was an undergraduate. Your support and love is what made this PhD and for that I am eternally grateful.

Many thanks to my sisters, Amira, Aisha and Fatimah who provided me with constant encouragement, support, laughter and love. I am blessed to have siblings like you.

To my best friend Afiah who was my rock to lean on for the past four years - I thank you. You showered me with love, care, concern, friendship and laughter. Your presence has been an immense source of blessings in my life and without you, this PhD would not have been possible. I am eternally grateful for all that you have done for me.

Many thanks to my oldest friend Prasanth. FIFA nights with you were some of the best memories I have during this journey where we eat and talk about anything and everything under the sun. I am forever thankful.

Lastly, to Farah and Farid, my cats - your presences have been nothing short of angelic and your faces are able to brighten up even the darkest of days. The both of you are sources of blessings for which I am immensely thankful.

---

# Contents

<b>Abstract</b>	<b>ii</b>
<b>Preface</b>	<b>iv</b>
<b>Dedication</b>	<b>v</b>
<b>Acknowledgements</b>	<b>vi</b>
<b>Contents</b>	<b>xi</b>
<b>List of Tables</b>	<b>xii</b>
<b>List of Figures</b>	<b>xxi</b>
<b>List of Abbreviations</b>	<b>xxii</b>
<b>List of Symbols</b>	<b>xxiii</b>
<b>Territorial Acknowledgement</b>	<b>xxv</b>
<b>1 Introduction</b>	<b>1</b>
1.1 Magnetic Monopoles . . . . .	1
1.2 Dirac Monopoles . . . . .	4
1.2.1 Classical Solution . . . . .	4
1.2.2 Quantum Mechanical Solution . . . . .	7
1.3 The Schwinger Monopole . . . . .	13

1.4	Monopole-Photon Coupling . . . . .	14
1.5	Monopoles in Electroweak Models . . . . .	15
1.5.1	Topologically Stable Finite Energy Electroweak Monopoles . . . . .	15
1.5.2	The Dirac Quantisation Condition and the Weak Mixing Angle . . . . .	17
1.6	The Cho-Maison Monopole . . . . .	20
1.7	The Nambu Monopole . . . . .	26
1.8	Matter Interactions . . . . .	29
1.9	Energy Loss via Ionisation of the Medium . . . . .	30
1.10	Detection Techniques . . . . .	32
1.11	Heavily Etched Nuclear Track Detectors . . . . .	33
1.12	Monopoles Trapped in Matter . . . . .	34
1.13	Observations of Monopole-Like Events . . . . .	36
1.14	Searches for Cosmological Monopoles . . . . .	38
1.15	Monopoles in Bound Matter Searches . . . . .	42
1.16	Searches for Monopoles at Colliders . . . . .	44
<b>2</b>	<b>The Large Hadron Collider and MoEDAL</b>	<b>47</b>
2.1	The Large Hadron Collider . . . . .	47
2.2	The MoEDAL Detector . . . . .	50
2.2.1	Nuclear Track Detectors . . . . .	51
2.2.2	Magnetic Monopole Trappers . . . . .	53
2.2.3	TimePix . . . . .	55
2.2.4	Conclusion . . . . .	56
<b>3</b>	<b>Searches in MOEDAL</b>	<b>57</b>
3.1	Magnetometer Measurements . . . . .	57
3.1.1	Calibration of Magnetometer . . . . .	58
3.1.2	Expected Magnetometer Response to Monopoles . . . . .	59

---

3.1.3	MMT samples . . . . .	60
3.2	Simulations at MoEDAL . . . . .	64
3.2.1	Event Generation . . . . .	64
3.2.2	Monopole Models in MadGraph5 . . . . .	65
3.2.3	Simulating the Energy Loss of Monopoles . . . . .	65
3.2.4	Simulation of Trapping Monopoles . . . . .	66
3.2.5	MMT Trapping Acceptances . . . . .	66
3.2.6	NTD Acceptances . . . . .	66
3.3	Full Analysis of LHC Run 1 Data . . . . .	69
3.3.1	Introduction . . . . .	69
3.3.2	Theory . . . . .	70
3.3.3	The MoEDAL Detector . . . . .	74
3.3.4	HIP Energy Loss in MoEDAL . . . . .	74
3.3.5	The MMT Detector . . . . .	75
3.3.6	Calibration of the MMT detector . . . . .	76
3.3.7	The Nuclear Track Detector System . . . . .	77
3.3.8	The Etching Procedure . . . . .	78
3.3.9	Calibration of the NTD Detector . . . . .	79
3.3.10	Etching and Scanning of MoEDAL NTD . . . . .	80
3.3.11	The Makrofol Detection Threshold . . . . .	83
3.3.12	Efficiency and False Positives in the NTD Detectors . . . . .	85
3.3.13	Acceptance of the LHC Run-1 MoEDAL Detector . . . . .	87
3.3.14	Analysis Results . . . . .	95
3.3.15	Conclusions . . . . .	101
3.4	The Search for Dyons . . . . .	103
3.4.1	Introduction . . . . .	103
3.4.2	Theory . . . . .	104

---

3.4.3	Detection of Dyons in MoEDAL . . . . .	107
3.4.4	Acceptance of the Run-2 MoEDAL MMT Sub-Detector . . . . .	114
3.4.5	Analysis Results . . . . .	119
3.4.6	Conclusions . . . . .	127
<b>4</b>	<b>Conclusion</b>	<b>129</b>
	<b>Bibliography</b>	<b>146</b>
<b>5</b>	<b>Appendices</b>	<b>147</b>
5.1	Full Analysis of LHC Run 1 Data . . . . .	148
5.1.1	HECO Acceptance Plots . . . . .	148
5.1.2	Monopole Acceptance Plots . . . . .	150
5.2	The Search for Dyons . . . . .	151
5.2.1	Dyon Acceptance Plots . . . . .	151

# List of Tables

3.1	Etching Conditions of Makrofol . . . . .	79
3.2	95% CL mass limits for HECO Pair Direct Production during Run-1 LHC $p - p$ Collisions, Assuming $\beta$ -Independent Couplings . . . . .	100
3.3	95% CL mass limits for Monopole Pair Direct Production during Run-1 LHC $p - p$ Collisions, Assuming $\beta$ -Independent Couplings . . . . .	100
3.4	95% C.L. Mass Limits Found in a Drell-Yan Production Model for Spin-0, Spin- $\frac{1}{2}$ and Spin-1 Dyon Pair Direct Production in LHC $p - p$ Collisions, Assuming $\beta$ -Independent Couplings . . . . .	127

# List of Figures

2.1	CERN Accelerator Complex . . . . .	48
2.2	A GEANT-4 Panoramix view of the MoEDAL detector prototype deployed at IP8 during LHC's Run-1. . . . .	51
2.3	A GEANT-4 Panoramix view of the MoEDAL detector deployed at IP8 during LHC's Run-2. . . . .	52
2.4	NTD module composition . . . . .	53
2.5	A photograph of the prototype MMT detector deployed at IP8. . . . .	54
3.1	Top: schematic representation of the magnetometer used in this work. Bottom: magnetic field configuration of pseudopole near two superconducting pick-up coils . . . . .	58
3.2	Top: persistent current (in units of $g_D$ after application of a calibration constant) after first passage through the magnetometer for all samples. Bottom: results of repeated measurements of candidate samples with absolute measured values in excess of $0.4g_D$ . . . . .	60
3.3	Tree level Feynman diagram for DY production (top) of HIP/anti-HIP pairs and (bottom) Spin- $\frac{1}{2}$ HECO/anti-HECO pairs. . . . .	73
3.4	Restricted Energy Loss in Makrofol for monopoles of different magnetic charge. The horizontal dashed line indicates the Makrofol detection threshold. . . . .	75

3.5	Restricted Energy Loss in Makrofol for HECOs of different electric charge. The horizontal dashed line indicates the Makrofol detection threshold. . . . .	76
3.6	Illustration of the track-etch technique: a) latent track forming along the trajectory of a high ionizing particle impinging perpendicularly on the NTD surface ; b) development of conical pits during the etching process; c) etch-pits joining after a prolonged etching, forming a hole in the detector. . . . .	78
3.7	Microphotographs of relativistic $\text{Pb}^{82+}$ tracks and of nuclear fragments ( $Z < 82$ ) in two consecutive foils of Makrofol. Each image frame measures $0.64\text{mm} \times 0.80\text{mm}$ . Etch-pits are from the same ions crossing the detector foils: (left) Makrofol foil etched in "strong conditions"; (right) Makrofol foil etched in "soft conditions". Note that the microphotographs also show two clearly differentiated fragmentation products of Pb: La ( $Z = 57$ ); and, Pm ( $Z = 61$ ). . . . .	79
3.8	Distribution of track surface areas in Makrofol exposed to 158A GeV $\text{Pb}^{82+}$ and etched in soft conditions [4]. . . . .	81
3.9	Reduced etch-rate ( $p$ ) versus REL for Makrofol exposed to relativistic Lead and Xenon ion beams: (top) detectors etched in soft conditions; (bottom) detectors etched in strong conditions. The upper and low curves are drawn through the $\pm 1\sigma$ value of the error on each $p$ value, where the error bars represent a convolution of the statistical and systematic errors on each point. . . . .	82
3.10	The maximum angle to the normal of the NTD plane within which the HIP will be detected. . . . .	84
3.11	Calibration Curve for $p$ vs REL similar to the bottom of Figure 3.9 . . . . .	85
3.12	Acceptance for Spin-0, Spin- $\frac{1}{2}$ and Spin-1 HECOs with charge $125e$ . . . . .	88
3.13	Acceptance for Spin-0, Spin- $\frac{1}{2}$ and Spin-1 Monopole Pair Production with Magnetic Charge $2g_D$ . . . . .	88

3.14	The coordinate system used in the analysis . . . . .	90
3.15	The $\theta$ , $\phi$ , momentum and $\eta$ distributions for Spin-0 HECOs of mass 100GeV and electric charge 50e, produced via the DY process via virtual photon exchange. In each case, 60K events were originally generated. The plots are normalized to the maximum amplitude. The blue histogram represents generated events and the underlying orange histogram shows the distribution of selected events. . . . .	91
3.16	The $\theta$ , $\phi$ , momentum and $\eta$ distributions for Spin- $\frac{1}{2}$ HECOs of mass 100GeV and electric charge 50e, produced via the DY process via virtual photon exchange. In each case, 60K events were originally generated. The plots are normalized to the maximum amplitude. The blue histogram represents generated events and the underlying orange histogram shows the distribution of selected events. . . . .	91
3.17	The $\theta$ , $\phi$ , momentum and $\eta$ distributions for Spin-1 HECOs of mass 100GeV and electric charge 50e, produced via the DY process via virtual photon exchange. In each case, 60K events were originally generated. The plots are normalized to the maximum amplitude. The blue histogram represents generated events and the underlying orange histogram shows the distribution of selected events. . . . .	92
3.18	The $\theta$ , $\phi$ , momentum and $\eta$ distributions for Spin- $\frac{1}{2}$ HECOs of mass 100GeV and electric charge 50e, produced via the DY process via virtual photon and $Z^0$ exchange. In each case, 60K events were originally generated. The plots are normalized to the maximum amplitude. The blue histogram represents generated events and the underlying orange histogram shows the distribution of selected events. . . . .	92

- 
- 3.19 The  $\theta$ ,  $\phi$ , momentum and  $\eta$  distributions for Spin-0 monopoles of mass 1000GeV and electric charge  $1g_D$ , produced via the DY process via virtual photon exchange for the NTD detector. In each case, 60K events were originally generated. The plots are normalized to the maximum amplitude. The blue histogram represents generated events and the underlying orange histogram shows the distribution of selected events. 93
- 3.20 The  $\theta$ ,  $\phi$ , momentum and  $\eta$  distributions for Spin- $\frac{1}{2}$  monopoles of mass 1000GeV and electric charge  $1g_D$ , produced via the DY process via virtual photon exchange for the NTD detector. In each case, 60K events were originally generated. The plots are normalized to the maximum amplitude. The blue histogram represents generated events and the underlying orange histogram shows the distribution of selected events. 93
- 3.21 The  $\theta$ ,  $\phi$ , momentum and  $\eta$  distributions for Spin-1 monopoles of mass 1000GeV and electric charge  $1g_D$ , produced via the DY process via virtual photon exchange for the NTD detector. In each case, 60K events were originally generated. The plots are normalized to the maximum amplitude. The blue histogram represents generated events and the underlying orange histogram shows the distribution of selected events. 94
- 3.22 The  $\theta$ ,  $\phi$ , momentum and  $\eta$  distributions for Spin-0 monopoles of mass 1000GeV and electric charge  $1g_D$ , produced via the DY process via virtual photon exchange for the MMT detector. In each case, 60K events were originally generated. The plots are normalized to the maximum amplitude. The blue histogram represents generated events and the underlying orange histogram shows the distribution of selected events. 94

3.23	The $\theta$ , $\phi$ , momentum and $\eta$ distributions for Spin- $\frac{1}{2}$ monopoles of mass 1000GeV and electric charge $1g_D$ , produced via the DY process via virtual photon exchange for the MMT detector. In each case, 60K events were originally generated. The plots are normalized to the maximum amplitude. The blue histogram represents generated events and the underlying orange histogram shows the distribution of selected events.	95
3.24	The $\theta$ , $\phi$ , momentum and $\eta$ distributions for Spin-1 monopoles of mass 1000GeV and electric charge $1g_D$ , produced via the DY process via virtual photon exchange for the MMT detector. In each case, 60K events were originally generated. The plots are normalized to the maximum amplitude. The blue histogram represents generated events and the underlying orange histogram shows the distribution of selected events.	95
3.25	95% CL mass limits in a DY production model of Spin-0, Spin- $\frac{1}{2}$ and Spin-1 HECO pair direct production in LHC $p - p$ collisions. . . . .	99
3.26	95% CL mass limits in a DY production model of Spin-0, Spin- $\frac{1}{2}$ and Spin-1 monopole pair direct production in LHC $pp$ collisions. . . . .	100
3.27	A Feynman-like diagram for the benchmark Drell-Yan mechanism used in direct dyon-dyon pair production at leading order. In the eikonal approximation, which is applicable for LHC energy, the coupling $g'$ is given by $\sqrt{g^2 + q^2}$ . . . . .	105
3.28	Results of the calibration measurements with the superposition method using a magnetic dipole sample, and the solenoid method with $P = 32.4g_D\mu\text{A}^{-1}$ and various currents. The dashed lines represent the expected plateau values in units of Dirac charge. The calibration constant is tuned using the measurement from the superposition method. . . .	110
3.29	Magnetic pole strength (in units of Dirac charge) measured in the 2400 aluminum samples of the MoEDAL trapping detector exposed to 13TeV collisions in 2015 – 2017, with every sample scanned twice. . . . .	111

3.30	Results of multiple pole strength measurements (in units of Dirac charge) for the 87 candidate samples for which at least one of the two first measurement values was above the threshold $ g  > 0.4g_D$ . More values are observed below threshold than above threshold for all of them, excluding the presence of a monopole with $ g  > g_D$ . . . . .	112
3.31	Acceptance for Spin-0, Spin- $\frac{1}{2}$ and Spin-1 Dyons with Magnetic Charge $1g_D$ and Electric Charges $25e$ . . . . .	115
3.32	Acceptance for Spin-0, Spin- $\frac{1}{2}$ and Spin-1 Dyons with Magnetic Charge $1g_D$ and Electric Charges $50e$ . . . . .	116
3.33	The $\theta$ , $\phi$ , momentum and $\eta$ distributions for Spin-0 HECOs of mass $1000\text{GeV}$ and electric charge $0e$ , produced via the DY process via virtual photon exchange. In each case, 60K events were originally generated. The plots are normalized to the maximum amplitude. The blue histogram represents generated events and the underlying orange histogram shows the distribution of selected events. . . . .	117
3.34	The $\theta$ , $\phi$ , momentum and $\eta$ distributions for Spin- $\frac{1}{2}$ HECOs of mass $1000\text{GeV}$ and electric charge $0e$ , produced via the DY process via virtual photon exchange. In each case, 60K events were originally generated. The plots are normalized to the maximum amplitude. The blue histogram represents generated events and the underlying orange histogram shows the distribution of selected events. . . . .	117
3.35	The $\theta$ , $\phi$ , momentum and $\eta$ distributions for Spin-1 HECOs of mass $1000\text{GeV}$ and electric charge $0e$ , produced via the DY process via virtual photon exchange. In each case, 60K events were originally generated. The plots are normalized to the maximum amplitude. The blue histogram represents generated events and the underlying orange histogram shows the distribution of selected events. . . . .	118

3.36	The $\theta$ , $\phi$ , momentum and $\eta$ distributions for Spin-0 HECOs of mass 1000GeV and electric charge $0e$ , produced via the DY process via virtual photon exchange. In each case, 60K events were originally generated. The plots are normalized to the maximum amplitude. The blue histogram represents generated events and the underlying orange histogram shows the distribution of selected events. . . . .	118
3.37	The $\theta$ , $\phi$ , momentum and $\eta$ distributions for Spin- $\frac{1}{2}$ HECOs of mass 1000GeV and electric charge $0e$ , produced via the DY process via virtual photon exchange. In each case, 60K events were originally generated. The plots are normalized to the maximum amplitude. The blue histogram represents generated events and the underlying orange histogram shows the distribution of selected events. . . . .	119
3.38	The $\theta$ , $\phi$ , momentum and $\eta$ distributions for Spin-1 HECOs of mass 1000GeV and electric charge $0e$ , produced via the DY process via virtual photon exchange. In each case, 60K events were originally generated. The plots are normalized to the maximum amplitude. The blue histogram represents generated events and the underlying orange histogram shows the distribution of selected events. . . . .	119
3.39	Cross-section upper limits at 95% C.L. for DY Spin-0 Dyon-Pair Production, with magnetic charges $1g_D - 2g_D$ and multiple electric charges, in 13TeV $p - p$ collisions. The solid lines are leading-order cross-section calculations. . . . .	121
3.40	Cross-section upper limits at 95% C.L. for DY Spin-0 dyon-pair production, with magnetic charges $3g_D - 4g_D$ and multiple electric charges, in 13TeV $p - p$ collisions. The solid lines are leading-order cross-section calculations. . . . .	122

3.41	Cross-section upper limits at 95% C.L. for DY Spin- $\frac{1}{2}$ Dyon-Pair Production, with magnetic charges $1g_D - 2g_D$ and multiple electric charges, in 13TeV $p-p$ collisions. The solid lines are leading-order cross-section calculations. . . . .	123
3.42	Cross-section upper limits at 95% C.L. for DY Spin- $\frac{1}{2}$ dyon-pair production, with magnetic charges $3g_D - 5g_D$ and multiple electric charges, in 13TeV $p-p$ collisions. The solid lines are leading-order cross-section calculations. . . . .	124
3.43	Cross-section upper limits at 95% C.L. for DY Spin-1 Dyon-Pair Production, with magnetic charges $1g_D - 2g_D$ and multiple electric charges, in 13TeV $p-p$ collisions. The solid lines are leading-order cross-section calculations. . . . .	125
3.44	Cross-section upper limits at 95% C.L. for DY Spin-1 dyon-pair production, with magnetic charges $3g_D - 4g_D$ and multiple electric charges, in 13TeV $p-p$ collisions. The solid lines are leading-order cross-section calculations. . . . .	126
3.45	Cross-section upper limits at 95% C.L. for DY Spin-1 dyon-pair production, with magnetic charge $5g_D$ and multiple electric charges, in 13TeV $p-p$ collisions. The solid lines are leading-order cross-section calculations. . . . .	126
5.1	Run-1 HECO Acceptance Plots for Electric Charges 15e – 100e . . . .	148
5.2	Run-1 HECO Acceptance Plots for Electric Charges 125e – 175e . . . .	149
5.3	Run-1 Monopole Acceptance Plots for Magnetic Charges $1g_D - 4g_D$ . . . .	150
5.4	Run-2 Dyon Acceptance Plots for Magnetic Charge $1g_D$ and Electric Charges 0e – 20e . . . . .	151
5.5	Run-2 Dyon Acceptance Plots for Magnetic Charge $1g_D$ and Electric Charges 25e – 400e . . . . .	152

---

5.6	Run-2 Dyon Acceptance Plots for Magnetic Charge $2g_D$ and Electric Charges $0e - 20e$ . . . . .	153
5.7	Run-2 Dyon Acceptance Plots for Magnetic Charge $2g_D$ and Electric Charges $25e - 400e$ . . . . .	154
5.8	Run-2 Dyon Acceptance Plots for Magnetic Charge $3g_D$ and Electric Charges $0e - 20e$ . . . . .	155
5.9	Run-2 Dyon Acceptance Plots for Magnetic Charge $3g_D$ and Electric Charges $25e - 400e$ . . . . .	156
5.10	Run-2 Dyon Acceptance Plots for Magnetic Charge $4g_D$ and Electric Charges $0e - 20e$ . . . . .	157
5.11	Run-2 Dyon Acceptance Plots for Magnetic Charge $4g_D$ and Electric Charges $25e - 400e$ . . . . .	158
5.12	Run-2 Dyon Acceptance Plots for Magnetic Charge $5g_D$ and Electric Charges $0e - 20e$ . . . . .	159
5.13	Run-2 Dyon Acceptance Plots for Magnetic Charge $5g_D$ and Electric Charges $25e - 400e$ . . . . .	160
5.14	Run-2 Dyon Acceptance Plots for Magnetic Charge $6g_D$ and Electric Charges $0e - 50e$ . . . . .	161

# List of Abbreviations

This is the list of all the abbreviations from this thesis.

LHC	Large Hadron Collider
QFT	Quantum Field Theory
QED	Quantum Electrodynamics
QCD	Quantum Chromodynamics
SM	Standard Model
LO	Leading Order (in quark mass)
NLO	Next-to-Leading Order (in quark mass)
NNLO	Next-to-Next-to-Leading Order (in quark mass)
FF	Form Factor(s)
LL	Leading Log, referring to the double logarithmic contribution
NLL	Next-to-Leading (subleading) Log, referring to the single logarithmic contribution
nL	n-loop diagram(s)

# List of Symbols

This is the list of frequently used symbols in this thesis.

$d$	dimension of spacetime, $d = 4 - 2\epsilon$ in dimensional regularization
$\epsilon$	dimension regularization parameter
$g_{\mu\nu}$	The metric tensor
$l_i, k_i, k'_i$	Loop momenta
$p_i$	Incoming particle momenta
$q$	Momentum transfer/Outgoing momentum
$m_q \equiv m$	Mass of the ( <i>i</i> ) scattering quark or ( <i>ii</i> ) quark in the loop
$m_H$	Mass of the Higgs Boson
$\rho$	The expansion parameter in the High energy limit, $\rho = m^2/q^2$
$u_i, v_i$	Sudakov parameters
$S(l)$	Feynman Propagator for a fermion carrying momentum ' <i>l</i> '
$D_{\mu\nu}(l)$	Gauge Boson propagator with momentum ' <i>l</i> '
$\alpha, \beta, \dots$	Greek letters designating the spacetime indices at a vertex

---

$a, b, \dots$	Latin alphabets indicating Color indices
$F_i$	Dirac and Pauli FF for $i = 1, 2$ respectively
$F_S$	Scalar FF for quark scattering
$M_{ggH}^q$	Higgs production FF
$y_q$	Quark Yukawa coupling
$SU(N_c)$	Special Unitary group, $N_c = 3$ for QCD
$C_F$	Quadratic Casimir of the fundamental representation
$C_A$	Quadratic Casimir of the Adjoint representation
$g_s$	The strong coupling appearing in the QCD Lagrangian and Vertices
$\alpha_s$	The strong coupling constant, $\alpha_s = g_s^2/(4\pi)$
$e$	Positron charge and QED Lagrangian Coupling
$p_i p_j$	Scalar (dot) product of the 4-momentum $p_i$ and $p_j$
$x = \frac{\alpha}{4\pi} \ln^2 \rho$	Double log variable
$z = (C_A - C_F)x$	Double log variable with standard eikonal color charge

## Territorial Acknowledgement

The University of Alberta, its campus, all the buildings, and research facilities as well as the place I have called home during my time in Edmonton, are all located on traditional territories of the Indigenous people of Canada. These lands are known part of Alberta Treaties 6, 7 and 8, and are the homeland to the Indigenous communities such as Blackfoot, Cree, Dene, Inuit, Iroquios, Métis, Nakota Sioux and Ojibway/Saulteaux/Anishinaabe Nations. All of us at the University respectfully acknowledge these lands and the sovereignty, histories, languages and cultures of all the First Nations who have thrived here for centuries and continue to be vital part of the modern multicultural community.

# Chapter 1

## Introduction

*"Maybe you are searching among the branches, for what only appears in the roots."* -  
Jalaluddin Rumi

### 1.1 Magnetic Monopoles

The electromagnetic fields and electrically charged particle dynamics are described by the classical theory of electromagnetism. The Maxwell's equations, created by James Clerk-Maxwell and published in 1873, describe these dynamics perfectly. The equations of Maxwell are,

$$\vec{\nabla} \cdot \vec{E} = \frac{\rho_e}{\epsilon} \quad (1.1)$$

$$\vec{\nabla} \times \vec{E} = -\frac{\partial \vec{B}}{\partial t} \quad (1.2)$$

$$\vec{\nabla} \cdot \vec{B} = 0 \quad (1.3)$$

$$\vec{\nabla} \times \vec{B} = \mu_0 \epsilon_0 \frac{\partial \vec{E}}{\partial t} + \mu_0 \vec{J}_e \quad (1.4)$$

Equation 1.1 states that an electric field,  $\vec{E}$ , produced by a source with a charge density of  $\rho_e$  diverges away from a positive charge. A magnetic field does not diverge, according to Equation 1.3, which means that it has no beginning or end points. Equation 1.4 states that the magnetic field that curls around a current is determined by the electric current density,  $\vec{j}_e$ .

The magnetic field's zero divergence, described in Equation 1.3, implies that there is no magnetic counterpart to the electric charges. The only components of electric and magnetic fields are electric charges and current densities. There have not been any magnetic currents or charges observed. Maxwell's equations take into account this observation - or lack thereof. In the event that there was a magnetic equivalent of electric charge, the charge would possess magnetic current and charge density. These magnetic representations of electric charges are frequently referred to as magnetic monopoles or just monopoles. The symmetry of Maxwell's equations would result from their existence like so,

$$\vec{\nabla} \cdot \vec{B} = \mu_0 \rho_m \quad (1.5)$$

$$\vec{\nabla} \times \vec{E} = -\frac{\partial \vec{B}}{\partial t} - \mu_0 \vec{j}_m \quad (1.6)$$

where  $\rho_m$  is the magnetic charge. Then, the magnetic charge of the monopole,  $g$ , would be given by,

$$g = \int_V \rho_m d\vec{r}^3 \quad (1.7)$$

Under a duality transformation which mixes the electric and magnetic fields, Maxwell's equations would remain symmetric upon introducing the monopole. The duality

transformation is described as follows,

$$\begin{pmatrix} \vec{E} \\ c\vec{B} \end{pmatrix} = R \begin{pmatrix} \vec{E}' \\ c\vec{B}' \end{pmatrix} \quad (1.8)$$

$$\begin{pmatrix} c\rho_e \\ \rho_m \end{pmatrix} = R \begin{pmatrix} c\rho'_e \\ \rho'_m \end{pmatrix} \quad (1.9)$$

where  $R$  is the standard  $2 \times 2$  transformation matrix with transformation parameter  $\theta$ ,

$$R = \begin{pmatrix} \cos\theta & \sin\theta \\ -\sin\theta & \cos\theta \end{pmatrix} \quad (1.10)$$

Equation 1.8 together with Equation 1.10 makes it abundantly evident that, for  $\theta = \frac{\pi}{2}$ , transformations between the electric and magnetic fields result in  $\vec{E} \rightarrow \vec{B}$  and  $\vec{B} \rightarrow -\vec{E}$ . Equation 1.9 together with Equation 1.10 demonstrates unequivocally that for  $\theta = \frac{\pi}{2}$ , transformations between the sources of the electric and magnetic fields result in  $c\rho_e \rightarrow \rho_m$  and  $\rho_m \rightarrow -c\rho_e$ . The magnetic and electric fields that occur in nature can only be transformed into one another by the addition of a monopole under the symmetries of Maxwell's equations.

## 1.2 Dirac Monopoles

The magnetic monopole is a proposed elementary particle with perhaps the most colorful history of all the particles. The monopole is postulated to be an isolated magnet with only one pole and would therefore carry a magnetic charge. Magnetism as we know it do not stem from monopoles. It was well understood in the 19th century that magnetism arose from a combination of electric currents, the electron magnetic moment and magnetic moments of other particles. Perhaps the most famous expression for the non-existence of monopoles comes from Gauss' Law -  $\vec{\nabla} \cdot \vec{B} = 0$ . In 1894, however, Pierre Curie [5] pointed out that magnetic monopoles could exist and P.A.M Dirac in 1931 [1] expanded upon the idea leading us to one of the most elegant results ever to have been conceived in all of physics - the theoretical quantization of electric charge. This section aims to explain the classical formulation of the monopole (i.e. what it would mean for Maxwell's Equations and our current understanding of electromagnetism) and after that, delve into the quantum realm to have an understanding of what Dirac thought a monopole should be.

### 1.2.1 Classical Solution

In this section, we take a look at the classical solution of a monopole. Consider the presence of magnetically charged sources. Then, in a direct analog of an electric charge at the origin, a monopole at the origin with charge  $g$  would have a magnetic field  $\vec{B}$  described by [6],

$$\vec{B} = \frac{g}{r^2} \hat{r} \quad (1.11)$$

and therefore,

$$\vec{\nabla} \cdot \vec{B} = 4\pi\rho_m = 4\pi g\delta^3(\vec{r}) \quad (1.12)$$

and we can write  $g$  as

$$g = \int_V \rho_m d\vec{r}^3 \quad (1.13)$$

At  $\mathbb{R} - \{0, 0\}$ , we have that  $\vec{\nabla} \cdot \vec{B} = 0$ . We are then led to make the somewhat naive assumption that  $\vec{A}$  exists everywhere except the origin. However, this naive assumption cannot be true. I will set out my arguments as to why in the following paragraphs.

In a direct analog with Gauss' Law (where we integrate over a 2-sphere with radius  $R$ ),

$$\oint_{S^2_R} \vec{E} \cdot d\vec{S} = 4\pi e \quad (1.14)$$

we can write

$$\oint_{S^2_R} \vec{B} \cdot d\vec{S} = 4\pi g \quad (1.15)$$

Notice that the limits of the integration done in Equation 1.15 do not intersect the origin (since it is being done over the 2-sphere). Suppose some  $\vec{A}$  exists. Then, the claim is that the integral in Equation 1.15 should be zero. (i.e.  $\oint_{S^2_R} \vec{B} \cdot d\vec{S} = 0$ )

Consider a sphere with a hole of radius  $a$  cut from the north pole. What we are considering here in essence is  $S^2_R - D$  where  $D$  is the disk of radius  $a$ . This is an open surface and we can perform the integral,

$$\int_{S^2_R - D} \vec{B} \cdot d\vec{S} = \int_{S^2_R - D} (\vec{\nabla} \times \vec{A}) \cdot d\vec{S} = \oint_D \vec{A} \cdot d\vec{l} \rightarrow 0 \quad (1.16)$$

as  $a \rightarrow 0$  which is a clear contradiction to Equation 1.15. We have just proved that  $\vec{A}$  cannot exist everywhere and it has to be singular at at least one point on the sphere.

We consider two possible solutions of  $\vec{A}$ ,  $\vec{A}^S$  and  $\vec{A}^N$  [7].

$$\vec{A}^S = \frac{gy}{r(r+z)} \hat{x} + \frac{gx}{r(r+z)} \hat{y} \quad (1.17)$$

$$\vec{A}^N = \frac{gy}{r(r-z)} \hat{x} - \frac{gx}{r(r-z)} \hat{y} \quad (1.18)$$

We then see that [7],

$$\vec{\nabla} \times \vec{A}^S = \frac{g}{r^2} \hat{r} + 4\pi g \delta(x) \delta(y) \theta(-z) \hat{z} \quad (1.19)$$

and

$$\vec{\nabla} \times \vec{A}^N = \frac{g}{r^2} \hat{r} + 4\pi g \delta(x) \delta(y) \theta(z) \hat{z} \quad (1.20)$$

Immediately, we notice that  $\vec{A}^S$  is well defined everywhere except at  $r = 0$  or  $r + z = 0$ . We also notice that  $r = 0$  is the origin and given our previous approach, we can easily delete that point from consideration. Hence, only  $r + z = 0$  has physical significance which implies  $z = -r$  and this occurs at the negative z-axis. Let us agree to neglect the negative z-axis from consideration. Then, we can compute,

$$\vec{\nabla} \times \vec{A}^S|_{r+z \neq 0} = \vec{B} \quad (1.21)$$

and analogously,

$$\vec{\nabla} \times \vec{A}^N|_{r-z \neq 0} = \vec{B} \quad (1.22)$$

To make Gauss' Law work, we need a flux tube of zero thickness along the negative z-axis as observed by Dirac [1]. The flux tube of zero thickness is aptly named the Dirac string.

Consider deleting the whole z-axis. It is then clear that  $\vec{A}^S$  and  $\vec{A}^N$  give rise to the same  $\vec{B}$  field. This then implies that  $\vec{A}^S$  and  $\vec{A}^N$  are both gauge equivalent. Mathematically we can write,

$$\vec{A}^N - \vec{A}^S = \vec{\nabla} \lambda \quad (1.23)$$

where  $\lambda$  is some scalar.

We conclude this section by observing that if we agree to work with two vector poten-

tials, it is possible to have a vector potential formulation of the magnetic field given a monopole of charge  $g$  at the origin. Geometrically, it is equivalent to covering a two-sphere with two patches - each patch having either the positive or negative  $z$ -axis defined.

### 1.2.2 Quantum Mechanical Solution

In this section, we take a look at what a monopole would mean for the theory of quantum mechanics. In 1931, Dirac published his paper on charge quantization and monopoles [1]. This paper was published right after his paper published in 1930 [8] on negative energies and a possible interpretation of the negative energies as "holes", following Oppenheimer (henceforth known as Oppenheimer's interpretation [9]). Dirac then noted that we only had an experimental value for the smallest electric charge  $e$  given by,

$$\frac{g}{e^2} = 137 \tag{1.24}$$

Dirac noticed that we did not have a theoretical value for  $e$  and that we were merely plugging in the experimental value of  $e$  into the formulas without a theoretical reasoning as to why. The paper he wrote in 1931 on monopoles gives a possible explanation as to why. In essence, Dirac shows that if a single monopole were to exist, all electric charge would be quantized. Furthermore, Dirac points out that the large experimental value of 137 introduces large quantitative differences between electricity and magnetism such that one is able to appreciate why their qualitative similarities have not been discovered experimentally. The rest of this section is an explanation of his views on the symmetries between electricity and magnetism.

Consider an electron in a time independent magnetic field. The Hamiltonian,  $H$ ,

of this system is well known and is given by,

$$H = \frac{(\vec{p} - e\vec{A})^2}{2m} \quad (1.25)$$

and we also know that

$$\hat{H}\psi = E\psi \quad (1.26)$$

where  $\psi$  is the wavefunction that represents the motion of the electron and  $E$  is the energy eigenvalues for the electron.

Let us examine what the wavefunction  $\psi$  is. We first note that it does not matter if the wavefunction is relativistic or not and that clearly,  $\psi$  is a function of  $x, y, z, t$ . We can then write  $\psi$  in the following manner,

$$\psi = Ae^{i\gamma} \quad (1.27)$$

where  $A$  and  $\gamma$  are real-valued functions of  $x, y, z, t$  such that  $|A| = 1$  if we impose the condition that  $\psi$  is normalized. Clearly,  $\gamma$  represents the phase. The phase itself is not a quantum mechanical observable (i.e. it has no physical meaning). Only the difference in phase is a quantum mechanical observable and has physical meaning. Given any two points, we can assume that the change in phase,  $\Delta\phi$  is not definite unless the two points are neighboring. For two non-neighbouring points,  $\Delta\phi$  is definite relative to some curve joining them. In general, different curves joining two non-neighbouring curves give rise to a different  $\Delta\phi$ .

We can further illustrate this point by considering two non-neighbouring points and two different curves joining the points. Let the two points be  $A$  and  $B$  and the two curves joining them be called  $\gamma_1$  and  $\gamma_2$ . Then we can write,

$$\Delta\phi = \phi(\gamma_1) - \phi(\gamma_2) = \frac{e}{\hbar} \int_{\gamma_1} \vec{A} \cdot d\vec{l} - \frac{e}{\hbar} \int_{\gamma_2} \vec{A} \cdot d\vec{l} \quad (1.28)$$

Through a well known property of integrals, we can reformulate this as,

$$\Delta\phi = \phi(\gamma_1) - \phi(\gamma_2) = \frac{e}{\hbar} \int_{\gamma_1} \vec{A} \cdot d\vec{l} + \frac{e}{\hbar} \int_{-\gamma_2} \vec{A} \cdot d\vec{l} \quad (1.29)$$

Now, we can see that the curves  $\gamma_1$  and  $-\gamma_2$  connecting  $A$  and  $B$  form a closed loop and we can then write,

$$\Delta\phi = \frac{e}{\hbar} \oint_{\gamma_1 - \gamma_2} \vec{A} \cdot d\vec{l} \quad (1.30)$$

By Stokes Theorem, the integral of  $\vec{A} \cdot d\vec{l}$  in a closed loop is merely the flux through the surface which we can denote as  $\Phi_m$ . Thus we write,

$$\Delta\phi = \frac{e}{\hbar} \Phi_m \quad (1.31)$$

and this is the well-known Aharanov-Bohm effect [10].

Now we consider the wave function itself and what different wavefunctions mean in this scenario of a free electron. Consider two arbitrary and different wavefunctions  $\psi_n$  and  $\psi_m$ . The probability of agreement,  $P$ , between the two states is given by,

$$P = \int |\psi_m^* \psi_n dx dy dz dt|^2 \quad (1.32)$$

For the integral to be definite, the integrand must have a definite phase difference between any two points regardless of whether they are neighbouring or not. Therefore, it must be the case that the change in phase of  $\psi_m^* \psi_n$  around a closed loop must be zero. This then implies that the change in phase around a closed loop of  $\psi_m^*$  must be equal and opposite to the change in phase of  $\psi_n$ . This then allows us to generalize and state that *the change in phase of a wavefunction around any closed loop must be the same for all wavefunctions*. This result implies that the change in phase must be independent of the state of the system and hence must be something determined by the dynamics of the system itself. Since the system consists of a free electron in a time independent EM field, the phase must be connected with the EM field in which

the electron moves. For a mathematical treatment, let us write  $\psi$  more generally like so,

$$\psi(\vec{x}) = \psi_1(\vec{x}) \exp\left(\frac{ie}{\hbar} \int_{\vec{x}_0}^{\vec{x}} \vec{A} \cdot d\vec{l}\right) \quad (1.33)$$

where  $\psi_1(\vec{x})$  is any ordinary wavefunction with a definite phase at each point and  $|\psi_1(\vec{x})| = |\psi(\vec{x})|$ . Consider how the momentum operator  $\vec{p}$  acts on the wavefunction  $\psi$ ,

$$\vec{p}\psi(\vec{x}) = (-i\hbar\vec{\nabla})\psi(\vec{x}) = (-i\hbar\vec{\nabla}) \left[ \psi_1(\vec{x}) \exp\left(\frac{ie}{\hbar} \int_{\vec{x}_0}^{\vec{x}} \vec{A} \cdot d\vec{l}\right) \right] \quad (1.34)$$

Upon expansion we get,

$$\vec{p}\psi(\vec{x}) = (-i\hbar) \left[ \frac{ie}{\hbar} \vec{A} \times \exp\left(\frac{ie}{\hbar} \int_{\vec{x}_0}^{\vec{x}} \vec{A} \cdot d\vec{l}\right) \psi_1(\vec{x}) + \exp\left(\frac{ie}{\hbar} \int_{\vec{x}_0}^{\vec{x}} \vec{A} \cdot d\vec{l}\right) \vec{\nabla}\psi_1(\vec{x}) \right] \quad (1.35)$$

Collecting like terms,

$$\vec{p}\psi(\vec{x}) = (-i\hbar) \left[ \frac{ie}{\hbar} \vec{A}\psi_1(\vec{x}) + \vec{\nabla}\psi_1(\vec{x}) \right] \exp\left(\frac{ie}{\hbar} \int_{\vec{x}_0}^{\vec{x}} \vec{A} \cdot d\vec{l}\right) \quad (1.36)$$

Simplifying,

$$\vec{p}\psi(\vec{x}) = e\vec{A}\psi(\vec{x}) + (-i\hbar) \exp\left(\frac{ie}{\hbar} \int_{\vec{x}_0}^{\vec{x}} \vec{A} \cdot d\vec{l}\right) \vec{\nabla}\psi_1(\vec{x}) \quad (1.37)$$

Renaming  $\exp\left(\frac{ie}{\hbar} \int_{\vec{x}_0}^{\vec{x}} \vec{A} \cdot d\vec{l}\right)$  as  $e^{i\beta}$  and collecting like terms we get,

$$(\vec{p} - e\vec{A})\psi(\vec{x}) = e^{i\beta} \vec{p}\psi_1(\vec{x}) \quad (1.38)$$

What we conclude after that computation is that the presence of the vector potential  $\vec{A}$  merely changes the phase of the wavefunction. We can also go ahead and define a new Hamiltonian  $H' = \frac{p^2}{2m}$  and write that,

$$\hat{H}'\psi_1(\vec{x}) = E\psi_1(\vec{x}) \quad (1.39)$$

When we discussed the Aharonov-Bohm effect earlier, we mentioned that the phase is path dependent. We also mentioned that the change in phase of a wavefunction around any closed loop must be the same for all wavefunctions. However, this is only partially true. Consider two wavefunctions  $\psi_1$  and  $\psi_2$ . Suppose we have that the change in phase around a certain closed loop  $L$  is  $\Delta\phi$  for  $\psi_1$  and that the change in phase around  $L$  is  $\Delta\phi + 2\pi$  for  $\psi_2$ . Then, clearly we would not be able to tell the difference between the change in phase going around  $L$  for  $\psi_1$  and  $\psi_2$  as it would be not observable due to them having a difference of  $2\pi$ . This leads us to relax the earlier condition and restate that *the change in phase around a closed loop may be different for different wavefunctions by multiples of  $2\pi$ .*

Now that the condition is relaxed, let us go back and see how our formulation of a free electron in an EM field changes. Consider the change in phase going around the Dirac string. We have mentioned earlier that the Dirac string is an infinitely long and infinitely thin solenoid. One can visualize a one dimensional curve in space stretching between two Dirac monopoles of opposite charge. Dirac required that the position of the Dirac string itself should not be observable. Now, consider the wavefunction of the electron circulating around the Dirac string. The Dirac string would not be observable if the wavefunction of the electron only acquires a trivial phase. We mentioned earlier that the phase itself is not observable and only the difference in phase is an observable. This would then imply that the change in phase,  $\Delta\phi$ , has to be integer multiples of  $2\pi$ . In other words,  $\Delta\phi = 2\pi n$ , where  $n \in \mathbb{N}$

Following Equation 1.15, we can write that the flux of a field with a monopole is,

$$\Phi_g = 4\pi g \tag{1.40}$$

Using the Aharonov-Bohm effect we derived earlier and noting that the Dirac string acts as the solenoid in the Aharonov-Bohm effect, we can write that the change in

phase  $\Delta\phi$  is,

$$\Delta\phi = \frac{e}{\hbar}\Phi_g = \frac{e}{\hbar}4\pi g \quad (1.41)$$

As we noted earlier, this change in phase has to be equal to an integer multiple of  $2\pi$ .

And so, we can write,

$$\Delta\phi = 2\pi n \rightarrow \frac{e}{\hbar}4\pi g = 2\pi n \quad (1.42)$$

This then gives us the result that,

$$eg = \frac{n\hbar}{2} \quad (1.43)$$

which is known as Dirac's quantization condition which means that if a monopole of charge  $g$  were to exist, then all electric charge must be quantized according to  $e = \frac{n\hbar}{2g}$ . However, we have to keep in mind that this formulation is not a solution to Maxwell's equations due to the singularities.

We conclude this section by giving a possible explanation as to why monopoles have not yet been observed. By Dirac's quantization condition, we have that  $g = 68.5e$  which then implies that the Coulomb force between two monopoles of opposite charge would be on the order of  $68.5^2 = 4692.25$ . Given such a large force, one can understand why we have not been able to separate dipoles into monopoles of opposite charge.

## 1.3 The Schwinger Monopole

Julian Schwinger also studied the monopole. In particular, he studied the relativistic invariance of Dirac's theory [11]. The vector potential found by Schwinger as a consequence of his research is given by,

$$\vec{A}(\vec{r}) = \frac{\mu_0 g}{4\pi r} \cot\theta \hat{\phi} \quad (1.44)$$

Following through the steps prescribed when deriving Dirac's quantisation, we end up with a different quantisation condition given by,

$$gq = \frac{2nh}{\mu_0} \quad (1.45)$$

It is obvious that the minimum magnetic monopole charge derived from this quantisation condition would be twice the Dirac charge which then directly impacts the magnitude of the monopole coupling. Schwinger went one step further to describe particles that carry both electric charge and magnetic charge known as dyons [12]. He derived a quantisation condition for dyons, with  $q_1, g_1$  being the electric and magnetic charge of the first dyon respectively,  $q_2, g_2$  being the electric and magnetic charge of the second dyon respectively, and is described like so,

$$q_1 g_2 - q_2 g_1 = \frac{2nh}{\mu_0} \quad (1.46)$$

## 1.4 Monopole-Photon Coupling

The fine structure constant,  $\alpha$ , describes the electron-photon coupling. This is the premise we will use to define the monopole-photon coupling,  $\alpha_m$  as an analog of the electron photon coupling. We substitute  $g = \frac{ng_D}{c}$  for  $e$  which gives us,

$$\alpha_m = \frac{\mu_0 g_D^2 n^2}{4\pi \hbar c} \quad (1.47)$$

Combining Equation 1.44 with  $g = \frac{nce}{2\alpha}$  where  $\alpha$  is the fine structure constant with  $\alpha = \frac{\mu_0 e^2 c}{2\hbar}$ , we conclude that the strength of the monopole-photon coupling is much greater than the magnitude of the electron-photon coupling which will result in strong implications in the production of monopoles and the way monopoles interact with matter.

## 1.5 Monopoles in Electroweak Models

The Standard Model (SM) precludes the existence of monopoles [13, 14]. However, it is proposed that monopole-like solutions are feasible in the electroweak sector of the SM, often referred to as electroweak monopoles [15]. These solutions have a minimum magnetic charge of  $2g_D$  because they adhere to Schwinger's charge quantisation. The hypothesis continues by predicting monopole masses between  $\sim 4\text{TeV}$  and  $\sim 10\text{TeV}$  [16, 17]. This mass range is well within the reach of the Large Hadron Collider(LHC).

### 1.5.1 Topologically Stable Finite Energy Electroweak Monopoles

The possible existence of non-sterile right-handed (RH) neutrinos, which we will denote as  $\nu_R$ , with electroweak-scale (EW-scale) masses in a seesaw mechanism for light neutrinos has been postulated [18]. One of the consequences of such a possibility is the existence of topologically stable finite energy EW-scale monopoles [19]. RH neutrinos acquire EW-scale majorana masses ( $M_R \sim 246 \text{ GeV}$ ) by coupling to a complex Higgs triplet which we will denote as  $\chi$ . The assumption that the RH neutrinos are non-sterile implies an upper bound on the mass of the RH neutrinos where  $M_R > 46 \text{ GeV}$  due to the measured width of the Z boson [19]. This then implies that  $\langle \chi \rangle = \nu_M \propto \Lambda_{EW}$  which destroys the experimentally verified relationship between the masses of the W and Z boson,  $M_W = M_Z \cos \theta_W$  where  $\theta_W$  is the weak mixing angle. This relationship,  $M_W = M_Z \cos \theta_W$ , is preserved by introducing a real Higgs triplet which we will denote as  $\xi$  with  $\langle \xi \rangle = \langle \chi \rangle = \nu_M$ . Let us call this model the EW- $\nu_R$  model. The EW- $\nu_R$  model has the following Higgs content along with their vacuum manifolds:

- One real Higgs triplet,  $\xi$  ; Vacuum Manifold -  $S^2$
- One complex Higgs triplet  $\chi$  ; Vacuum Manifold -  $S^5$
- Two complex Higgs doublets  $\phi_i^{SM}$ ,  $i = 1, 2$  which couple to the SM ; Vacuum Manifold -  $S^3$

- Two complex Higgs doublets  $\phi_i^M$ ,  $i = 1, 2$  which couples to the mirror fermions ; Vacuum Manifold -  $S^3$
- Higgs singlets which are not relevant to the discussion here but are important for other reasons

To find a finite-energy field configuration at spatial infinity which corresponds to a monopole, the Higgs field should approach its minima. The minima of the Higgs field is described by the so-called vacuum manifold which forms a sphere in 3-dimensional internal space commonly denoted as  $S^2$ . A 3-dimensional spatial sphere is mapped to the sphere of the vacuum manifold  $S^2$ . This particular mapping corresponds to the second homotopy group  $\pi_2$  (for 3-dimensional space). There are three well known results in topology that are useful here.

$$\pi_n(S_n) = Z \tag{1.48}$$

$$\pi_i(S_n) = 0 \quad \forall i < n \tag{1.49}$$

$$\pi_n(S_1 S_2 \dots S_k) = \pi_n(S_1) \pi_n(S_2) \dots \pi_n(S_k) \tag{1.50}$$

Therefore, we have that  $\pi_2(S_2) = Z$  where  $Z = 0, 1, 2, ..$  and  $Z$  refers to the winding number.  $Z = 0$  corresponds to the trivial vacuum with no monopole,  $Z = 1$  corresponds to the first non-trivial solution and so on. The monopole solution is topologically stable because it takes an infinite amount of energy to go from one configuration to another (i.e. to go from the  $n = 1$  configuration to the  $n = 0$  configuration takes an infinite amount of energy).

Let us consider the Georgi-Glashow model [20] as an example. In the model proposed by Georgi and Glashow, the group structure is  $SO(3) \sim SU(2)$  ( $SU(2)$  is the

covering group of  $SO(3)$ ) with a real Higgs triplet  $\xi = (\xi_0, \xi_1, \xi_2)$ . The vacuum manifold is therefore  $\nu_M^2 = \xi_0^2 + \xi_1^2 + \xi_2^2$  which corresponds to  $S^2$ . Since  $\pi_2(S^2) = \mathbb{Z} \neq 0$ , this model is able to accommodate a topologically stable monopole.

Let us consider the SM as another example. The SM only contains a complex Higgs doublet. The vacuum manifold of the SM is therefore  $S^3$ . Since  $\pi_2(S^3) = 0$ , the well-known result of the SM not being able to accommodate any monopoles is reproduced.

The vacuum manifold of the Higgs sector is given by

$$S_{vac} = S^2 \times S^5 \times \sum_{i=1,2} S_{SM,i}^3 \times \sum_{i=1,2} S_{M,i}^3 \quad (1.51)$$

Then, the second homotopy group of the vacuum manifold of the EW- $\nu_R$  model is given by

$$\pi_2(S_{vac}) = \pi_2(S^2) \bigoplus \pi_2(S^5) \bigoplus_{i=1,2} \pi_2(S_{SM,i}^3) \bigoplus_{i=1,2} \pi_2(S_{M,i}^3) = \pi_2(S^2) \cong \mathbb{Z} \quad (1.52)$$

Notice that the EW- $\nu_R$  model is able to accommodate a topologically stable monopole because of the real Higgs triplet,  $\xi$ .

### 1.5.2 The Dirac Quantisation Condition and the Weak Mixing Angle

Equation 1.43 is known as the Dirac Quantisation Condition (DQC). In the presence of a monopole, magnetic charges are quantised in quanta of  $\frac{\hbar}{2e}$  according to the DQC.

$S^2$  is associated with the vacuum manifold of the real Higgs triplet  $\xi$ . Topological quantization would involve the  $SU(2)$  coupling  $g_s$  rather than the standard electro-

magnetic coupling  $e$  [21]. For the magnetic charge  $g$ , the quantization condition reads

$$gg_s = \frac{n}{2}, n \in \mathbb{Z} \quad (1.53)$$

The full SM gauge group structure,  $SU(2) \times U(1)$  is broken down to the usual electromagnetic  $U_{em}(1)$  group by the complex Higgs doublets and the complex Higgs triplet  $\xi$  of the EW- $\nu_R$  model. The  $W_\mu^3$  gauge field of the  $SU(2)$  subgroup is a mixture of the Z-boson and photon fields parameterized by the weak mixing angle  $\theta_W$ .

$$W_\mu^3 = \cos\theta_W Z_\mu + \sin\theta_W A_\mu \quad (1.54)$$

where  $\sin\theta_W = \frac{g_U}{g_U^2 + g_S^2}$  ( $g_U$  is the  $U_\gamma(1)$  coupling and  $g_S$  is the  $SU(2)$  coupling).

The corresponding field strengths are [21]

$$W_{ij}^3 = \cos\theta_W Z_{ij} + \sin\theta_W F_{ij} \quad (1.55)$$

where  $F_{ij}$  is the usual EM field-strength tensor and  $Z_{ij}$  is the Z field-strength tensor. This mixing between the photon and Z-boson is why this particular monopole solution is called the  $\gamma - Z$  monopole. The corresponding B-field intensity defined by  $\frac{1}{2}\epsilon_{ijk}W_{jk}^3$  is given by [21]

$$B_i^{\gamma Z} = \frac{1}{gr^2} (\cos\theta_W e^{-M_Z r} + \sin\theta_W) \hat{r}_i \quad (1.56)$$

Using  $e = g \sin\theta_W$ , we obtain

$$B_i^{\gamma Z} = \frac{\sin\theta_W}{er^2} (\cos\theta_W e^{-M_Z r} + \sin\theta_W) \hat{r}_i \quad (1.57)$$

At large distances ( $r \gg R_c \sim \frac{1}{g\nu_M}$  where  $R_c$  is the core radius of the monopole), the  $\gamma - Z$  magnetic field is given by [21]

$$B_i^{\gamma Z} \sim \frac{\sin^2\theta_W}{er^2} \hat{r}_i \quad (1.58)$$

At these large distances, the true magnetic field  $B_i$ , defined in terms of  $F_{ij}$  is given by [21]

$$B_i \sim \frac{\sin \theta_W}{er^2} \hat{r}_i, \quad i = 1, 2, 3, \quad r \gg R_c \quad (1.59)$$

Comparing this magnetic field with the conventional definition of the monopole, we get

$$g_M = \frac{\sin \theta_W}{e} \quad (1.60)$$

Notice that the DQC is violated by the weak mixing angle factor in  $g_M = \frac{\sin \theta_W}{e}$ . This implies that the electron wavefunction would not be single-valued along a loop that surrounds the monopole at large distances,  $r \gg R_c$ .

The topological quantisation rule  $gg_s = \frac{n}{2}$  stemming from the homotopy properties of the  $SU(2)$  group is insufficient for the quantum consistency of the electron wavefunction in the presence of the magnetic field induced by the  $\gamma - Z$  monopole. One then imposes the DQC as an additional constraint [21].

$$eg_M = \frac{n}{2}, \quad n \in \mathbb{Z} \quad (1.61)$$

Using  $eg_M = \frac{n}{2}$  and  $g_M = \frac{\sin \theta_W}{e}$ , one obtains

$$\sin \theta_W = \frac{n}{2} \quad (1.62)$$

Squaring both sides,

$$\sin^2 \theta_W = \frac{n^2}{4}, \quad n \in \mathbb{Z} \quad (1.63)$$

Since  $\sin \theta_W \leq 1$ , we have that  $n = 1$  or  $n = 2$ . The  $n = 2$  case leads to a massless W boson [21]. This is not in good agreement with experimental and theoretical evidence pointing to a massive W boson. We thus ignore the  $n = 2$  case and focus on the  $n = 1$  case. When  $n = 1$ ,  $\sin^2 \theta_W = \frac{1}{4}$  which is close to the experimental value of  $\sin^2 \theta_W \approx 0.231$ . Indeed with renormalization one is able to get really close to the agreed upon value for  $\sin^2 \theta_W$  [21].

## 1.6 The Cho-Maison Monopole

Dirac suggested a modification of Maxwell's electromagnetism that allows the existence of a spherically symmetric monopole solution in 1931 [1]. With this modification comes a singularity known as the Dirac string, which spoils the regularity and well-definedness of the theory. The theory only makes sense when one considers a subspace where the singularity is not present. The appropriate gauge transformation needs to be well defined on the subspace  $S^1 \subset S^2$ . Therefore the Dirac monopole is nothing but the non-trivial fiber bundle characterized by the fundamental group  $\pi_1(U(1)) \cong \pi_1(S^1) \cong \mathbb{Z}$ . As shown in Equation 1.43, the charge is quantized as  $q_m = \frac{n}{2e}$  where  $n \in \mathbb{Z}$  and is commonly known as the Dirac Charge Quantisation or DQC. The mathematical self-consistency however does not change the fact that the Dirac singularity is ever present and spoils the theory.

Consider a semi-simple and simply connected group  $G$ . Then, there exists a group isomorphism  $\pi_2(G/H) \cong \pi_1(H)$ . Let  $G = SU(2)$  and  $H = U(1)$ . The coset manifold  $SU(2)/U(1)$  is the vacuum manifold of the bosonic part of the Georgi-Glashow model. Qualitatively, the  $\pi_2(SU(2)/U(1)) \cong \pi_1(U(1))$  isomorphism implies that the non-trivial second homotopy group which can be mapped isomorphically to the Dirac monopole's topological class is an equivalence class of homotopy from the sphere to the vacuum manifold of some spontaneous symmetry breaking theory (Georgi-Glashow). This mapping embeds the point on  $S^2$  of infinite radius into the ground state. Therefore the existence of a stable solitonic solution of finite energy is all but guaranteed. This is the well known 't Hooft-Polyakov monopole which does not have the sin of a Dirac singularity.

The 't Hooft-Polyakov monopole is a monopole arising out of a spontaneous symmetry breaking theory. The question then becomes if monopoles can arise out of other spontaneous symmetry breaking theories and in particular, the theory put forward by

Glashow, Weinberg and Salam (more commonly known as the electroweak theory). In the electroweak theory, the symmetry breaking pattern is  $SU(2)_L \times U(1)_Y$  being broken to the well known unbroken  $U(1)_{em}$  group representing Maxwellian interactions. In the same spirit of what was done earlier, we have that  $\pi_2(SU(2) \times U(1)/U(1)) \cong \pi_2(S^3)$ . Notice that by Equation 1.49,  $\pi_2(S^3)$  is completely trivial and hopes of a so-called electroweak monopole were dashed until Cho and Maison put forward a paper in 1996 [15].

The Lagrangian of the electroweak theory is [15]

$$\mathcal{L} = -\frac{1}{4} (W_{\mu\nu}^a)^2 - \frac{1}{4} (B_{\mu\nu})^2 + (\mathcal{D}_\mu \phi)^\dagger (\mathcal{D}^\mu \phi) - V(\phi) \quad (1.64)$$

where  $W_{\mu\nu}^a$  and  $B_{\mu\nu}$  are the gauge field strength tensors of  $SU(2)_L$  and  $U(1)_Y$  respectively.

The covariant derivative when expanded reads [15]

$$\mathcal{D}_\mu \phi = (\partial_\mu - ig\tau^a W_\mu^a - ig'Y B_\mu) \phi \quad (1.65)$$

where  $\tau^a$  is the weak isospin generator of  $SU(2)_L$ ,  $g$  is the coupling constant associated with  $SU(2)_L$ ,  $Y$  is the hypercharge generator of  $U(1)_Y$  and  $g'$  is the coupling constant associated with  $U(1)_Y$ . The covariant derivative encodes the interactions between the Higgs doublets and gauge fields in the kinetic term of the Higgs sector. In the potential term of the Higgs sector,  $V(\phi)$  is the conventional form of Higgs self interactions leading to the non-zero vacuum expectation value (VEV) when symmetry is spontaneously broken. One has the freedom to choose a spherically symmetric form of the Higgs doublet [15],

$$\phi = \sqrt{\frac{1}{2}} \rho(r) \xi(\theta, \varphi) \quad (1.66)$$

where  $\rho(r)$  is the reduced Higgs boson defined by absorbing the VEV into the canonical definition of the Higgs (i.e.  $\rho(r) = v + h(r)$ ) and  $\xi$  is a normalized ( $\xi\xi^\dagger = 1$ ) doublet field defined as

$$\xi(\theta, \varphi) = i \begin{pmatrix} \sin\left(\frac{\theta}{2}\right) e^{-i\varphi} \\ -\cos\left(\frac{\theta}{2}\right) \end{pmatrix} \quad (1.67)$$

When the Higgs multiplet gains the VEV around the true vacua,

$$\xi \rightarrow \begin{pmatrix} 0 \\ 1 \end{pmatrix} \quad (1.68)$$

By restricting to a unitary gauge, one is able to remove all of the Nambu-Goldstone modes without worrying about unitarity violation.

The spherically symmetric ansatz of the relevant gauge fields in the unitary gauge can be chosen as follows

$$W_{\pm}^{\mu} = \sqrt{\frac{1}{2}} (W_1^{\mu} + iW_2^{\mu}) = \frac{i}{g} \frac{f(r)}{\sqrt{2}} e^{i\varphi} (0, 0, 1, i \sin \theta) \quad (1.69)$$

$$W_3^{\mu} = \frac{1}{g} (A(r), 0, 0, 1 - \cos \theta) \quad (1.70)$$

$$B^{\mu} = \frac{1}{g'} (B(r), 0, 0, 1 - \cos \theta) \quad (1.71)$$

$A(r)$  and  $B(r)$  are simply functions of the radial coordinate  $r$ . Objects in the bracket are in spherical coordinates  $(t, r, \theta, \varphi)$ . When the gauge fields are in this form, they look very similar to a Dirac monopole with the singularity at the South Pole because of the  $1 - \cos \theta$  term.

By substituting the ansatz into the Lagrangian given in Equation 1.64, one obtains  $B_\mu$  in terms of  $\xi$ . This enables one to perform a suitable gauge transformation of the  $U(1)_Y$  hypercharge group to remove the Dirac-like singularity away. Under a suitable gauge transformation of the  $U(1)_Y$  hypercharge group, the normalized doublet  $\xi$  transforms as

$$\xi \rightarrow \xi' = e^{i\beta Y} \xi \quad (1.72)$$

By gauge invariance,  $\xi$  and  $\xi'$  belong to the same equivalence class and one can write

$$\xi' = c\xi, \quad c \in \mathbb{C} \quad (1.73)$$

After spontaneous symmetry breaking, the physical gauge fields can be extracted. The cross-term arising from the two gauge fields  $W_\mu^3$  and  $B_\mu$  is removed by rotating the gauge fields by the Weinberg angle  $\theta_W$  where  $\theta_W$  is defined as

$$\tan(\theta_W) = \frac{g'}{g} \quad (1.74)$$

One ends up with the rotated physical gauge fields,

$$A^\mu = B^\mu \cos \theta_W + W_3^\mu \sin \theta_W = \left( \frac{e}{g^2} A(r) + \frac{e}{g^2} B(r), 0, 0, \frac{2}{e}(1 - \cos \theta) \right) \quad (1.75)$$

$$Z^\mu = -B^\mu \sin \theta_W + W_3^\mu \cos \theta_W = \frac{e}{gg'} (A(r) - B(r), 0, 0, 0) \quad (1.76)$$

where  $e$  denotes the canonical electromagnetic coupling and

$$e = g \sin \theta_W = g' \cos \theta_W \quad (1.77)$$

By Gauss' Law, one has

$$q_e = \int dS E_r = \int d\Omega r^2 F_{0r} = -er^2 \left[ \frac{1}{g^2} A' + \frac{1}{g'^2} B' \right]_{r \rightarrow \infty} \quad (1.78)$$

where the prime on  $A$  and  $B$  indicates a derivative with respect to the radial component  $r$ . Choosing appropriate boundary conditions which guarantee regularity of solutions in the  $SU(2)$  sector [15],

$$\begin{aligned} f(0) = 1, \quad \rho(0) = 0, \quad A(0) = 0, \quad B(0) = b_0 \\ f(\infty) = 0, \quad \rho(\infty) = 0, \quad A(\infty) = A_0, \quad B(\infty) = B_0 \end{aligned} \quad (1.79)$$

The asymptotic behavior of the free parameters  $A$  and  $B$  under the chosen boundary conditions is given by

$$A \sim A_0 + \frac{A_1}{r} \quad (1.80)$$

$$B \sim A + \frac{B_1}{r} e^{-mzr} \quad (1.81)$$

With these asymptotic conditions, one is able to solve for  $q_e$  and obtain [15],

$$q_e = -\frac{A_1}{e} \quad (1.82)$$

By comparison with the ordinary Coulomb potential,

$$A_1 \sim \alpha_e = -e^2 \quad (1.83)$$

The magnetic charge is given by [15]

$$q_M = \frac{1}{e} \quad (1.84)$$

The magnetic charge is quantized in terms of  $\frac{n}{e}$  which is twice that of the DQC. The electric charge of the Cho-Maison monopole is also given by [15],

$$q_e = \frac{2}{e} \sin^2 \theta_W \int_0^\infty f^2 A dr \quad (1.85)$$

By quantisation of electric charge, one has

$$q_e = ne, \quad n \in \mathbb{Z} \quad (1.86)$$

Then, equating Equation 1.84 with Equation 1.85,

$$ne = \frac{2}{e} \sin^2 \theta_W \int_0^\infty f^2 A dr \quad (1.87)$$

And therefore,

$$\sin^2 \theta_W = \frac{n\alpha}{2} \frac{1}{\int_0^\infty f^2 A dr} \quad (1.88)$$

By numerically determining the value of  $\int_0^\infty f^2 A dr$  one is able to determine the value of  $\sin^2 \theta_W$  from the perspective of the Cho-Maison monopole.

## 1.7 The Nambu Monopole

The existence of string-like objects in an Abelian Higgs model as a simplified model for hadrons has been postulated [22]. Nambu extended this analogy to monopoles [23]. 't Hooft and Polyakov have shown the existence of topologically stable finite energy solutions in a  $SO(3)$  Higgs model [24, 25]. The more relevant model for electromagnetic and weak interactions is the electroweak theory. The electroweak theory admits classical solutions which are analogous to the hadronic strings model put forward by Nielsen and Olesen with a monopole-antimonopole pair attached at each end of the string. The mass of the monopole and tension of the string are estimated to be in the TeV range.

Qualitative arguments for the existence of such monopoles are sketched below. Consider a Wu-Yang monopole where the isospin direction is locked with the radial vector. A Higgs field is necessary to smooth out the singularity at the origin and make the energy of the system finite. In the 't Hooft-Polyakov model, the Higgs field is an isovector given by

$$\phi^i(r) = f(r) \frac{\chi^i}{r} \quad (1.89)$$

where  $f(r)$  is approximately a constant asymptotically and  $f(0) = 0$  so  $\phi^i$  is well-defined everywhere. In the electroweak theory, the Higgs field is an isospinor  $\phi^\alpha$ ,  $\alpha = 1, 2$  and the corresponding ansatz is given by

$$\phi \sim \begin{pmatrix} \cos \frac{\theta}{2} \\ \sin \frac{\theta}{2} e^{i\varphi} \end{pmatrix} \quad (1.90)$$

for  $r \neq 0$ . Notice that along the negative z-axis where  $\theta = \pi$ , the phase is ill-defined. Therefore,  $\phi$  necessarily has to be zero when  $\theta = \pi$  in order to maintain

well-definedness. This demand then implies that one cannot have a simple monopole but it must be accompanied by a string. Along the negative  $z$  direction far away from the origin, there is a  $U(1)$  gauge field and the effect of the monopole can be ignored. Then,  $\phi$  is essentially of the form

$$\phi \sim \begin{pmatrix} 0 \\ f(\rho)e^{i\varphi} \end{pmatrix} \quad (1.91)$$

where  $\rho = x^2 + y^2$ . The string is made up of a flux of a combination of gauge fields which is inherently unstable. A stable configuration is obtained if the string is terminated by putting a monopole of opposite charge and spin on the other end of the string. The monopole carries a charge  $q_M$  where

$$q_M = \frac{\sin^2 \theta_W}{e} \quad (1.92)$$

In the spirit of the Kalb-Ramond monopole, the DQC is imposed and one obtains

$$\sin^2 \theta_W = \frac{n}{2}, \quad n = 1, 2 \quad (1.93)$$

Then, the predicted values of  $\sin^2 \theta_W$  are that  $\sin^2 \theta_W = \frac{1}{2}$  or  $\sin^2 \theta_W = 1$ . As we did earlier, we will neglect the  $\sin^2 \theta_W = 1$  case and conclude that for the Nambu monopole, the predicted value of  $\sin^2 \theta_W$  is  $\frac{1}{2}$ .

Notice how both the Cho-Maison monopole and the Nambu monopole are solutions of the electroweak theory. One starts to wonder if they are the same. Indeed, they are not the same for three reasons. Firstly, the Cho-Maison monopole's quantisation condition differs with the Nambu monopole's quantisation condition by a factor of  $\sin^2 \theta$  as per Equation 1.84 and Equation 1.92. Secondly, unlike the Cho-Maison monopole, the Nambu monopole is not spherically symmetric since the solution proposed by Nambu involves a dumbbell-like configuration with the monopole at one end,

the antimonopole at the other end and joining them together is a  $Z$  flux tube. In order to obtain a spherically symmetric solution, one needs to separate the monopole-antimonopole pair which requires infinite energy. Thirdly and lastly, the Cho-Maison monopole is neutrally uncharged (i.e.  $Z_e = Z_m = 0$ ). The Cho-Maison is then unable to connect with its antimonopole through a  $Z$  flux tube like the Nambu monopole. Therefore, the Cho-Maison monopole is the only true electroweak monopole with a predicted mass range of a few TeV [17].

The SM by itself is unable to accommodate any monopoles. One needs an extension of the SM in order to accommodate monopoles in any of the Beyond SM (BSM) theories. In particular a real Higgs triplet is key to the existence of monopoles in a theory. In the EW- $\nu_R$  model postulated by P.Q. Hung [19] and expanded upon by Ellis, Hung and Mavratamos [21] a real Higgs triplet was included so that monopoles could exist in the theory. Ellis, Hung and Mavratamos went one step further and shown how the value of the electroweak mixing angle  $\theta_W$  can be predicted from the existence of a monopole by the imposition of the DQC. In this paper, the idea of predicting the value of the electroweak mixing angle was expanded upon. In particular, the electroweak monopole and the Nambu monopole were studied and it was shown that one is able to predict the value of the electroweak mixing angle in these monopole models as well. Other monopole models such as the Julia-Zee dyon [26] were not studied in this paper. However, given that the electroweak monopole has the same topological origin as the Julia-Zee dyon and that the Julia-Zee dyon can be extended to the electroweak monopole with a suitable ansatz one should be able to predict the value of the electroweak mixing angle in the model of Julia and Zee as well. In conclusion, there is a certain class of monopoles for which one is able to predict the value of the electroweak mixing angle. Monopoles in that class must be born out of a spontaneous symmetry breaking theory and a real Higgs triplet must exist in that theory.

## 1.8 Matter Interactions

A particle with both an electric and magnetic charge in the presence of an electromagnetic field would experience the Lorentz force. This force is given by

$$\vec{F} = q(\vec{E} + \vec{v} \times \vec{B}) + g(\vec{B} - \vec{v} \times \frac{\vec{E}}{c^2}) \quad (1.94)$$

The interactions of a monopole with an electric field will be at least a magnitude larger than those of an electrically charged particle with an electric field because the Dirac charge is approximately equivalent to  $68.5e$ . Suppose the monopole has a charge of  $g$  and is moving at a speed of  $\beta = \frac{v}{c}$ . With a strength of  $\beta g$ , it then interacts with an electron in an atomic orbital. Therefore, monopoles show up in detectors as highly ionizing particles (HIPs). Note that Highly Electrically Charged Objects (HECOs) follow this line of reasoning. The energy loss in matter, or  $\frac{dE}{dx}$ , is often the characteristic that separates HIPs from other types of particles. Pair-production, bremsstrahlung, and ionization of the media are the three mechanisms in which electrically and magnetically charged particles lose energy. A monopole would then lose energy via all 3 mechanisms - ionization of the media being the dominant [27, 28].

## 1.9 Energy Loss via Ionisation of the Medium

When moving through a medium, electrically charged particles lose energy either through collisions with atomic nuclei or interactions with electrons from atomic orbitals. Ionization describes the liberation of electrons following an interaction with the traversing particle. Non-ionizing Energy Loss (NIEL) is the term used to describe the energy loss a particle goes through upon a collision with an atomic nucleus. Since Non-ionizing Energy Loss is seldom taken into account due to practical considerations as well as the fact that energy loss via ionization outweighs NIEL by a considerable factor. Therefore, in most cases, just the energy loss by ionization is often taken into account.

The Bethe-Bloch formula describes the mean ionization energy loss for Highly Electrically Charged Objects (HECOs) like so,

$$-\frac{dE}{dx} = K \frac{Z}{A} \frac{z^2}{\beta^2} \left[ \ln \frac{2m_e c^2 \beta^2 \gamma^2}{I} - \beta^2 - \frac{\delta}{2} \right] \quad (1.95)$$

where  $z$  is the charge of the particle in units of  $e$ ,  $\beta c$  is the velocity of the particle,  $m_e c^2$  is the rest mass of an electron,  $I$  is the mean ionization energy of the material and  $\delta$  is the correction term to the density which becomes relevant for relativistic particles.

We note that the Bethe-Bloch formula (Equation 1.95) is only valid for Highly Electrically Charged Objects (HECOs) because they are electrically charged. The Bethe-Bloch formula is only valid for electrically charged particles. We should alter it in order to analyze the energy loss of monopoles, starting by substituting  $ze \rightarrow \beta g$ . Because of how strongly the electrons interact with the monopoles' magnetic field, large energy depositions are anticipated when they move through a material. High momentum transfer and low momentum transfer are the two regimes under which a monopole loses energy.

The high momentum transfer model was derived by Kazama, Yang, and Goldhaber (KYG) by solving the Dirac equation for an electron in a monopole's magnetic field [29].

By using the dipole approximation with a first order Born approximation with an accuracy of 0.03, the low momentum transfer model was derived by S.P. Ahlen for monopoles with  $\beta \geq 0.2$  and  $\gamma \leq 100$  [30]. Spin effects and contributions from the internal structure of the nuclei render the formula invalid for  $\gamma > 100$ . The Ahlen low momentum energy loss formula for monopoles is given by,

$$-\frac{dE}{dx} = K \frac{Z}{A} g^2 \left[ \ln \frac{2m_e c^2 \beta^2 \gamma^2}{I} - \frac{\delta}{2} + \frac{k(g)}{2} - \frac{1}{2} - B(g) \right]. \quad (1.96)$$

where  $g = ng_D$  is the magnetic charge,  $\beta c$  is the velocity of the monopole,  $k(g)$  is the KYG correction and  $B(g)$  is the Bloch correction.

The energy lost by ionizing monopoles is not based on the assumption of spin dependency. At relatively low velocities ( $\beta < 0.01$ ), the monopole spin becomes significant. However, because of the magnetic field's dependency on  $\beta$ , ionization ceases to occur at low velocities.

From comparing Equations 1.95 and 1.96, we can observe that the magnitude difference between magnetically charged particles with  $|g| = g_D$  and their electrically charged counterparts with  $|z| = e$  is four orders of magnitude. The majority of the kinetic energy is deposited by electrically charged particles at low velocities at the end of their trajectories. This deposition of energy is known as the Bragg peak. However, at lower velocities, particles with magnetic charges deposit less kinetic energy. This can be seen in the Ahlen formula for magnetically charged particles as  $\frac{dE}{dx} \sim \ln(\beta^2)$  whereas in the Bethe-Bloch formula for electrically charged particles,  $\frac{dE}{dx} \sim \frac{1}{\beta^2}$ .

## 1.10 Detection Techniques

Numerous studies have been conducted in the past in an effort to identify a monopole, utilizing both direct and indirect techniques of detection. The significant energy loss from ionization is the monopole's distinguishing feature. These studies use clever methods and tools to take advantage of this characteristic. The ability to look for monopoles exposed to magnetic fields was made possible by the development of particle detectors with precise tracking systems. These particle detectors would register such monopoles in magnetic fields as anomalies. A divergence in the magnetic flux would suggest the presence of a monopole as well. This technique is used for monopoles that are trapped in matter.

## 1.11 Heavily Etched Nuclear Track Detectors

Plastic foils, typically CR39 and Makrofol, are used as Nuclear Track Detectors (NTDs). Nuclear Track Detectors (NTDs) are used to recognize Highly Ionizing Particles (HIPs) created in particle colliders [31, 32] and cosmic ray experiments [33–36]. Highly Ionizing Particles (HIPs) destroy the polymers of the Nuclear Track Detectors (NTDs) when they travel through them and cause damage to the NTDs. The charge and velocity of the Highly Ionizing Particle (HIP) determine how much damage is done. The NTD is then etched, creating etch pits where the HIPs had previously gone through. An optical microscope is used to observe these etch pits. The details of the incident HIP (such as charge, energy, direction of motion and etc) is contained in the size and shape of these etch pits.

## 1.12 Monopoles Trapped in Matter

Monopoles created shortly after the Big Bang might become stuck in meteorites, rocks, or the crust of the Earth. With binding energies on the order of  $\sim 100\text{keV}$  [37], they are bound to the nuclei of the materials. Monopole production need not just occur in the very early universe. High energy collisions at particle accelerators would be able to produce monopoles as well. Before reaching detector or sub-detector systems, monopoles generated in particle accelerators often pass through layers of inactive material. It is very feasible that the monopole becomes stuck in that inactive material before reaching the detection/sub-detection systems. For the Large Hadron Collider (LHC), trapped monopoles are searched for in the beam pipe surrounding the interaction points [38].

There are several methods of extracting such monopoles trapped in matter. The monopole can be extracted from a solid sample by applying a strong magnetic field to the sample surface, provided the field is 5T or greater [39–43]. Prior to the monopoles being extracted using a magnetic field, the sample can also be heated and/or evaporated [44]. The monopole would accelerate in this magnetic field, and an array of scintillators and/or Nuclear Track Detectors (NTDs) would be able to detect it. This experiment can be divided into three broad processes: extraction, acceleration, and detection. In each phase, there are uncertainties. The charge and mass of the monopole have a significant impact on the efficiencies and the efficiency reduces to zero after a certain mass point [45].

With the development of superconducting magnetometers, the three-step strategy outlined above is no longer necessary. As a result, the induction technique may be used, which eliminates the first two phases (extraction and acceleration) and allows for quick examination of the sample. Additionally, since measurement is dependent on the magnetic charge rather than the mass of the monopole, there is less room for

error and uncertainty.

This method involves passing samples through a superconducting coil to evaluate changes in induced currents, sometimes referred to as persistent current. The charge of the monopole is directly proportional to the persistent current. When the sample is repeatedly passed through through the coils, non-zero persistent current measurements would, of course, be the signature of a monopole. This is the equivalent to observing a divergence in the magnetic field. This method is exactly what the MoEDAL (Monopole and Exotics Detector at the Large Hadron Collider) experiment search utilizes to look for trapped monopoles in the MoEDAL Magnetic Monopole Trapper samples [31].

## 1.13 Observations of Monopole-Like Events

There have been many searches for magnetic monopoles, none of which have produced any evidence for their existence. Many experiments have been re-interpreted and deemed as inconclusive. In 1975, an experiment that consisted of layers of NTD foils covered with nuclear emulsions and a layer of Cherenkov radiation, claimed to support the observation of a monopole of more than 200GeV [46]. However promising, later interpretation of the data showed the tracks to be inconsistent with that of a monopole. The identity of the particle remained inconclusive [34].

Similar experiments set up in the 1980s seemed to point to the existence of monopoles - in the first, a loop was connected to a superconducting input coil of a magnetometer. If a Dirac monopole passed through the loops, the result would be a flux change of  $8\Phi_0$ . Even though the results seemed consistent with the signal of a Dirac monopole, and was one of the most accurate observations to date, there was a high chance that it could have been caused by instrumental effects. Furthermore, there had been inconsistencies in the monopole flux calculations [35].

Another experiment carried out in 1983 was the 250-day placement of nuclear emulsion plates in a lead-mercury shield 1370 meters deep in a gold mine underground. With this shielding, any local radioactivity that would upset the plates was effectively eliminated, and the depth ensured that all cosmic ray background was eliminated. The volume was examined for any discernible/visible tracks after exposure.  $\alpha$  particles were determined to be the cause of all but seven tracks. Six of these tracks underwent examination, and it was discovered that they were protons produced by reactions of thorium decay [47]. Additionally, it was found that either ternary fission processes or monopole-induced ternary fission resulted in the seventh track.

A  $0.18m^2$  monopole detector with an effective observation duration of 8242 hours

---

that used a method based on the induction method captured a total flux of  $0.83\Phi_0$  in 1985. It is essential to remember that a Dirac monopole should produce a total magnetic flux of  $2\Phi_0$ . Naturally, it was determined that none of the explanations for this result that were emphasized in the publication [48] were deemed probable.

## 1.14 Searches for Cosmological Monopoles

It is thought that the unification of interactions that occur at the fundamental level result in monopoles [24, 25, 49]. However, we cannot be certain of an observation of a monopole based on this reason alone. Given the limitations of our current technology and the fact that these monopoles can have masses up to  $10^{16}\text{GeV}$ , the likelihood of creating them are slim, if not completely impossible.

The numerous phase transitions that were taking place when the Universe was in its infancy meant that there was a higher chance that monopoles would be produced. Since they are stable particles, monopole-antimonopole annihilation would be the only method to lower the density of monopoles. It is important to remember that during the early stages of the universe, the rapid expansion of the universe led to a significant decrease in the frequency of monopole-antimonopole collisions. This means a relatively high density of monopoles would have continued to exist. The cosmic monopole issue, which asserts that the monopole density is comparable to the baryon density, is a result of the GUT models, and it is here where the GUT and cosmological models diverge and contradict each other. This issue can be solved by examining the inflationary universe model, in which the quantity of monopoles is reduced to a small but non-negligible amount. The currently existing cosmological models are unable to predict how abundant monopoles will be, despite the fact that there are several scenarios or events in which they can be produced [49].

The magnetic field of the Milky Way galaxy, whose energy density is dissipated at a rate proportionate to the monopole density, causes monopoles to accelerate, according to the Parker Limit, which places a limit on the flux of the monopoles [50].

A flux bound for monopoles of  $10^{-16}\text{cm}^{-2}\text{s}^{-1}\text{sr}^{-1}$  is derived by requiring that the magnetic field energy not substantially depleted within a time period of the order

of  $10^8$  years. This rate of magnetic field energy dissipation has a mass dependency and will change the flux limit for monopoles with masses greater than  $10\text{GeV}$  to  $10^{-13}\text{cm}^{-2}\text{s}^{-1}\text{sr}^{-1}$ .

The velocities of heavy cosmological monopoles are affected by gravitational and magnetic fields. A cosmological monopole would reach an in-fall velocity of  $10^{-3}c$  independent of its mass due to gravitational fields alone. Consider a galactic magnetic field carrying an approximate field strength of  $3 \times 10^{-10}\text{T}$ . The influence of the field on a Dirac monopole of coherence length  $10^{19}\text{m}$  would result in the monopole having a velocity of  $v = (\frac{2g_D BL}{m}) \approx 10^{-2}c$ . Slower moving monopoles are extremely infiltrative; a monopole of mass  $10^{16}\text{GeV}$  may penetrate a million kilometers of rock! Essentially, it travels through Earth rapidly and without losing its velocity. A wide range of detection techniques that are sensitive to the various monopole masses must be used in order to detect a variety of monopole masses.

Over the course of 11 years, from 1989 to 2000, the Monopole Astrophysics and Cosmic Ray Observatory (MACRO), a massive multipurpose underground detector, collected data [51]. Grand Unified Theory (GUT) Monopoles with velocities  $\beta > 4 \times 10^{-5}$  were in the detection range of MACRO. For GUT monopoles with velocities  $\beta > 4 \times 10^{-5}$ , MACRO was able to set a flux limit of  $1.4 \times 10^{-16}\text{cm}^{-2}\text{s}^{-1}\text{sr}^{-1}$  [35]. A combination of Nuclear Track Detectors, layers of liquid scintillators, and streamer tubes filled with a helium-n-pentane gas were used to achieve this result.

The Radio Ice Cherenkov Experiment (RICE), which was carried out in the South Pole in 2008, had as its goal the search for intermediate mass monopoles ( $10^7 \leq \gamma \leq 10^{12}$ ). RICE was a good choice for this search since it had a large effective volume. More importantly, it has the capacity to distinguish between a neutrino event and a monopole that loses a significant amount of energy in the ice. The experiment was also very sensitive to relativistic ( $\gamma \geq 10^6$ ) intermediate mass monopoles, which made it even

more appropriate. The mass of these intermediate mass monopoles would be significantly less than the mass of the typical GUT energy monopoles [52]. RICE was able to establish an upper limit on the monopole flux on the order of  $10^{-18}\text{cm}^{-2}\text{s}^{-1}\text{sr}^{-1}$  without having seen any monopole-like events. This limit that was placed by RICE is greater than the limit placed by MACRO by two orders of magnitude.

Between December 2008 and January 2009, the Antarctic Impulsive Transient Apparatus (ANITA-II) gathered data for 31 days [53]. It was designed to detect ice-generated Cherenkov radiation. The experiment was capable of also determining whether any ultra-relativistic monopoles were present. However, no such ultra-relativistic monopoles were observed, and the experiment set an upper limit on the monopole flux on the order of  $10^{-19}\text{cm}^{-2}\text{s}^{-1}\text{sr}^{-1}$  within the  $\gamma \geq 10^9$  kinematic range.

ANTARES (Astronomy with a Neutrino Telescope and Abyss environmental RE-Search) was yet another experiment designed to detect Cherenkov radiation produced by the ionization of sea water. The Western Mediterranean based underwater telescope ANTARES was composed of modules with photomultiplier detector tubes attached to it to detect Cherenkov radiation from the ionization of sea water [54]. It was deployed at a depth of 2467 meters. It is crucial to remember that, assuming they have the same velocity, relativistic monopoles ( $\beta \geq 0.51$ ) with a charge of  $1.0g_D$  should produce 8550 times more Cherenkov photons than muons [55]. Between 2007 and 2008, 116 days of data was collected and several analyses were made for monopole  $\beta$  bins in the range of  $0.55 \leq \beta \leq 0.995$ . A single monopole-like event was detected in the range of  $0.675 \leq \beta \leq 0.725$ , although it was consistent with the anticipated atmospheric muon and neutrino background. Then, for monopoles in the range of  $0.625 \leq \beta \leq 0.995$ , a 90% Confidence Limit (C.L.) upper limit was defined in the flux range of  $1.3 \times 10^{-17}\text{cm}^{-2}\text{s}^{-1}\text{sr}^{-1}$  and  $8.9 \times 10^{-17}\text{cm}^{-2}\text{s}^{-1}\text{sr}^{-1}$ .

The IceCube experiment is an experiment situated at the South Pole. The pho-

tomultiplier tubes inside each of the 86 strings, which each had 60 digital optical modules, were able to detect Cherenkov radiation. The experiment is covered a volume of one cubic kilometer and was deployed at a depth between 1450 and 2450 meters. There were no observations of monopole-like events throughout the data from the searches for relativistic ( $\beta \geq 0.76$ ) and weakly relativistic ( $\beta \geq 0.51$ ) monopoles in the years 2008 – 2009 and 2011 – 2012 and the monopole flux limit was set at  $1.55 \times 10^{-18} \text{cm}^{-2} \text{s}^{-1} \text{sr}^{-1}$  [56].

SLIM (Search for LIght Monopoles) is a noteworthy experiment that is situated in the Chacaltaya Laboratory (Bolivian Andes), at a height of 5230 meters. A massive array of Nuclear Track Detectors (NTDs) made up this experiment [33]. This detector was sensitive to intermediate mass monopoles ( $10^5 < M < 10^{12} \text{GeV}$ ). The detector was also sensitive to a beta-dependent charge. SLIM boasted a sensitivity to charges of  $2g_D$  in the velocity range of  $4 \times 10^{-5} < \beta < 1$  as well as charges of  $1g_D$  in the velocity range of  $\beta > 10^{-3}$ . However, no monopole-like events were discovered in the NTDs, hence a 90% Confidence Limit (C.L.) upper limit of  $1.3 \times 10^{-15} \text{cm}^{-2} \text{s}^{-1} \text{sr}^{-1}$  was established by SLIM [36].

The Super-Kamiokande experiment in Japan has established a tight limit on the monopole flux and restricted it to a small range. With respect to monopoles of mass greater than  $10^{17} \text{GeV}$ , this limit ranges from  $6 \times 10^{-28} \text{cm}^{-2} \text{s}^{-1} \text{sr}^{-1}$  to  $7 \times 10^{-20} \text{cm}^{-2} \text{s}^{-1} \text{sr}^{-1}$ . This limit was determined using data gathered over a period of more than ten years, from April 1996 to August 2008, totaling 2853 days. Three full cycles of upgrading occurred on the Super-K throughout the time of data collecting [57]. The methodology used in this experiment was to find surplus neutrinos from the Sun with energies of 29.79 MeV. When monopoles begin to amass and catalyze proton decay, neutrinos with such energy are created.

## 1.15 Monopoles in Bound Matter Searches

Colliders and, more recently, cosmic rays have both been the subject of monopole searches in the past. These searches are complemented by the search for matter-trapped monopoles. Typically, these searches are sensitive to smaller mass monopoles. These monopoles may have been produced as secondary particles - a byproduct of collisions between astronomical bodies and high energy cosmic rays. These searches are also sensitive to high mass monopoles, which may have been formed during the creation of the universe, during the Big Bang nucleosynthesis. These monopoles, known as stellar monopoles, may have been trapped in the cores of planets and/or planetary bodies shortly after they were created. Below is a brief summary of these searches; for a more thorough description, see [45].

Through a detector, monopoles in the atmosphere may be collected using a powerful magnet's magnetic field. This would depend on the polarity of the monopole. Over an effective area of 24,000m<sup>2</sup>, such a technique was employed in collecting data. For positively charged monopoles of masses up to 10<sup>7</sup>GeV, a charge range of 1.0g<sub>D</sub> – 12.0g<sub>D</sub> and an energy range of 10<sup>2</sup>GeV – 10<sup>11</sup>GeV a 90% C.L. limit of 4.4 × 10<sup>-16</sup>cm<sup>-2</sup>s<sup>-1</sup>sr<sup>-1</sup> was placed on the monopole flux [58].

The surface of magnetite outcrops that function as attraction sites is a potential area to detect monopoles if they thermalize in the atmosphere. 1000m<sup>2</sup> of a location in the Adirondack Mountains (New York) was examined for positively charged monopoles using a portable extraction device. In the absence of monopoles, a limit on the monopole flux of about 1.6 × 10<sup>-14</sup>cm<sup>-2</sup>s<sup>-1</sup>sr<sup>-1</sup> was placed for monopoles with charge over 1g<sub>D</sub> and mass below 10GeV [39]. If monopoles are thermalized by either the atmosphere or ocean water, they can accumulate in deep-ocean deposits [40–42]. The main benefit of such underwater searches is the massive exposure duration (on the order of a million years), which is also sensitive to larger masses and energies than

above sea level experiments, given the depth of the ocean.

Combining the results of the three separate searches produced the most stringent limit from the ocean searches. Four manganese nodules were extracted utilizing the extraction technique described earlier from the Drake Passage bottom. 1600kg of sediments from deeper oceans with a depth of 4.4km on average was also collected along with 8kg of ferromanganese crust, 2.5cm thick, from the Mid-Atlantic ridge. For cosmic monopoles stopping in the atmosphere or ocean with magnetic charge magnitudes  $1g_D - 60g_D$  and masses below 130GeV, a combined upper limit of  $4.8 \times 10^{-19} \text{cm}^{-2} \text{s}^{-1} \text{sr}^{-1}$  was established. Early in the 1970s, magnetic monopoles were examined using the induction technique in 19.8kg of Moon rock samples obtained during the Apollo missions. The predicted exposure duration for these samples is approximately 500 million years. For cosmic monopoles that would stop within a depth of 4m from the surface of the moon, a monopole flux limit was established at  $6.4 \times 10^{-19} \text{cm}^{-2} \text{s}^{-1} \text{sr}^{-1}$  [59, 60].

Stellar monopoles that were originally produced in the early universe and bound to planetary cores might reappear as being bound to polar rocks. A search for such monopoles was conducted in 2013 using the induction technique to analyze 23.4kg of volcanic rocks from a wide range of locations in the Arctic and Antarctic regions. This search placed a limit of  $1.6 \times 10^{-5} \text{gm}$  at a 90% Confidence Level (C.L.) on the density of stellar monopoles. A stellar monopole flux limit of  $2.2 \times 10^{-14} \text{cm}^{-2} \text{s}^{-1} \text{sr}^{-1}$  was established after this search was expanded to include cosmic monopoles within an energy and mass range that were expected to stop within the Earth.

## 1.16 Searches for Monopoles at Colliders

The  $L_3$  experiment carried out at the Large Electron-Positron Collider (LEP) searched for indirect monopole signatures by looking for the process of  $Z \rightarrow \gamma\gamma\gamma$  [61]. The Standard Model (SM) significantly suppresses this process. The existence of monopoles, which would couple to the Z boson, increases the cross section of this process. The findings of this cross-section analysis were consistent with what Quantum Electrodynamics (QED) predicts, leading to a branching ratio limit of  $\text{BR}(Z \rightarrow \gamma\gamma\gamma) < 0.8 \times 10^{-5}$ . The monopole mass's lower bound was established at 520GeV.

High monopole-photon coupling was the subject of an indirect search at the Tevatron-based  $D\bar{O}$  experiment at a centre of mass energy of  $\sqrt{s} = 1.8\text{TeV}$  [62]. The coupling of a monopole to a photon is several orders of magnitude stronger than the coupling of a photon to an electric charge. This analysis predicted that virtual monopoles will result in photon-photon re-scattering, as was previously indicated in [63, 64]. Lower 95% Confidence Limits (C.L) of 610GeV, 970GeV, and 1580GeV on the masses of a Spin-0, Spin- $\frac{1}{2}$  and Spin-1 Dirac monopole were established respectively since no excess of events were seen in the background.

The MODAL experiment, which ran at a centre of mass energy of  $\sqrt{s} = 91.91\text{GeV}$ , was housed in the  $e^+e^-$  LEP collider and was dedicated to experiments involving monopoles. NTD foils were carefully positioned around the  $I_5$  interaction point at the collider for this experiment. It was expected that monopoles would passing through these NTD foils would leave distinct Highly Ionizing Particle (HIP) tracks. Cross-section limits of 70pb were established as a consequence of the exposure periods in 1990 and 1991, none of which yielded any candidates. These limits were based on the Drell-Yan mechanism. Another effort was undertaken, this time encircling the beam pipe and other components of the OPAL (Omni-Purpose Apparatus at LEP) detector with NTD foils. Cross-sectional limits of 0.3pb were established in this experiment,

likewise assuming the Drell-Yan mechanism [65]. It should be emphasized, nonetheless, that both experiments could only analyze masses up to 45GeV and for charges up to  $2g_D$ .

Monopole signatures of high ionization that were present in the jet chambers were the focus of a search at the Omni-Purpose Apparatus at LEP (OPAL) at  $LEP_2$ . In particular, the tracks that were parallel to the magnetic field of the solenoid were curved. The outcomes of this search improved upon the results obtained by LEP. At a centre of energy  $\sqrt{s} = 206.3\text{GeV}$ , data was collected and upper bounds on the production cross section of monopoles with a charge of  $1g_D$ , a mass range of 45GeV to 102GeV, and were produced via the Drell-Yan mechanism were established at 0.05pb with no monopole-like events having been seen.

A beam pipe from the  $H1$  experiment in the positron-proton ( $e + p$ ) Hadron-Electron Ring Accelerator (HERA) collider at DESY which was running at a centre of mass energy  $\sqrt{s} = 300\text{GeV}$  was used to search for monopoles at colliders. This beam pipe was crucial in the search for monopoles using the induction technique [66]. A cross-section upper limit range was established between 0.06pb to 2pb for monopoles ranging from a charge of  $1g_D$  to  $6g_D$ . After having seen no monopole-like events, a mass limit range of 5GeV to 140GeV was established. The Drell-Yan process is obviously not applicable in positron-proton ( $e + p$ ) collisions, hence it is vital to emphasize that this experiment was predicated on the premise that pair-production of monopoles happened by photon-photon interactions (photon fusion). This investigation was conducted on the assumption that Spin-0 monopoles were produced by elastic collisions, whereas Spin- $\frac{1}{2}$  monopoles were created through inelastic collisions.

Three separate studies were carried out at the Tevatron in an effort to directly isolate monopoles. The induction method was used on detector samples of the  $D\bar{O}$  in the first analysis. The CDF (Collider Detector at Fermilab) detectors that had been sub-

jected to collisions at  $\sqrt{s} = 1.8\text{TeV}$  were used in addition to these samples [67]. For the purposes of this analysis, the Drell-Yan mechanism was assumed, and it was established that the upper limits of monopole production cross-sections for the charges of  $1g_D$ ,  $2g_D$ ,  $3g_D$ , and  $6g_D$  were fixed at 0.6pb, 0.2pb, 0.07pb, and 0.2pb respectively. In a direct analog, lower mass limits were set at 265GeV, 355GeV, 410GeV, and 375GeV respectively. In an effort to identify monopoles, the CDF experiment used collision data with a  $\sqrt{s} = 1.96\text{TeV}$  and a time-of-flight (TOF) trigger that was highly sensitive to any monopole with  $\beta > 0.2$  [68]. The study was built on the monopole signature of high ionization, which is often connected to a track that is consistent with a particle with magnetic charge. After no monopole-like events were seen during the results analysis, the production cross section's upper limit was established at  $10^{-2}\text{pb}$ . For monopoles with a charge  $|g| = 1g_D$ , the Drell-Yan production mechanism was assumed and 476GeV was established as the lower mass limit.

7TeV proton-proton (pp) collisions were studied in the ATLAS experiment at CERN [69]. In order to identify monopole signatures that fall in the monopole mass range of 200GeV to 1500GeV, the Transition Radiation Tracker (TRT) and the Electromagnetic (EM) Calorimeter were both essential to this investigation. However, no monopole-like events were observed and a monopole production cross-section limit of 3fb was established on the production cross section of monopoles with a charge of  $1g_D$  and masses ranging from 200GeV to 1500GeV. Additionally, it was determined that, assuming the Drell-Yan production process, the cross section limit for masses between 200GeV and 1200GeV was between 0.2pb and 0.02pb. A lower mass limit of 862GeV was established for a monopole produced by the Drell-Yan process.

## Chapter 2

# The Large Hadron Collider and MoEDAL

*“Work is love made visible; if you cannot work with love but only with distaste, it is better that you should leave your work.” - Khalil Gibran*

### 2.1 The Large Hadron Collider

The CERN accelerator complex shown in Figure 2.1 is made up of a multitude of machines, one after another. This design is not accidental; its purpose is to gradually ramp up the energy of the proton beam by passing the beam from one machine to the next and finally into the LHC where it reaches energies of 7TeV [70].

Protons are obtained by stripping Hydrogen gas of its electrons in the Linear Accelerator (LINAC 2) in transit through an electric field and it reaches an energy of 50MeV. The proton beam then enters the Proton Synchotron Booster (PSB) where it will reach an energy of 1.4GeV, proceeds onto the Proton Synchrotron (PS) where it will reach an energy of 25GeV, and then the Super Proton Synchrotron (SPS) where it will reach an energy of 450GeV. After the SPS, the proton beam reaches the LHC where it will be accelerated to 7TeV as mentioned above and it can stay there for up

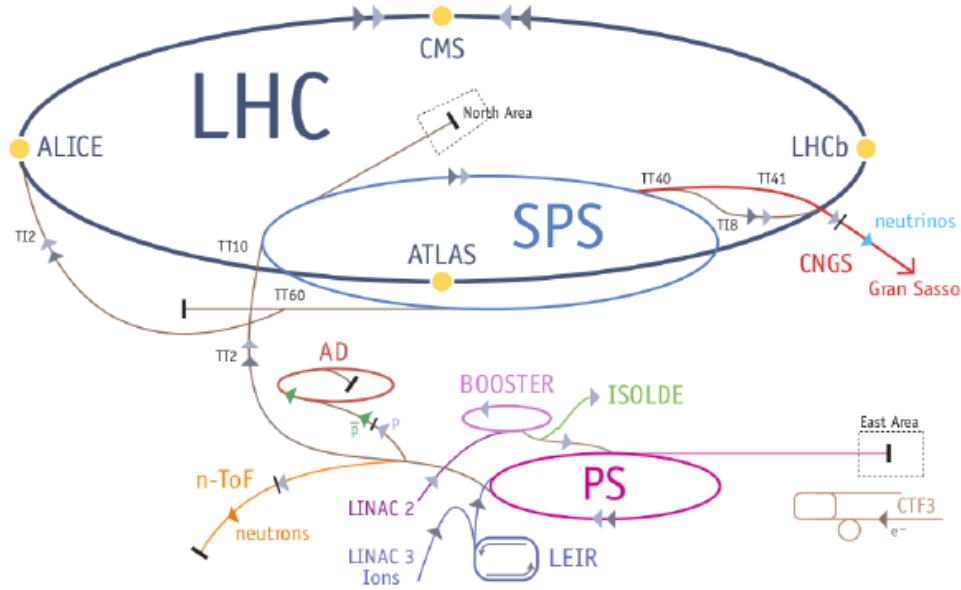


Figure 2.1: CERN Accelerator Complex

to 15 hours on average [70].

The two ring superconducting hadron accelerator and collider that is the LHC is housed in a 26.7km tunnel. The tunnel was formerly occupied by the Large-Electron-Positron (LEP) collider. The particles (i.e the protons) that circulate the LHC traverse in a vacuum tube and their somewhat circular orbit is kept by dipole magnets. The beam is focused by quadrupole magnets and the beam is accelerated by electromagnetic resonators. The proton beam consists of 2808 bunches with  $10^{11}$  protons per bunch on average with a bunch spacing of 25ns. For a given process, the number of events generated per second in the LHC collisions is given by:

$$N_{event} = L\sigma \quad (2.1)$$

where  $L$  is the machine luminosity and  $\sigma$  is the cross section of the process of interest. The luminosity for a Gaussian beam distribution depends on different beam parameters and can be described by:

$$L = \frac{N_b^2 n_b f_{rev} \gamma_r}{4\pi \epsilon_n \beta^*} F \quad (2.2)$$

where  $\beta^*$  is the beta function at the collision point,  $f_{rev}$  is the revolution frequency,  $\gamma_r$  is the relativistic gamma factor,  $N_b$  is the number of particles per bunch,  $\epsilon_n$  is the normalised transverse beam emittance,  $n_b$  is the number of bunches per beam and  $F$  is the geometric luminosity reduction factor. By definition, the unit of cross section is in barn where  $1 \text{ barn} = 10^{-28} \text{ m}^2$ . Naturally, different processes in physics will have different cross sections and it is obvious that the rarer the process, the lower the cross section (i.e. the probability of occurrence of an event is proportional to the cross-section). Therefore, to observe rare processes, one should increase the luminosity with respect to time. The LHC is able to deliver a maximum integrated luminosity of  $80 \text{ fb}^{-1} - 120 \text{ fb}^{-1}$  per year [70]. Suppose BSM physics is not observed; we can then set a cross-section limit for that particular process, which describes the constraint on the production of the particle with respect to that particular cross-section value. This serves as a basis of comparison between experiments. Started in 2015, the Run-2 of the LHC currently operates at 13TeV although it has plans to reach 14TeV in the near future during Run-3 of the LHC also known as the High-Luminosity LHC (HL-LHC).

## 2.2 The MoEDAL Detector

MoEDAL, the Monopole and Exotics Detector at the LHC, is an experiment designed to increase the physics reach of the LHC complementary to the sledgehammer experiments of CMS and/or ATLAS. MoEDAL's primary objective is the search for the monopole but it includes searches for Dyons, HIPs and/or Stable Massive Particles (SMPs). MoEDAL is located at IP8 along with LHCb's experiment and is deployed around LHCb's Vertex Locator (VELO) [71]. However, the High Charge Catcher (HCC) region (only during Run-2 of the LHC) of the NTD detector is placed inside the LHCb detectors acceptance between LHCb's RICH (ring-imaging Cherenkov) and the TT1 (first upstream tracking detector tracking station) detectors.

MoEDAL is extremely unique and consists of three main detector systems: the Magnetic Monopole Trappers (MMTs), the Nuclear Track Detectors (NTDs) and the TimePix detector. NTDs are placed in stacks around the interaction point. Its purpose is to indicate the passage of HIPs as it passes through the NTDs and it is optimized to search for a range of charges of which the monopole charge is a subset. MMTs are comprised of a ton of aluminium samples cut up into rectangular cuboids. They are designed to trap HIPs which will then be measured by a superconducting magnetometer known as a SQUID. The purpose of the TimePix is to monitor the radiation in the cavern. Notice that while the NTDs and MMTs are passive, the TimePix is active. One advantage of a passive detector is that the experiment remains model-independent and is also independent on any electronic readouts (which can cause build-up and other problems therefore leading to limitations imposed on such active detectors such as electronic triggers).

Another main feature of MoEDAL is the absence of background noise in the sense that BSM physics can be easily identified unlike CMS and/or ATLAS. The MoEDAL detector is exemplified by its ability to retain a permanent record, and even cap-

ture new particles for further study. The NTDs provide a tried-and-tested and cost effective method to accurately measure the track of a HIP and its effective charge. Importantly, the NTD response was directly calibrated using heavy-ion beams at the CERN SPS. The second detector system, the MMT, ensures that a small but significant fraction of the HIPs produced are slowed down, stopped and trapped for further study in the laboratory. It is highly unlikely that any known particle in the SM is able to mimic the signature of a monopole in the MMTs and/or the NTDs. Thus, even the detection in MoEDAL of few HIP messengers of new physics would herald a discovery.

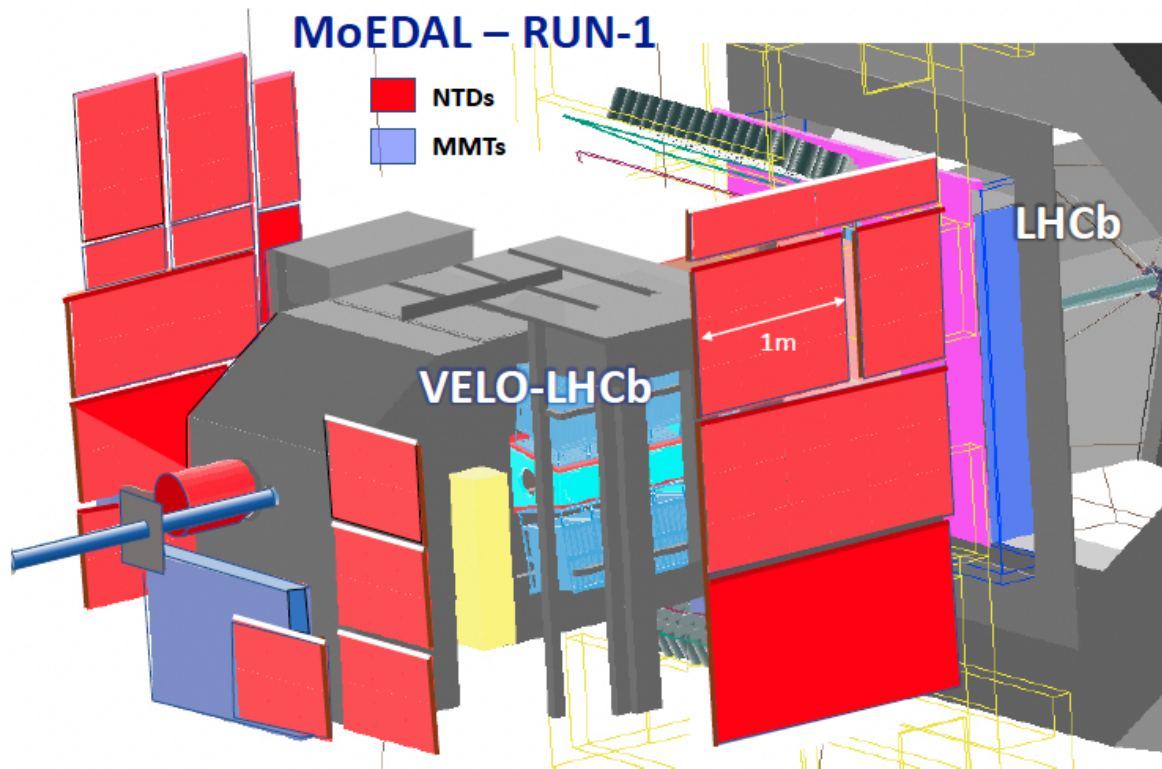


**Figure 2.2:** A GEANT-4 Panoramix view of the MoEDAL detector prototype deployed at IP8 during LHC's Run-1.

### 2.2.1 Nuclear Track Detectors

Each NTD stack shown in Figure 2.4 comprises of 3 sheets of 1.5mm thick CR39, 3 sheets of 0.5mm thick MAKROFOL and 3 sheets of 0.25mm thick LEXAN sheets in that particular order making it a total of 9 sheets [71–73]. The 9 sheets are kept in an Aluminium bag. Currently the Lexan foils serve as protective layers and are not

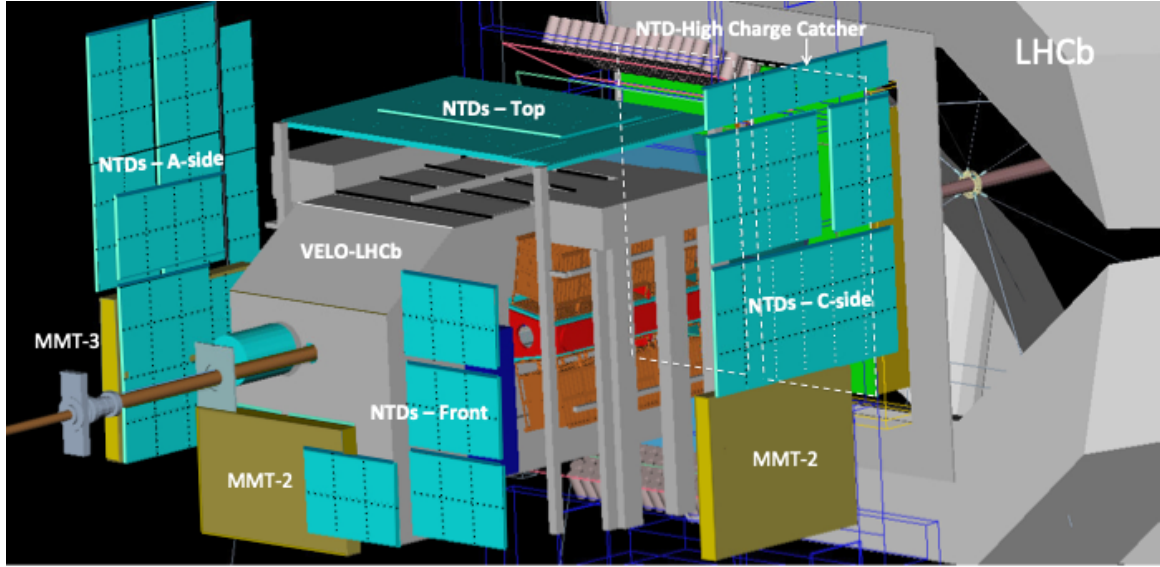


**Figure 2.3:** A GEANT-4 Panoramix view of the MoEDAL detector deployed at IP8 during LHC’s Run-2.

analyzed. The trajectory of a HIP traversing through the NTD stack leaves ”damage” marks on the NTD stack. The NTDs are then etched (a process that involves the application of hot sodium hydroxide or potassium hydroxide solution to the NTD) which reveals the damage zones as cone-shaped pits which are called etch pits. The NTD sub-detector system is calibrated using heavy-ion beams at NASA Space Radiation Laboratory (NSRL) and Brookhaven National Lab (BNL) [71–73].

After etching, the plastic is scanned. This can be done using computer controlled optical scanners and/or manually controlled optical scanners. The scanners are able to detect the etch pits to an accuracy of  $\approx 50\mu\text{m}$ . After the etch pits are detected, the trajectory of the HIP is reconstructed through the NTD stack by tracking the successive etch pits.

For the LHC Run-1 analysis, only the Makrofol NTDs were utilized. This is due to roughly a factor ten higher detection threshold in Makrofol than CR39 which results in substantially less visual noise in the etched plastic due to spallation products arising from beam backgrounds. Thus, the analysis of the CR39 NTDs is considerably more time intensive. HIPs produced in LHC collisions during Run-1 of the LHC,

are sufficiently highly ionizing that they can easily be detected with the Makrofol NTDs obviating the need to scan the CR39. MoEDAL's NTD sub-detector system is sensitive to HIPs with an ionizing power greater than around  $\frac{7}{55}$  times that of a minimum ionizing particle such as a relativistic muon, for the 3 CR39/Makrofol foils comprising an NTD stack. During Run-1 of the LHC, the NTD sub-detector system comprised of 125 stacks of NTD. During Run-2 of the LHC, the NTD sub-detector system was upgraded to 186 stacks of NTD. Each stack measured  $25\text{cm} \times 25\text{cm}$  during both Run-1 and Run-2 of the LHC. Therefore, the total area of NTDs deployed during Run-2 of the LHC was  $122\text{m}^2$ , including the area of the High Charge Catcher (HCC). The exposed NTD plastic is removed at the end of each year of data taking and fresh plastic is put in place. Of course, in the event of the observation of a candidate event in the Makrofol, all 6 NTD sheets in the stack would be analyzed. Consequently, a permanent record of the passage of a HIP is obtained.

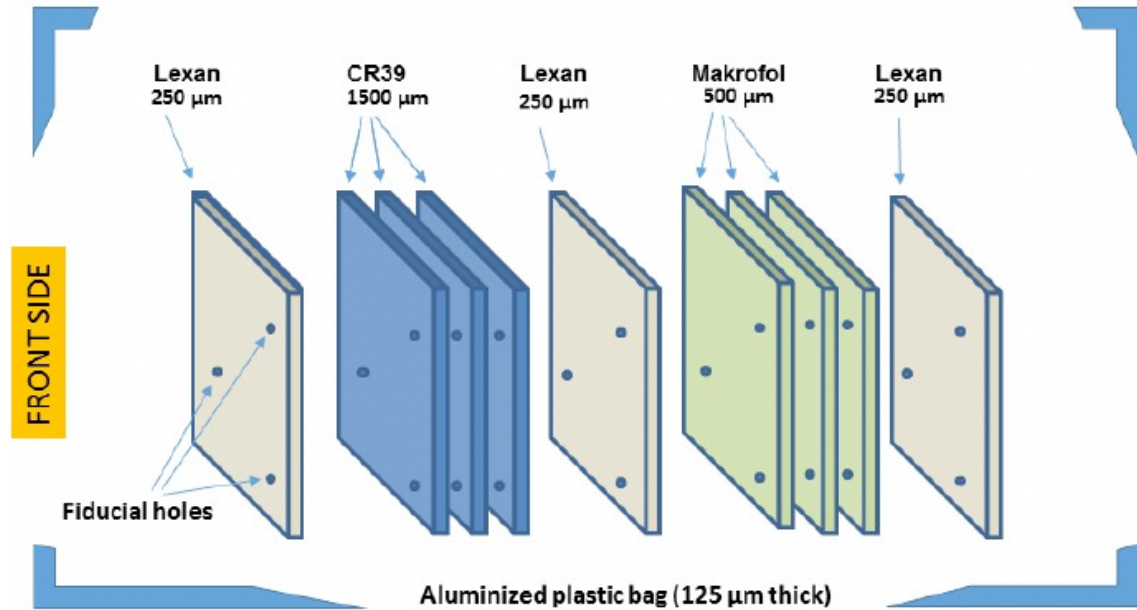


Figure 2.4: NTD module composition

## 2.2.2 Magnetic Monopole Trappers

The prototype MMT detector deployed for LHC's Run 1 was comprised of 198 aluminium rods weighing a total of 163kg. These rods were housed in an enclosure

placed just underneath the beampipe at the upstream end of LHCb's VELO detector as shown in Figure 2.5. The full MMT detector, deployed for LHC's Run 2, utilizes a 800 kg trapping detector (MMT) comprised of 2400 Aluminium (Al) bars to capture HIPs for further study. In this case there are three enclosures, one under the beampipe, as in the Run-1 detector plus one on each side of the VELO detector as shown in Figure 2.2. Aluminium is chosen as the material for 3 reasons:

- a trapped monopole will be strongly bound to the aluminium due to the large magnetic moment [37]
- aluminium is cheap is readily available
- aluminium is non magnetic and therefore, during SQUID superconducting magnetometer measurements, the measurements will remain stable



**Figure 2.5:** A photograph of the prototype MMT detector deployed at IP8.

After exposure the MMT's aluminium volumes are sent to the ETH Zurich Laboratory for Natural Magnetism where they are passed through a SQUID magnetometer to

scan for the presence of trapped magnetic charge. A monopole will stop in the MMT detector when its speed falls below  $\beta \leq 10^{-3}$ . It then binds due to the interaction between the monopole and the nuclear magnetic moment [74–77] of an aluminium nucleus comprising a MMT trapping volume.

The anomalously large magnetic moment of an aluminium nucleus gives rise to a monopole-nucleus binding energy of 0.5-2.5 MeV [74], comparable to the shell model splittings. In any case, it is reasonable to assume that the very strong magnetic field of the monopole will rearrange the nucleus, permitting it to bind strongly to the nucleus. As reported in Ref. [74] monopoles bound in such a way would be trapped indefinitely. It would require fields well in excess of several Tesla for the lifetime of the trapped monopole state to compromise its detection by the MoEDAL trapping detector. We note that the MoEDAL detector is only subject to fields lower than  $\sim 10mT$ .

### 2.2.3 TimePix

The background radiation in the MoEDAL/VELO cavern is measured by the TimePix detector. The TimePix detector uses  $300\mu m$  wafer of n-type silicon for its sensitive element and the readout electronics is an application specific integrated circuit (ASIC) onto which the sensor is bump-bonded. There are three different modes on the readout electronics: Medipix mode for photon counting, TimePix mode for the time of arrival of the photon and time-over-threshold (ToT). It ‘visualizes’ radiation using the ToT mode. Each pixel stores the length of time the charge measured by that pixel spends above a preset threshold value. In return, each activated pixel will return an analogue to digital count (ADC) associated with its  $x$  and  $y$  position where 1 count represents  $0.1\mu s$ . The count value is dependent on: the energy deposited in the sensor per unit length (i.e.  $\frac{dE}{dx}$ , also known as linear energy transfer or LET), the distance of the sensor interaction from the pixel readout pad and the detector settings. Each particle or photon activates a certain region of pixels and they differ from one another (i.e.

a photon will activate a different set of pixels compared to an alpha particle). The groups of activated pixels adjacent to each other are known as clusters and there is a systematic approach to classifying the clusters so as to identify with particle or photon set off those clusters. The TimePix chip itself comprises of a preamplifier, a discriminator with threshold adjustment, synchronisation logic and a 14-bit counter. The TimePix in ToT mode is equivalent to a tiny bubble chamber providing real-time measurements of energy depositions in the cavern [72, 78].

### 2.2.4 Conclusion

In conclusion, MoEDAL is designed to have superior sensitivity to HIPs compared to other general purpose collider detectors such as ATLAS and CMS. This meliority is due to several factors. Firstly, MoEDAL has a relatively small amount of material between the interaction point and the detector systems. MoEDAL has, on average, 1.4 radiation lengths between the interaction point and the detector system. This results in a smaller number of HIPs that would be absorbed between MoEDAL and the interaction point as compared to a massive collider detector.

Secondly, a HIP need only penetrate a relatively low mass of the detector volume before a measurement is made. This is, on average, simply the mass of a single element of the MMT detector. Thirdly, the lack of Standard Model backgrounds is unique to MoEDAL. This ensures that the presence of a magnetically charged particle can be detected using a SQUID. Lastly, MoEDAL is a passive detector without the need for an electronic trigger. This means that there is almost no chance of missing new physics should they occur.

## Chapter 3

# Searches in MOEDAL

*"What do you mean less is more? More is more!" - Yngwie Malmsteen*

### 3.1 Magnetometer Measurements

A SQUID is a mechanism used to measure extremely weak magnetic fields. It employs the use of a Josephson junction. A Josephson junction is a type of electronic circuit capable of switching at very high speeds when operated at temperatures approaching 0K, thus exploiting the phenomenon of superconductivity which is the ability to conduct electrical current at practically zero resistance (for certain materials only). It is made up of two superconductors separated by an insulating layer thin enough for electrons to tunnel through. Before every run, the belt attached to the SQUID is cleaned thoroughly with ethanol. The SQUID was calibrated by sending a long thin solenoid with known properties and current through the sensing coil. The long and thin solenoid mimics a monopole. The output is then measured before, during and after the passage of the sample through the sensing coil. The measurement with the empty holder is subtracted from the measurement with the sample in the holder. The persistent current which is the difference between the resulting current before and after the sample is passed through the sensing coil is recorded. A deviation from zero would indicate the signature of the monopole. The SQUID is extremely sensitive

and therefore prone to even the slightest of vibrations such as a train passing or a car starting outside the lab. For this reason, the measurement with the empty sample holder is made.

The SQUID is used to detect the presence of monopoles whose characteristic is an induced non-decaying current. The SQUID also needs to be calibrated before being able to measure monopoles. The SQUID used for the purposes of this report is housed in Zurich and kept by ETH Zurich, the Swiss Federal Institute of Technology Zurich. A schematic outline of the magnetometer together with an illustration of the magnetic field configuration arising from a solenoid (one end of which is a pseudopole), near two superconducting pick-up coils is shown in Figure 3.1.

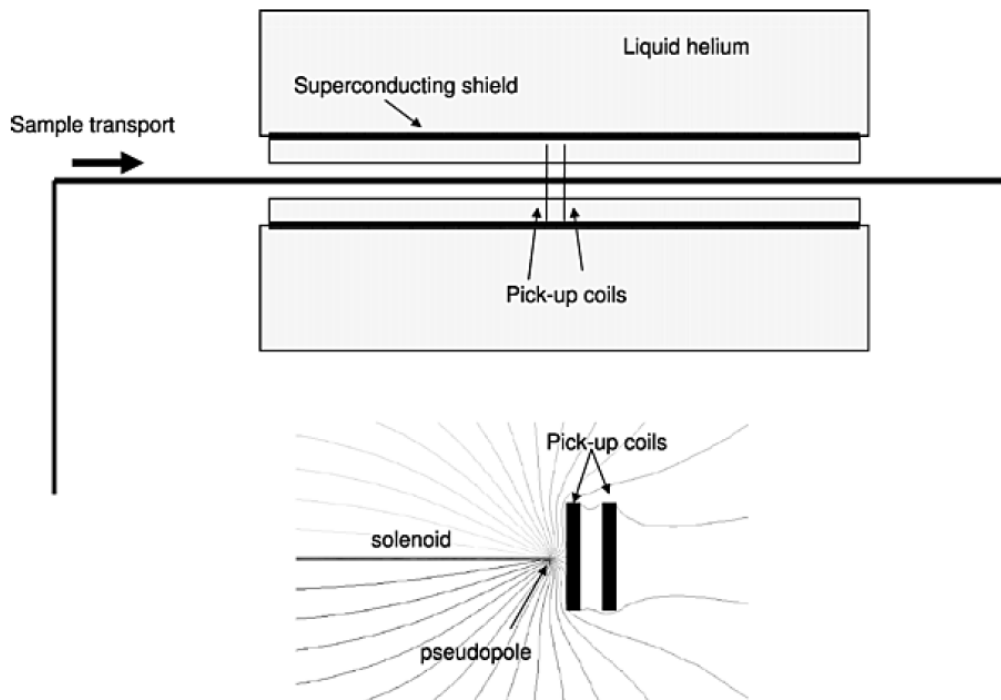


**Figure 3.1:** Top: schematic representation of the magnetometer used in this work. Bottom: magnetic field configuration of pseudopole near two superconducting pick-up coils

### 3.1.1 Calibration of Magnetometer

To calibrate the magnetometer, a needle of  $14\text{mm}$  in length and  $1\text{mm}$  diameter enclosed in a non-magnetic plastic holder is used. The dipole sample was made from

floppy disk material and was subsequently magnetised such that the dipole moment, aligned along the longitudinal direction, is  $3.02 \times 10^{-6} \text{Am}^2$ . The uncertainty on the moment is less than 1% as assessed by comparing measurements with independent magnetometers at the ETH laboratory. The measurements of the calibration sample can be used to predict the magnetometer response to a monopole, using the direct method described in the next sub-section.

### 3.1.2 Expected Magnetometer Response to Monopoles

Here, we take a look at two methods, the direct approach and the convolution method, used to gauge the magnetometer response to a monopole. The direct approach is described in detail in the following sub-sub-sub-section while the convolution approach is briefly described. For a detailed discussion on the estimated uncertainties in the two methods, refer to Section 3 in [79].

#### The Direct Approach Using a Long Solenoid

A long solenoid is used to mimic a monopole response since the  $B$ -field from one end of a long (semi-infinite) solenoid obeys the inverse square law [80].  $S1$ , a thin solenoid formed with two layers of copper wound around it and  $S2$ , a thin solenoid formed with three layers of copper wound around it are used for the calibration. The interaction between the oppositely charged poles of the solenoid is given by

$$q = \frac{I \times S \times n}{l} \quad (3.1)$$

where,  $n$  is the number of turns on the solenoid. Its length and surface area are given by  $l$  and  $S$  respectively and  $I$  is the applied current. In units of Dirac charge  $g_D$  and the current flowing through the solenoids, the pseudopole strength is given as  $32.4g_D$  for  $S1$  and  $41.4g_D$  for  $S2$  per unit  $\mu\text{A}$ .

### The Convolution Method

We can also gauge the magnetometer response to a monopole by using currents from a calibration sample. The current increases to a maximum value for a length directly proportional to the longitudinal extent of the pick-up coil array which is approximately 4cm and then decreases again. Invoking the superposition principle for magnetic fields, we see that the field for a long thin magnet is equivalent to the sum of many individual dipoles positioned tip-to-tail such that the length of the long thin magnet equals the total length of the individual dipoles. We can therefore use the magnetometer response at a number of dipole positions whose sum will then equal the value of a long thin bar magnet acting as a pseudopole.

#### 3.1.3 MMT samples

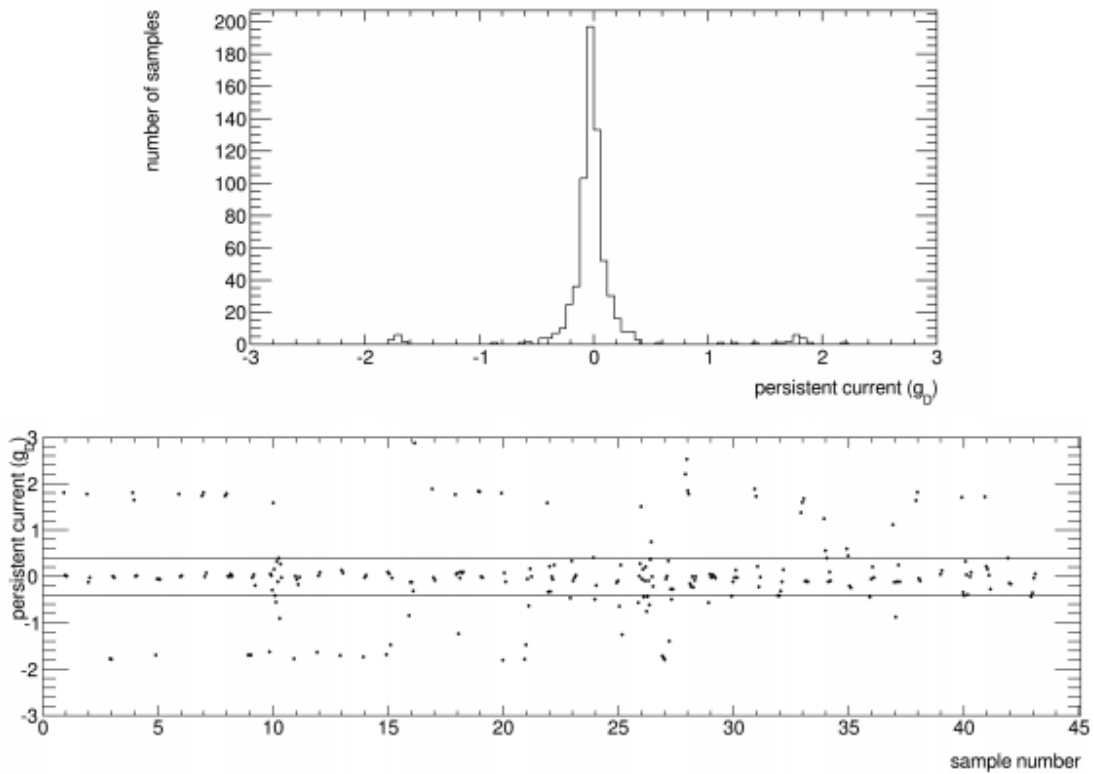


**Figure 3.2:** Top: persistent current (in units of  $g_D$  after application of a calibration constant) after first passage through the magnetometer for all samples. Bottom: results of repeated measurements of candidate samples with absolute measured values in excess of  $0.4g_D$ .

The 672 exposed aluminium samples of the MoEDAL forward trapping detector array were scanned in Spring 2017 during a two-week campaign with a DC SQUID long-core magnetometer (2G Enterprises Model 755) located at the laboratory for natural magnetism at ETH Zurich. Each sample was passed through the sensing coil at least once, with measurements of the magnetometer response in all three coordinates before, during, and after passage. The persistent current, defined as the difference between the measured responses in the z coordinate (along the shaft) after and before passage of the sample through the magnetometer sensing coil, to which the contribution of the conveyor tray is subtracted. A calibration factor obtained from special calibration runs using two independent methods as described in Section 3.3.2 is used to translate this value into the measured magnetic charge in the samples in units of Dirac charge. Persistent currents measured for all 672 samples for the first passage are shown in the top panel of Figure 3.2. Samples for which this measurement significantly deviates from zero are set aside as candidates for further study.

The threshold in the absolute value of the persistent current beyond which a sample is selected as a candidate is chosen to be greater than  $0.4g_D$  as a compromise between allowing sensitivity to magnetic charges down to  $1g_D$  and the time and effort required to scan a number of samples multiple times. This gives 43 candidates, which were remeasured at least two more times each, as shown in the bottom panel of Figure 3.2. These multiple measurement do not yield consistent non-zero persistent current values, confirming that all candidates identified in the first pass were false positives. During this measurement campaign, the identification of false positives was dominated by two effects. The first effect, which was already observed in the previous runs [81], tends to happen with samples containing dipole impurities: whenever the sample magnetisation results in a flux inside the SQUID loop which temporarily exceeds the fundamental flux quantum  $\Phi_0 = \frac{h}{2e}$ , there is a chance that the response does not quite come back to the same level during the flux change in the other direction, causing a slight offset with value around  $\pm 1.8g_D$ . Measuring such samples multiple times will

occasionally result again in an offset, faking the response of a monopole with charge  $\pm 1.8g_D$ ; however, unlike what a genuine monopole would produce, it also occasionally yields zero, and turning the sample around such as to reverse its magnetisation in the  $z$  direction consistently reverses the sign of the offset. The second effect is a slight degradation of the resolution of the  $z$  measurements due to large random flux jumps occurring in the  $x$  and  $y$  directions. These jumps are related to imperfect grounding of the metallic shields of the magnetometer and will be eliminated for the next measurements. Tests performed with aluminium samples and rock samples confirm that the jumps in  $x$  and  $y$  do not impact the reliability of the measurement in the  $z$  direction besides resulting in small fluctuations which simply degrade the resolution.

Special care is given to the assessment of the probability for false negatives (the possibility that a monopole in a sample would remain unseen in the first pass due to a spurious fluctuation cancelling its response and resulting in a persistent current below the  $0.4g_D$  threshold used to identify candidates). This is studied using the distribution of persistent currents obtained in samples without monopoles (top panel of Figure 3.2), assuming that the magnetic field of the monopole itself (small compared to those of magnetic dipoles contained in the sample and tray) does not affect the mismeasurement probability. The distribution can be very well fitted using a sum of four Gaussians (two centred around zero, and two around  $\pm 1.8g_D$ ). The probability to miss a monopole is then estimated by integrating the fitted function in the relevant intervals: it is found to be less than 0.02% for a magnetic charge  $\pm 1g_D$ , less than 1.5% for a magnetic charge  $\pm 2g_D$ , and negligible for higher magnetic charges. Resulting from this study, a conservative detection efficiency of 98% is assumed for the final interpretation.

Expressed in units of the Dirac Charge, the magnetic pole strength,  $P$ , contained in an MMT sample is given by

$$P = C \cdot [(I_2 - I_1) - (I_2^{tray} - I_1^{tray})] \quad (3.2)$$

where  $C$  is the calibration constant,  $I_1$  and  $I_2$  are the currents measured before and after the MMT sample has passed through the sensing coil of the SQUID respectively and  $I_2^{tray}$  and  $I_1^{tray}$  are the currents measured before and after the empty tray has passed through the sensing coil of the SQUID respectively. The contributions from the empty trays result from minute, seemingly random variations in the SQUID measurement, primarily as a result of imperfect grounding of the magnetometer electronics. It should be noted that the tray itself is made of G10, a fiberglass-epoxy composite that is neither metallic nor magnetic and cannot be used to increase or shield the magnetic signal. Two independent methods - detailed descriptions of which may be found in Ref. [79] as well as the section above — are used to calibrate the magnetometer response. The difference between the two approaches is  $\sim 10\%$ , which we take to be the calibration error in the pole strength. Within a range of  $0.3g_D$  to  $300g_D$ , the magnetometer response is shown to be linear and charge-symmetric. The plateau value of the calibration dipole sample was periodically remeasured during Run-2 and was discovered to be steady to within less than 1%. The SQUID had an update in 2018, with the key advancement being improved grounding across the magnetometer mechanics and electronics. The observed variations in magnetometer values were significantly reduced as a result.

## 3.2 Simulations at MoEDAL

We now study how the monopoles interact with the MMTs and NTDs and in particular, with what probability is a monopole with a certain spin and certain mass produced by a certain mechanism is trapped in the MMTs (i.e. stopped in the MMTs) and/or interacts with the NTDs. To this end, we make use of the GEANT4 toolkit [82] to produce simulations (which take into account the equations of motion and the model of production of monopoles) of the monopole traversing through the LHCb VELO, losing its energy and stopping inside one of the MMTs [83–85]. The simulations of the trapped monopoles are then reconstructed using LHCb’s Gauss Software [86].

The simulation process involves a series of steps called the Full Chain of Monte Carlo production that range from generating physics events to reconstructing detector processes.

The simulations involving the GAUSS software package requires heavy computation. When one or two samples are being simulated through GAUSS, it is traditional to use the CERN Computing Cluster, LXPLUS [87]. However, with a sample size greater than 10, it is not recommended to use LXPLUS. Instead, Ganga and DIRAC is used for sending computing jobs to the GRID [88, 89].

### 3.2.1 Event Generation

The first step in the Full Chain is the event generation which produces the final state monopoles according to the model of production specified by the user. There are many event generators for the many different kinds of physics processes. More often than not, the final state particle and model of production is not included in the event generator and has to be defined by the user. Here, we use MadGraph [90], a tree level matrix element generators specialised on simulation of hard scattering processes via perturbative Quantum Chromodynamics (QCD). For the purposes of this report,

we created 12 different user models in MadGraph. Other event generators analogous to MadGraph include Alpgen [91] and AcerMC [92]. Full event generators such as PYTHIA [93], Herwig++ [94] and SHERPA [95] simulate the nonperturbative parton showering, hadronisation and underlying event. Here, PYTHIA is interfaced with Gauss. At MoEDAL however, we are unconcerned with the parton showering and hadronisation. PYTHIA is used solely to give the initial boost to the monopoles in the z direction for our purposes.

### 3.2.2 Monopole Models in MadGraph5

It must be noted that MG5 (MadGraph5) has no provision for the monopoles or HECOs in its standard library of particles. Therefore, a monopole model or HECO model has to be implemented. One can do this by visualizing the monopole as a point particle.

For the Spin-0 model, the monopole was simulated as a scalar boson with magnetic charge in units of  $g_D$ . For the Spin- $\frac{1}{2}$  model, the monopole was simulated as a fermion with magnetic charge in units of  $g_D$ . For the Spin-1 model, the monopole was simulated as a vector boson with magnetic charge in units of  $g_D$ .

### 3.2.3 Simulating the Energy Loss of Monopoles

The GEANT4 toolkit is used to simulate the energy loss of a monopole travelling through the cavern of LCHb. The modified Bethe-Bloch formula in Equation 24 is used to model the beta-dependent energy loss [30, 96]. For slow monopoles, with  $10^{-4} < \beta < 0.01$ , Ahlen and Kinoshita gives a very good approximation for the energy loss [96–98]:

$$-\frac{1}{\rho} \frac{dE}{dx} = (f_n + f_c) \frac{g^2}{g_D^2} \beta \quad (3.3)$$

where  $f_n$  is the contribution from the non-conduction electrons,  $f_c$  is the contribution from the conduction electrons,  $\rho$  is the density of the medium through which the monopole punches through. Naturally, the values of  $f_n$  and  $f_c$  are material dependent. We only concern ourselves with Aluminium, Steel and Copper, the three dominant materials in MoEDAL [99]. Linear interpolation is used to estimate energy loss for the intermediate velocity range.

The monopoles are not highly relativistic due to their sheer massiveness. Therefore, energy losses via bremsstrahlung and pair-production which become significant only at ultra-relativistic energies should not concern us. It will not affect the monopole trajectory and/or trapping acceptance in any significant manner.

### 3.2.4 Simulation of Trapping Monopoles

The GEANT4 toolkit which is able to simulate the energy loss of a monopole traversing the LHCb cavern is also able to determine the stopping position of a monopole in the MMTs. In the toolkit, if the monopole has  $\beta \leq 10^{-3}$ , the monopole is considered to have stopped. This is because, in models describing the energy losses of monopoles,  $\beta = 10^{-2}$  implies that the monopole will only travel a few more millimeters in aluminium before stopping [99].

### 3.2.5 MMT Trapping Acceptances

The acceptance of the MMT prototype is defined for each event as the probability that at least one monopole, produced in the collision, stops inside one of the aluminium bars contained within the MMT.

### 3.2.6 NTD Acceptances

For the NTDs, the acceptance of a HIP is determined in part by the Restricted Energy Loss (REL). For  $\beta < 10^{-2}$ , the REL is equal to the particle's total energy loss

in the medium. At larger velocities, REL is the fraction of the electronic energy loss leading to the formation of  $\delta$ -rays with energies lower than a cut-off energy  $T_{max}$ . The REL can be computed from the Bethe-Bloch/Ahlen formula restricted to energy transfers  $T < T_{max}$  with  $T_{max}$  a constant characteristic of the medium. For Makrofol,  $T_{max} \leq 350\text{eV}$ . The REL of the travelling HIP is calculated. Then, using the calibration data, the maximum angle,  $\delta_{max}$  that the HIP is able to impinge on the Nuclear Track Detector (NTD) while still being detectable is determined. The actual angle  $\alpha$ , formed when the HIP impinges on the NTD, is checked. If  $\alpha < \delta_{max}$ , we accept the HIP. Else, the HIP is rejected.

The equations of REL are different for HECOs and monopoles.

$$REL_{HECO} = K \frac{Z_{eff}}{A} \frac{z^2}{\beta^2} \left( \frac{1}{2} \log(2m_e c^2 \omega(\gamma\beta)^2) \frac{1}{I^2} - \frac{\beta^2}{2} \left( 1 + \frac{T_{Upper}}{T_{max}} \right) - \frac{\delta}{2} \right) \quad (3.4)$$

where

- if  $X < X_0$  :  $\delta = 0$  or  $X_0 < X < X_1$  :  $\delta = 4.6052X + d + a(X_1 - X)^m$  or  $X > X_1$  :  $\delta = 4.6052X + d$
- $X = \log_{10}(\eta)$
- $\eta = \gamma\beta$
- $Z_{eff} = z \left( 1 - e^{-137 \times 0.95 \times \beta z^{-\frac{2}{3}}} \right)$
- $T_{max} = 2m_e c^2 \eta^2$
- $v_p = \sqrt{N_A \rho \frac{Z}{A} \frac{e^2}{\pi m_e}}$
- $d = 2 \log \left( \frac{I}{h v_p} \right) - 1$
- $a = - \left( d + \frac{4.6052 X_0}{(X_1 - X_0)^m} \right)$

- $K = 0.307075$ ,  $m_e c^2 = 0.511\text{MeV}$ ,  $\rho = 1.21$ ,  $m_e = 9.10938 \times 10^{-28}\text{kg}$ ,  $h = 4.136 \times 10^{-15}$ ,  $e = 4.803 \times 10^{-10}$

For Makrofol we have that  $A = 254.284$ ,  $Z = 230$ ,  $\omega = 350\text{eV}$ ,  $T_{upper} = 350\text{eV}$ ,  $I = 100\text{eV}$ ,  $X_0 = 0.2$ ,  $X_1 = 0.3$ ,  $m = 0.3$ .

$$REL_{MM} = \frac{\omega_p^2 g_D^2}{c^2} \left[ \ln \left( \frac{1.123 \beta \gamma c \sqrt{\epsilon - 1}}{b \omega_p} \right) - \frac{1}{2} \right] \text{ for } \beta < \frac{1}{\sqrt{\epsilon}} \quad (3.5)$$

$$REL_{MM} = \frac{\omega_p^2 g_D^2}{c^2} \left[ \ln \left( \frac{1.123 c}{b \omega_p} \right) - \frac{1 - \beta^{-2}}{2(\epsilon - 1)} \right] \text{ for } \beta > \frac{1}{\sqrt{\epsilon}} \quad (3.6)$$

where

- $\omega_p^2 = \frac{4\pi N_e e^2}{m_e}$
- $\frac{\epsilon}{\epsilon - 1} = \frac{0.5621 I}{\hbar \omega_p}$
- $b = \frac{1.123 \hbar c}{\sqrt{2 m_e c^2 \omega_0}}$  is the minimum impact parameter below which the production of  $\delta$  rays (electrons with energy above  $\omega_0$ ) occurs
- $N_e$  is the electron density
- $I$  is the mean ionization potential

For Makrofol we have that,  $I = 100\text{eV}$ ,  $\epsilon = 1.1994$  and  $\omega_0 = 350\text{eV}$ .

Equation 3.4 describes the REL of a HECO while Equations 3.5 and 3.6 describe the REL of a monopole depending on its velocity.

When the REL has been computed, we then need to determine  $\delta_{max}$ , the maximum angle that the particle is able to impinge on the Nuclear Track Detector (NTD) while still being detectable. This is done via the calibration curve. We will postpone the discussion of calibration and acceptance when we discuss the full analysis of the LHC Run 1 Data.

### 3.3 Full Analysis of LHC Run 1 Data

*Using  $2.2\text{fb}^{-1}$  of  $p-p$  collision data collected at a centre of mass energy ( $E_{CM}$ ) of  $8\text{TeV}$  by the MoEDAL detector during Run-1 of the LHC, a search for highly electrically charged objects (HECOs) and magnetic monopoles is presented. The prototype Nuclear Track Detector array and Trapping Detector array from MoEDAL were used to collect the data. The findings are explained by the three spin hypotheses (Spin-0, Spin- $\frac{1}{2}$  and Spin-1) and the Drell-Yan pair production of stable HECO and monopole pairs. With mass limits ranging from  $590\text{GeV}$  to  $1\text{TeV}$ , the search places limits on the direct production of magnetic monopoles with one to four Dirac magnetic charges ( $1g_D - 4g_D$ ). In addition, HECO are given mass limits for masses between  $30\text{GeV}$  and  $1\text{TeV}$  for charges between  $10e$  and  $180e$ , where  $e$  is the charge of an electron.*

#### 3.3.1 Introduction

Accelerator centres have been engaged in active research in the search for Highly Ionizing Particle (HIP) avatars of physics beyond the Standard Model (SM) for several decades [69, 71, 72, 100–113]. Cosmic rays and matter have both been the subject of searches [45, 114].

The two categories that make up the majority of HIP searches are the search for magnetic monopoles and the search for Highly Electrically Charged Objects (HECOs). Moreover, massive singly-charged particles traversing matter are highly ionizing at low velocities,  $\beta$  (the particle velocity expressed as a fraction of the speed of light,  $c$ ), according to the Bethe-Bloch formula 1.95. Many of these massive Singly Electrically Charged Object (SECO) HIP scenarios are described in the physics program of the MoEDAL experiment [72]. Additional studies have looked at the sensitivity of MoEDAL to SUSY SECOs [115, 116] and doubly charged SUSY particles [116].

### 3.3.2 Theory

In the framework of quantum physics, Dirac developed a consistent definition of a magnetic monopole in 1931 [1]. A Dirac string, a line of singularity, is associated with this monopole. In order to ensure that this string has no physical impact, Dirac derived his quantization condition known as the Dirac Quantization Condition (DQC) (in SI units of Ampere-metres) given by

$$g = ng_D = \frac{2\pi\hbar}{\mu_0 e} n \quad (3.7)$$

where  $e$  is the electric charge of the particle probe,  $\hbar$  is the reduced Planck's constant,  $g_D$  is the magnetic charge,  $\mu_0$  is the permeability of free space, and  $n$  is an integer. According to the DQC, the electric charge is quantized in units of  $e = \frac{2\pi\hbar}{\mu_0 g_D}$  if magnetic charge exists. The approximate value of  $1g_D$  is  $\sim 68.5e$ . Dirac's theory did not impose any restrictions on the mass or spin of the monopole. Additionally, the DQC indicates a coupling strength much greater than one -

$$\alpha_m = \frac{\mu_0 g_D^2}{4\pi\hbar c} \approx 34 \quad (3.8)$$

As a result, perturbation theory is cannot be used in this case and cross-section calculations based on perturbation theory are only useful as a benchmark. The non-Abelian Georgi-Glashow model's monopole solutions were found in 1974 by 't Hooft [24] and Polyakov [25]. The only gauge symmetry in this model is  $SO(3)$ , which has a three component Higgs field. It was estimated that the mass of the 't Hooft-Polyakov monopole would be around 100GeV. However, experimental evidence has disproved the existence of monopoles with such a low mass.

Then, using the single non-Abelian gauge symmetry,  $SU(5)$ , Georgi and Glashow combined their electroweak theory with a theoretical account of strong nuclear forces to create a Grand Unified Theory (GUT) [20]. The monopoles in this GUT theory,

with a mass of  $\sim 10^{15}\text{GeV}$ , would be far too heavy to be directly produced at any terrestrial collider in the foreseeable future.

The SM has an  $SU(2) \times U(1)$  group structure that forbids the existence of a monopole with finite energy. To allow for the possibility of a "electroweak" monopole [15, 117] with a magnetic charge of  $2g_D$ , Cho and colleagues modified the structure of the SM. Cho, Kim, and Yoon (CKY) have more recently presented an adaptation of the SM that allows for the possibility of a finite energy dyon by including a non-minimal coupling of its Higgs field to the square of its  $U(1)$  gauge coupling strength [16, 118]. A topologically stable, finite energy magnetic monopole with a mass estimated to range from 900GeV to 3TeV exists in another extension of the Standard Model (SM) [19, 21].

Right-handed neutrinos are non-sterile in this extension which has an extended fermion and Higgs sector but keeps the same gauge group as the SM. Ellis, Mavromatos, and You (EMY) considered the issue of whether it is possible to develop generalizations of the CKY model that are consistent with the SM [17]. According to EMY, there is a chance that an electroweak monopole could exist and be found at the LHC if it is consistent with the current constraints on the SM. The search for a monopole has been made as each new energy frontier is explored because the existence of a monopole is such a theoretically sound and revolutionary possibility. Only models that permit a magnetic charge quantized in units of Dirac charge,  $g_D$ , or a multiple of the Dirac charge are taken into consideration in this analysis. In comparison to a relativistic proton, a relativistic monopole with a single Dirac charge will ionize 4700 times more as  $g_D = 68.5e$ . Therefore, it is a great example of a HIP. HECOs, or electrically charged HIPs, have also been theorized, as was already mentioned. Dyons [118], scalars in neutrino-mass models [119], doubly charged massive particles [72], Q-balls [120, 121], aggregates of ud- [122] or s-quark matter [123] and the remnants of microscopic black holes [124] are examples of HECOs. The ATLAS and MoEDAL Collaborations in 8TeV  $p - p$  collisions conducted the first searches for monopoles and/or HECOs at

the LHC [69, 102, 105]. During that time, the MoEDAL search was sensitive to both single and multiply charged monopoles, whereas the ATLAS monopole search was sensitive to singly charged,  $1g_D$ , monopoles.

During Run-2 of the LHC, ATLAS and MoEDAL carried on their searches for HIPs. In the case of monopoles, the ATLAS and MoEDAL searches were complementary in that the ATLAS experiment used the highly ionizing signature of the monopoles to detect the magnetic charge [104–111] while the MoEDAL experiment used the induction technique to search for the magnetic charge directly. There also have been extensive accelerator searches for HIPs at the LHC [102–104, 111]. The most recent LHC discovery was made by the ATLAS experiment using data collected during Run-2 of the LHC with a 13TeV Center-of-Mass (COM) energy [112].

In the following sections, the first application of the prototype MoEDAL Nuclear Track Detector (NTD) System, which uses an ionization signal to detect HIPs, in conjunction with the prototype MoEDAL Trapping Detector System (MMT), which makes use of a Superconducting Quantum Interference Device (SQUID) to detect the presence of trapped magnetic charge is described in detail. Figure 2.2 displays the prototype detector in its entirety. This detector was used to collect and analyze collision data for evidence of HECOs. The collision data totalled  $2.2\text{fb}^{-1}$  at intersection point IP8 on the LHC ring during Run-1. According to estimates, the luminosity measurement's precision at IP8 during Run-1 was 1.16% [125].

A straightforward model for the generation of HIP pairs is the DY mechanism. The Feynman-like diagram depicted in Figure 3.3 is used to compute the cross sections for the production of monopole pairs, Spin-0 HECO pairs, and Spin-1 HECO pairs (top). As shown in the bottom of Figure 3.3, DY production for Spin- $\frac{1}{2}$  HECOs can occur through virtual photon or Z exchange [126].

It is typically assumed that there is no coupling between the magnetic charge and

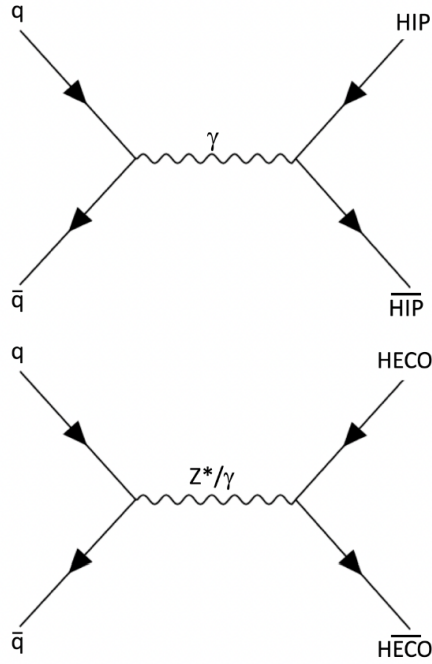


**Figure 3.3:** Tree level Feynman diagram for DY production (top) of HIP/anti-HIP pairs and (bottom) Spin- $\frac{1}{2}$  HECO/anti-HECO pairs.

the  $Z$  boson in the case of Drell-Yan processes that produce magnetic monopoles. This is explicitly demonstrated in some models of these monopoles [19, 21], where any  $Z$ -flux that might be present in the monopole solution would be concentrated inside the monopole core. For electrically charged dyons, this problem depends on the model.

The magnetic moment of the Spin-1 magnetic monopole [127, 128] can be non-zero and is defined by the parameter  $\kappa$  [129]. The value  $\kappa = 1$  is used in this analysis because it is the only one that respects unitarity [130]. It should be noted that these calculations fall under the non-perturbative regime due to the large monopole-photon coupling. To account for potential non-perturbative quantum corrections in the case of HECOs, which are distinguished by large electrical charges, the Drell-Yan (DY) diagram shown in Figure 3.3 should undergo appropriate resummation. These methods are outside the purview of this analysis and thesis and will be the subject of further studies.

### 3.3.3 The MoEDAL Detector

The detector technology employed by MoEDAL is significantly different from that of ATLAS and CMS, the general-purpose LHC experiments. The MoEDAL detector, installed at IP8 alongside the LHCb's VELO (Vertex LOcator) detector, employs two novel passive detection techniques tailored to the search for HIPs. A plastic NTD stack array is the first of these, and it is used to find the ionization trail of HIPs. The second is a detector system made up of absorber elements made of aluminum. Since it is used to trap HIPs with magnetic charge that slow down and stop within its sensitive volume for additional laboratory analysis, this detector system is known as the MMT (Magnetic Monopole Trapper). Since neither of these detector systems needs a trigger nor readout electronics, they are both passive systems. The MoEDAL detector can capture new particles for additional research and keep a permanent record of BSM physics. The NTDs offer a tried-and-true, economical method for precisely measuring the track and the effective charge of a HIP.

It's significant to note that the NTD response was directly calibrated at the CERN SPS using heavy-ion beams. A small but significant portion of the HIPs produced are slowed down, stopped, and trapped by the second detector system, the MMT, for later laboratory research. Such distinct signatures cannot be produced by SM particles. Therefore, a discovery of new physics in MoEDAL would be heralded by the detection of even a few HIP messengers.

### 3.3.4 HIP Energy Loss in MoEDAL

HIPs lose energy in the MoEDAL detector through ionization. Using the Bethe-Bloch formula 1.95, the energy lost through ionization in the MMT detector is calculated. The restricted energy loss (REL) is important information for NTDs [131]. The REL is the total energy lost by the particle in the medium for  $\beta < 10^{-2}$ . REL is the fraction of electronic energy loss that results in the formation of  $\delta$ -rays with energies

lower than a cut-off energy  $T_{cut}$  at higher velocities. The Bethe-Bloch formula, which is limited to energy transfers of  $T < T_{cut}$  with  $T_{cut}$  being a characteristic property of the medium, can be used to calculate the REL.  $T_{cut} \leq 350\text{eV}$  for Makrofol, the MoEDAL NTD used for the analysis detailed in this paper. In Makrofol, the RELs for monopoles and HECOs are depicted in Figures 3.4 and 3.5 respectively.

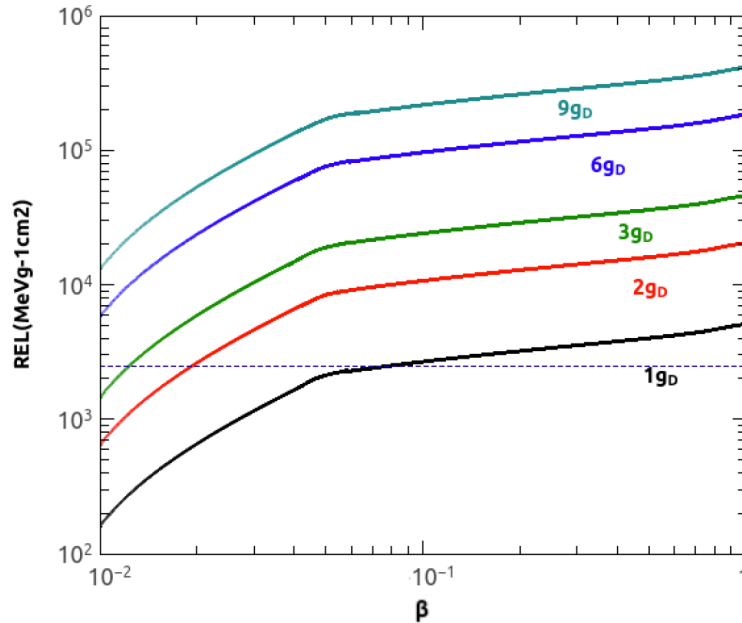


**Figure 3.4:** Restricted Energy Loss in Makrofol for monopoles of different magnetic charge. The horizontal dashed line indicates the Makrofol detection threshold.

### 3.3.5 The MMT Detector

A prototype MMT detector made up of 198 aluminum rods weighing a combined 163kg was used for the LHC's Run-1. As depicted in Figure 2.5, these rods were kept in an enclosure that was positioned directly below the beampipe at the upstream end of the LHCb's VELO detector. The aluminium volumes from the MMT are exposed before being sent to the ETH Zurich Laboratory for Natural Magnetism, where they are put through a SQUID magnetometer to check for the presence of trapped magnetic charge. When a monopole's speed drops below  $\beta \leq 10^{-3}$ , the monopole is assumed to be stopped in the MMT detector.

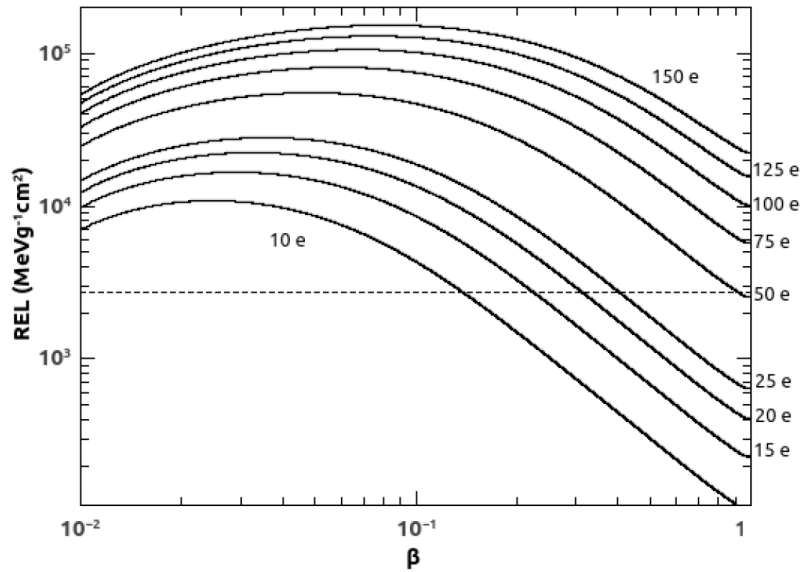


**Figure 3.5:** Restricted Energy Loss in Makrofol for HECOs of different electric charge. The horizontal dashed line indicates the Makrofol detection threshold.

Due to the interaction between the monopole and the nuclear magnetic moment [75, 76, 132], the monopole binds to an aluminium nucleus. The aluminium nucleus' anomalously large magnetic moment results in a monopole-nucleus binding energy of 0.5MeV to 2.5MeV [132], which is comparable to the shell model splittings. In any case, it is logical to assume that the monopole's extremely strong magnetic field will rearrange the nucleus and enable it to bind strongly to it. According to Ref. [132], monopoles bound in this way would be trapped forever. For the trapped monopole state's lifetime to interfere with MoEDAL's ability to detect it, fields well in excess of several Tesla would be necessary. We point out that only fields less than  $\sim 10mT$  are subject to the MoEDAL detector.

### 3.3.6 Calibration of the MMT detector

A persistent current in the SQUID coil encircling the samples' transport axis that travels through the SQUID magnetometer is how a magnetic monopole captured in a MMT volume is identified and measured.

There are two separate methods used to calibrate the magnetometer response. Briefly

stated, the magnetometer calibration was obtained by applying the convolution method to a dipole sample, and it was then verified using long, thin solenoids that simulated a monopole of a well-known magnetic charge. The calibration techniques are described in detail in 3.1 and [79].

These calibration techniques agree to within 10%, which is considered to be the calibration uncertainty for pole strength. Measurements have shown that the magnetometer response is linear and charge-symmetric over the magnetic charge range of  $0.3g_D$ – $300g_D$ .

### 3.3.7 The Nuclear Track Detector System

In the VELO cavern, the MoEDAL NTD is organized into modules and deployed around IP8. For Run-1, a prototype NTD array of  $125 \times 25\text{cm} \times 25\text{cm}$  stacks was installed, as depicted in Figure 2.2. Each module is made up of three layers of 1.5mm thick CR39 polymer, three layers of Makrofol, and three layers of Lexan, each measuring 0.5mm and 0.25mm thick and kept inside Aluminum bags as shown in Figure 2.4. The Lexan foils are not currently being studied; instead, they act as protective layers.

Only the Makrofol NTDs are utilized in this analysis. This is because Makrofol has a rough ten-fold higher detection threshold than CR39, which leads to significantly less "visual noise" in the etched plastic as a result of spallation products originating from beam backgrounds. The interaction of the LHC beam with the LHC machine components and the machine environment produces beam background particles. As a result, the analysis of the CR39 NTDs takes a lot longer. It is not necessary to scan the CR39 in the first pass because HIPs produced by the DY mechanism in LHC collisions during Run-1 are sufficiently highly ionizing to be easily detected using the Makrofol NTDs. All 6 NTD sheets in the stack would have been examined in the event that a candidate event was observed in the Makrofol.

### 3.3.8 The Etching Procedure

In plastic track-etch detectors, the passage of a HIP can result in permanent polymeric bond damage in a cylindrical region (the "latent track") that extends a few tens of nanometers around the particle trajectory shown in Figure 3.6. The latent track is "amplified" and can be seen under an optical microscope thanks to a subsequent chemical etching.

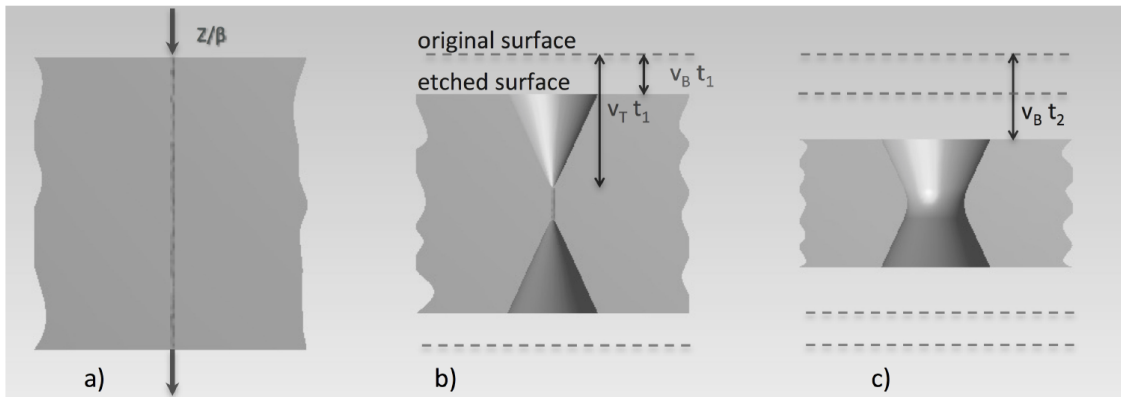


**Figure 3.6:** Illustration of the track-etch technique: a) latent track forming along the trajectory of a high ionizing particle impinging perpendicularly on the NTD surface ; b) development of conical pits during the etching process; c) etch-pits joining after a prolonged etching, forming a hole in the detector.

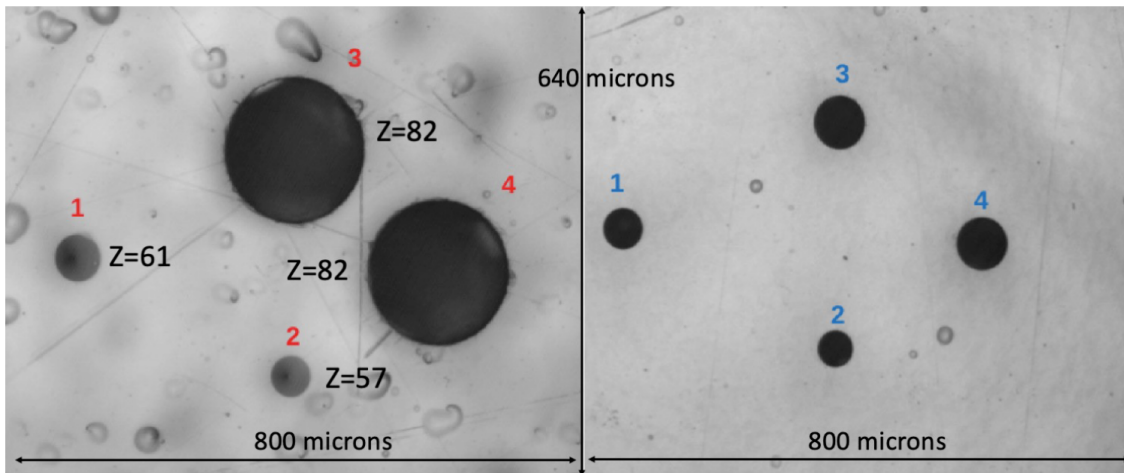
The bulk of the material is etched away during the etching process at a rate of  $v_B$  and at a faster rate of  $v_T$  along the latent track. Under an optical microscope, the damage zone appears as two cone-shaped etch-pits, one on each face of the NTD sheet. For normally incident particles, etch-pit surface openings are circular; otherwise, they are elliptical. A "track" candidate is a single well-measured etch pit. We have a confirmed track candidate if another etch pit is measured on the NTD sheet and is consistent with being the twin.

Figure 3.6 depicts a schematic of an etch-pit at various etching times for a normally incident particle crossing the detector with a constant energy loss. There were two etching conditions used shown in Table 3.1. The first is what is referred to as a "strong" etching condition, which allows for faster etching and produces larger etch-pits that are simpler to see with visual scanning. The first, most upstream Makrofol

foil in each module received a thorough etching. The second condition, known as "soft etching," causes a slower etching process. As a result, the etching procedure can be carried out in stages to mimic the formation of etch-pits. If a candidate track is found in the first layer, soft etching is used on the subsequent Makrofol foils in the stack. Microphotographs of relativistic  $\text{Pb}^{82+}$  tracks in Makrofol foils etched under "strong conditions" and "soft conditions" are shown in Figure 3.7 on the right and left respectively.

**Table 3.1:** Etching Conditions of Makrofol

Etching Mode	Etchant	$v_B$ ( $\mu\text{m}/\text{hour}$ )
Strong	6N KOH + 20% ethyl alcohol at 65°C	$23 \pm 0.5$
Soft	6N KOH + 20% ethyl alcohol at 50°C	$3.4 \pm 0.05$



**Figure 3.7:** Microphotographs of relativistic  $\text{Pb}^{82+}$  tracks and of nuclear fragments ( $Z < 82$ ) in two consecutive foils of Makrofol. Each image frame measures  $0.64\text{mm} \times 0.80\text{mm}$ . Etch-pits are from the same ions crossing the detector foils: (left) Makrofol foil etched in "strong conditions"; (right) Makrofol foil etched in "soft conditions". Note that the microphotographs also show two clearly differentiated fragmentation products of Pb: La ( $Z = 57$ ); and, Pm ( $Z = 61$ ).

### 3.3.9 Calibration of the NTD Detector

The etching rate ratio, also known as the reduced etch rate,  $p = \frac{v_T}{v_B}$ , as a function of the particle's REL, is used to assess the response of the NTD. According to reference [4], heavy ion beams are used to assess the detector response across a wide range of energy losses. At CERN's SPS, the Makrofol was calibrated using ion beams with energies of 158A GeV  $\text{Pb}^{82+}$  and 13A GeV  $\text{Xe}^{54+}$ . A stack of Makrofol foils was

placed upstream and downstream of an Aluminum target as part of the calibration set-up.

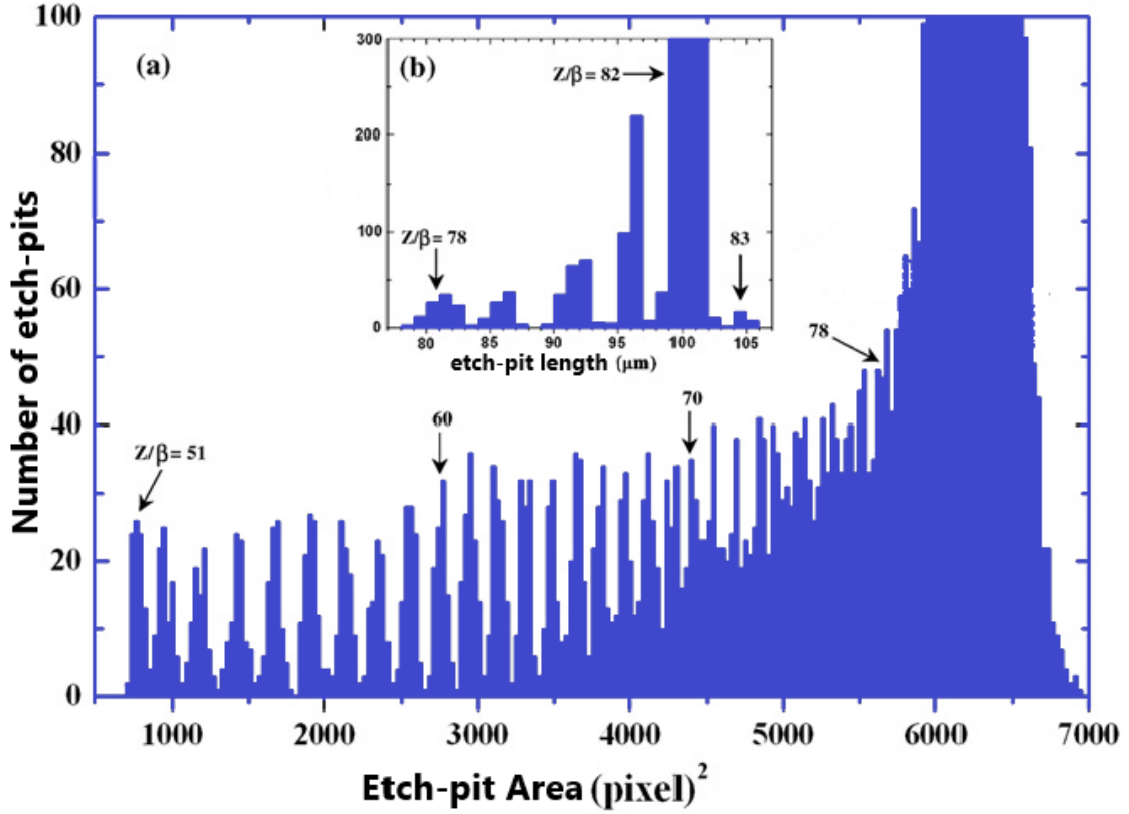
Along their path through the detector foils and the target, incoming ions undergo nuclear fragmentation that change their charge. The detectors were etched in 6N KOH+20% ethyl alcohol at 50°C for 10 hours following exposure. The bulk etching velocity was  $v_B = 3.4 \frac{\mu\text{m}}{\text{h}}$ . Following etching, an automatic scanning system that provided the cone base area and the coordinates of the etch pits' center was used to measure the size of the etch pits. Etch pit diameters typically range from  $10\mu\text{m} - 100\mu\text{m}$ , with a modal value between  $30\mu\text{m} - 40\mu\text{m}$ .

Figure 3.8 shows the base area distributions of the incoming ions and their fragments. The projectile fragments move in roughly the same direction and at a similar speed as the incident ions. The charge corresponding to each nuclear fragment peak can be found in the base area spectrum, and the corresponding REL can be calculated. Ref. [4] provides a thorough explanation of the calibration process. Reduced etch rate,  $p$ , REL, and  $\frac{Z}{\beta}$  are computed for each identified peak. The obtained calibration data is displayed in Figure 3.9.

The minimum detectable relativistic charge for Makrofol is  $\frac{Z}{\beta} \sim 50$ , for both soft and strong etching. The REL that corresponds to this detector threshold is  $\sim 2700\text{MeVg}^{-1}\text{cm}^2$ .

### 3.3.10 Etching and Scanning of MoEDAL NTD

The MoEDAL NTD stacks were transported to the INFN etching and scanning laboratory in Bologna after exposure in the LHC IP8 region. On each detector module, three 2mm diameter reference holes are drilled in order to establish a global module reference system. When determining the position of a particle track over the detector surface, this coordinate system offers an accuracy of  $100\mu\text{m}$ . The stacks are then



**Figure 3.8:** Distribution of track surface areas in Makrofol exposed to 158A GeV Pb<sup>82+</sup> and etched in soft conditions [4].

unpacked, the detector foils are labeled, and a grid of points evenly spaced across the foil surface is used to measure the thickness of the foils. Only Makrofol was used for the search described in this paper.

The Makrofol layer furthest upstream in each exposed stack was etched in 6 N KOH + 20% ethyl alcohol at 65°C. Etch-pits as small as 10 μm would be visible under 20 times magnification after 6 hours of etching. By scanning foils that had been exposed to ions as described below, an efficiency of 99% was calculated. Manual scanning was used to examine each layer of Makrofol. Every surface structure that was discovered was examined at a higher magnification and categorized as either a particle's track or a material defect.

If two etch-pits are found on the foil's front and back, they were seen under higher magnification (100 × –500×). The angle of incidence on each surface is estimated

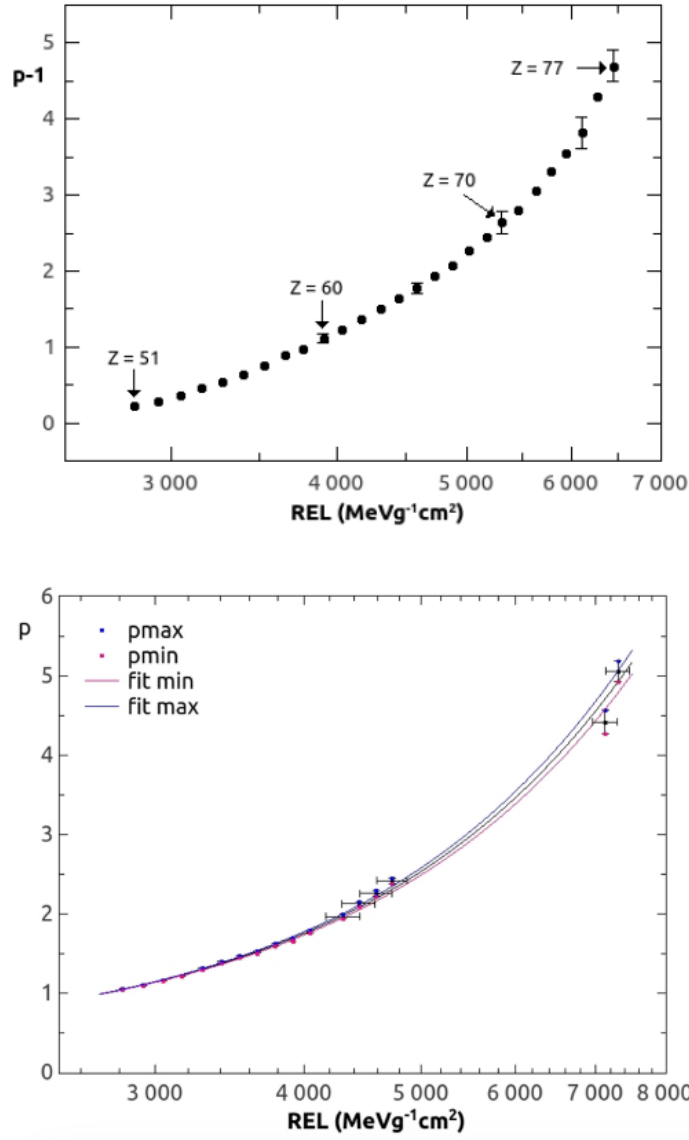


**Figure 3.9:** Reduced etch-rate ( $p$ ) versus REL for Makrofol exposed to relativistic Lead and Xenon ion beams: (top) detectors etched in soft conditions; (bottom) detectors etched in strong conditions. The upper and low curves are drawn through the  $\pm 1\sigma$  value of the error on each  $p$  value, where the error bars represent a convolution of the statistical and systematic errors on each point.

from the size of the etch-pits on the "front" and "back" surfaces and the bulk etching rate. One side of a Makrofol layer can be scanned in its entirety using the microscope at a magnification of  $32\times$  in about 2.5 hours.

A potential candidate "track" is described as a pair of collinear incident and exiting etch-pits that are consistent with pointing to the IP. In particular, the downstream Makrofol foils would be etched in 6 N KOH + 20% ethyl alcohol at  $50^\circ\text{C}$  if a candidate is discovered in the first layer of a module. When the NTD sheet is etched, the

vast majority of spallation products resulting from beam backgrounds only produce a single pit. Their range in the NTD sheet is typically tens of microns.

The next step would be to use an optical microscope with higher magnification ( $100\times$ – $200\times$ ) to accurately scan the downstream Makrofol sheets in a square region of about  $1\text{cm}^2$  around the candidate's anticipated position. The CR39 would then be scanned for etch-pits that are concentric with those in the Makrofol layers if concentric etch-pits are discovered in all three Makrofol sheets. All six NTD sheets in the stack pointing to the IP must have collinear etch-pits in order for a HIP candidate track to exist. Furthermore, the REL calculated from the dimensions of the etch-pits (surface area, etch-pit length) must agree with the HIP hypothesis. However, no candidate track was discovered.

### 3.3.11 The Makrofol Detection Threshold

The REL of the HIP must be higher than the detection threshold of Makrofol in order for it to be detected. The etching conditions will affect the detection threshold. Additionally, it will change depending on the HIP's angle of incidence,  $\delta$  on the NTD. The relationship between the threshold and the maximum angle of incidence,  $\delta_{max}$  that the HIP can make to the normal of the NTD and still be detected is given by:

$$p = \frac{1}{\cos(\delta)} \quad (3.9)$$

where  $p$  is the reduced etch-rate mentioned above. The lowest threshold is obtained when a HIP impinges on the NTD normally. Figure 3.10 depicts the curve derived from an empirically based parameterization of the relationship between  $\delta_{max}$  and the REL. The acceptance for HIPs incident on the NTD stacks of the MoEDAL is determined using this parameterization.

For the HIP to be detected its REL must be greater than the detection threshold

of the Makrofol. The detection threshold will vary with the etching conditions. It will also vary with the angle of incidence of the HIP ( $\delta$ ) on the NTD. The connection between the threshold and the maximum angle of incidence ( $\delta_{max}$ ) to the normal to the NTD that the HIP can make and still be detected, is expressed by the relationship:  $p = \frac{1}{\cos(\delta_{max})}$ , where  $p$  is reduced etch-rate. Everything else being equal, the greater the maximum angle of incidence the lower the detection threshold. The lowest threshold is obtained for a HIP impinging normally to the NTD. The curve showing the relation between  $\delta_{max}$  and the REL is shown in Figure 3.10.

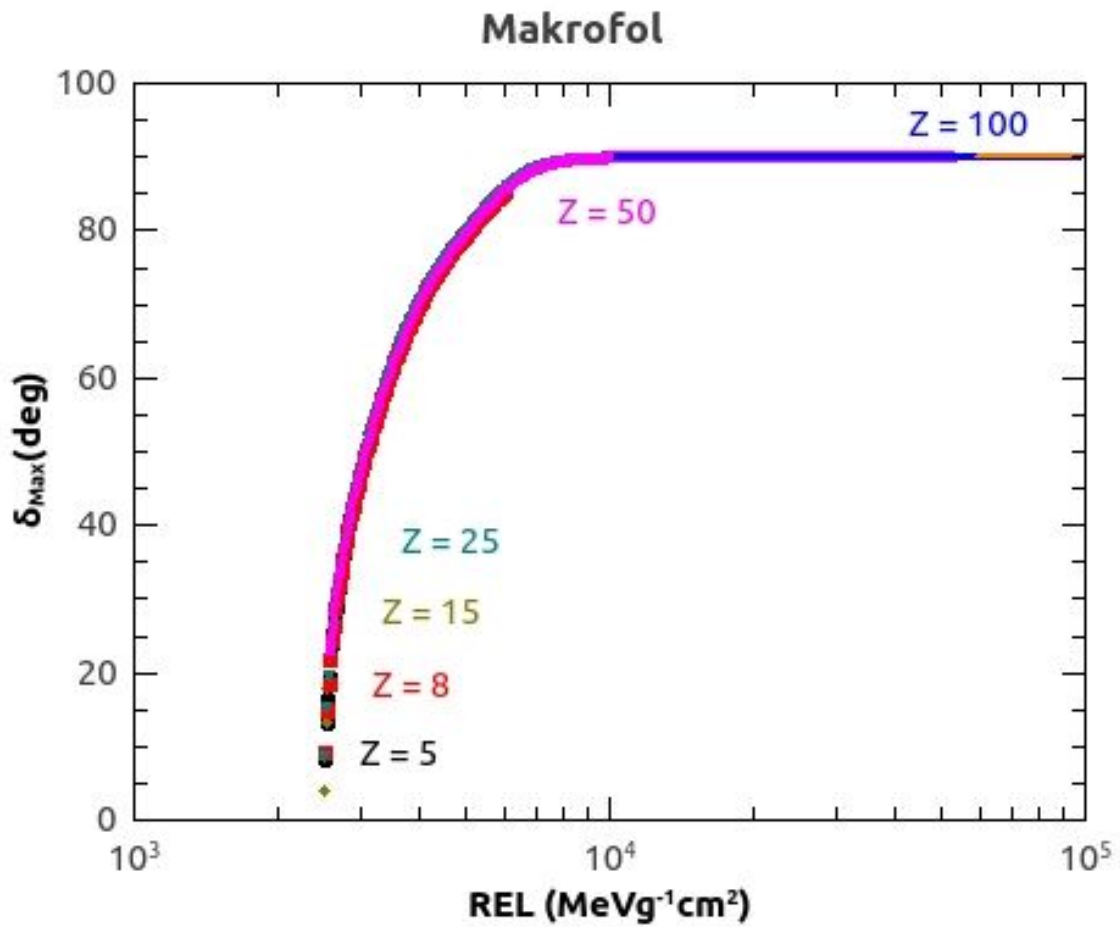


Figure 3.10: The maximum angle to the normal of the NTD plane within which the HIP will be detected.

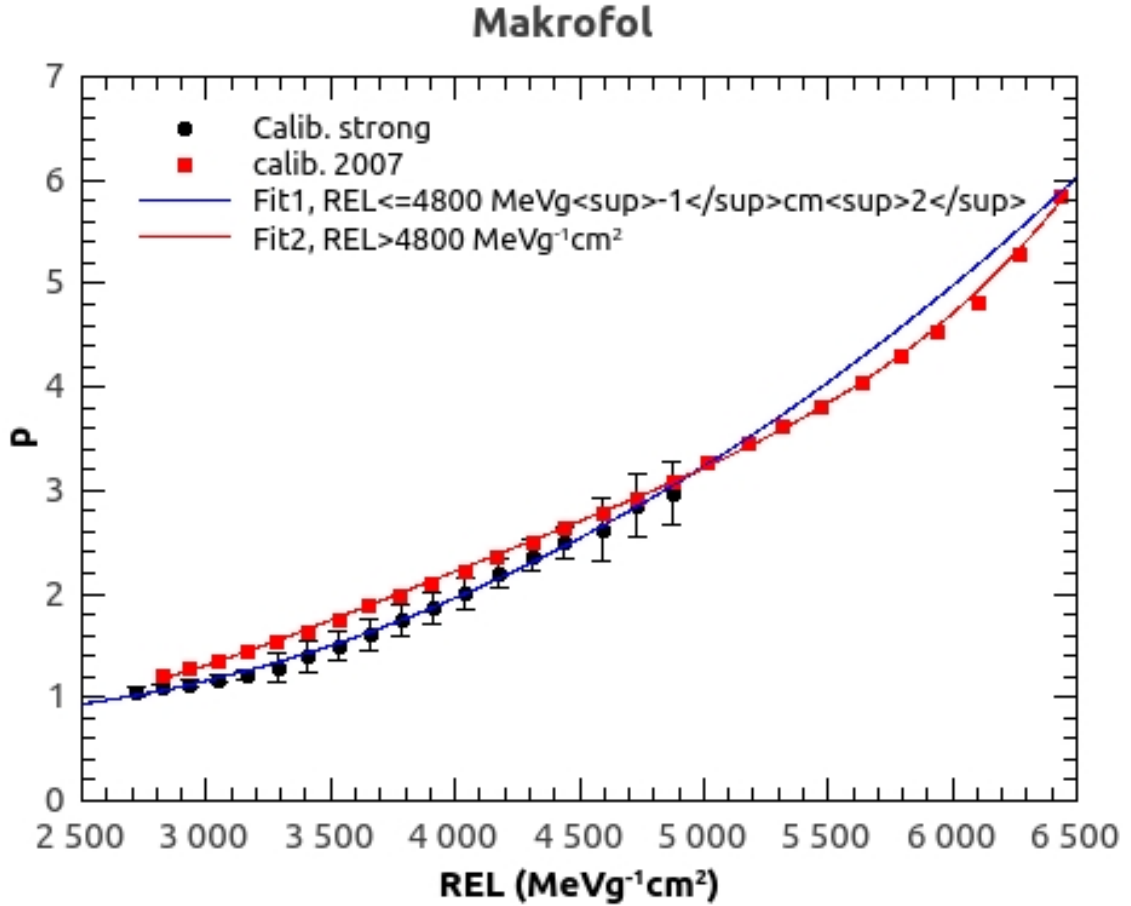


Figure 3.11: Calibration Curve for  $p$  vs REL similar to the bottom of Figure 3.9

We then parameterize the  $p$  vs REL curve shown in Figure 3.11 with a second order polynomial.  $p = p_0 + p_1x + p_2x^2$  where  $p_0 = -0.215 \pm 0.534$ ;  $p_1 = 0.0002849 \pm 0.0002754$ ;  $p_2 = 6.071 \times 10^{-8} \pm 3.362 \times 10^{-8}$  and  $x = \text{REL}$ . This parameterization is excellent with  $R^2 \approx 0.99$ . Note that REL is in units of  $\text{MeVg}^{-1}\text{cm}^2$ . The value of  $p$  is computed using the REL value. Then,  $\delta_{max}$  is computed using  $\delta_{max} = \arccos\left(\frac{1}{p}\right)$ . The actual angle  $\alpha$ , formed when the HIP impinges on the NTD, is determined via analysis. If  $\alpha < \delta_{max}$ , we accept the HIP.

### 3.3.12 Efficiency and False Positives in the NTD Detectors

As previously mentioned, a string of etch-pits in the stack, where each etch-pit pair is caused by the ingress and egress of the HIP passing through an NTD sheet, would serve as the signal for the passage of a HIP messenger of new physics through a

MoEDAL NTD stack. In this search or any other HIP search using NTDs, no such signal has ever been discovered [101]. In fact, only the most upstream sheet of the 125 NTD stacks, corresponding to  $7.8\text{m}^2$ , were examined, revealing no candidates.

The astroparticle physics experiments MACRO [35] and SLIM [36], which deployed a surface area of  $1263\text{m}^2$  and  $427\text{m}^2$  respectively, also had the absence of false positives using the NTD technique. Both experiments failed to find any HIP candidates. It should be noted that these experiments use an NTD technique that is nearly identical to that used at colliders. The lack of false positives in astroparticle physics experiments or colliders using the NTD technique begs the question of false negatives or detector efficiency, where a signal is present but not detected.

The heavy ion beams that are used to calibrate NTD detectors can be used to evaluate this. The detection, or scanning, efficiency for the etch-pits caused by heavy-ion HIPs with ionizing power above the NTD threshold was measured to be greater than 99% in the absence of beam backgrounds, as detailed below. NTD calibration stacks were exposed to a relativistic lead-ion beam as described above to estimate the detection efficiency of NTDs for HIPs in the presence of beam backgrounds. The stacks included Makrofol NTD sheets that had been exposed to the beam backgrounds (LHC-exposed sheets) during data collection for a year in the VELO chamber of the LHC, interspersed with sheets that had not been exposed to the beam backgrounds (LHC-unexposed sheets). The plastic used for calibration and standard data collection came from the same production batch. The NTD sheets that made up the calibration stacks were then etched in the same manner as the standard NTD stacks used during Run-1 to collect data. The same manually controlled optical scanning microscope technology used to inspect all MoEDAL NTD stacks was used to scan the individual sheets.

The signal etch-pits seen in the LHC unexposed sheets, where the signal can be clearly seen with a 100% efficiency, can serve as a map because the relativistic lead-

ion calibration beam particles penetrate the entire stack. By performing independent comparison scans of the other LHC-unexposed sheets in the stack, which naturally have the same etch-pit number and pattern, the identification of etch-pits in the LHC-unexposed sheets is evaluated to be 100%. The scanning efficiency for LHC-exposed sheets can be determined by using the LHC-unexposed sheets in the stack as a one-to-one same-scale map for the hits in the adjacent LHC- exposed sheets.

According to these measurements, the overall scanning efficiency for detection above threshold was greater than 99%. By scanning the LHC-exposed sheets and comparing the etch pits discovered with the etch pits identified in the nearby LHC- unexposed stacks, this number was discovered. Due to the calibration beam passing through the entire stack, each sheet has precisely the same number and pattern of "signal" etch-pits.

### 3.3.13 Acceptance of the LHC Run-1 MoEDAL Detector

The percentage of events in which at least one HIP of the DY produced pair was found in MoEDAL in either the NTD detector or the MMT detector is known as the acceptance of the MoEDAL detector. The interplay of the geometrical placement of MoEDAL NTD modules and MMT detectors, energy loss in the detectors, mass of the particle, and spin-dependent kinematics of the interaction products is used to describe the acceptance for DY production of HECOs and magnetic monopoles.

The only method of detection for the HECOs is the NTD system of MoEDAL. The pair-production model establishes the kinematics and overall trapping acceptance for a given HIP spin and mass. Uncertainties in the material description account for the majority of the uncertainty in acceptance [105–107]. By running simulations with hypothetical material conservatively added and removed from the nominal geometry model, this contribution is estimated. Figure 3.12 provides an illustration of the MoEDAL NTD acceptance curves for Spin- $\frac{1}{2}$ , Spin-0, and Spin-1 HECOs with

charge  $125e$  produced by a DY process using virtual photon exchange. The rest of the acceptance curves are shown in the Appendix 5.1.1 in Figures 5.1 and 5.2.

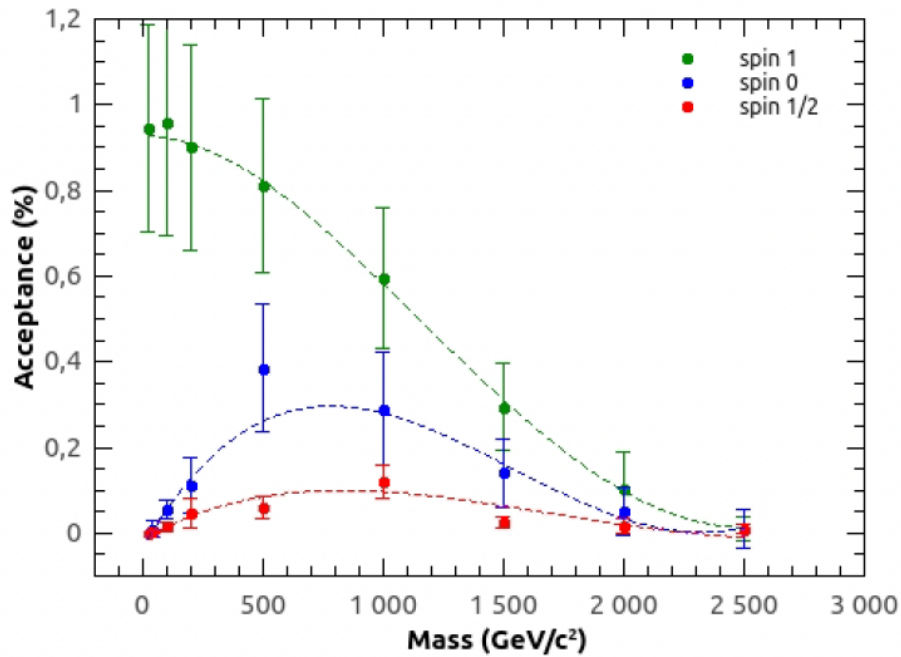


Figure 3.12: Acceptance for Spin-0, Spin- $\frac{1}{2}$  and Spin-1 HECOs with charge  $125e$ .

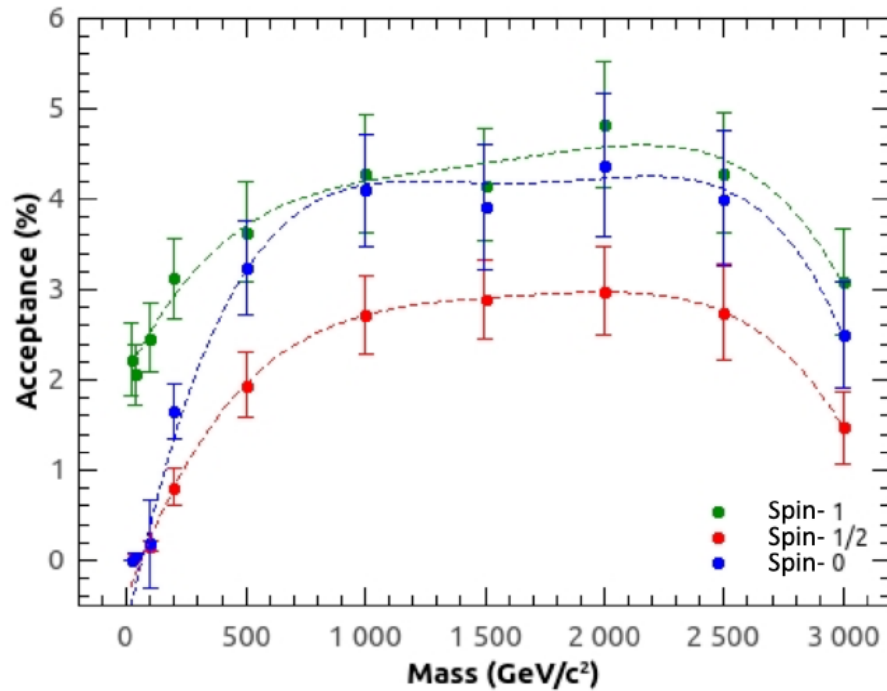
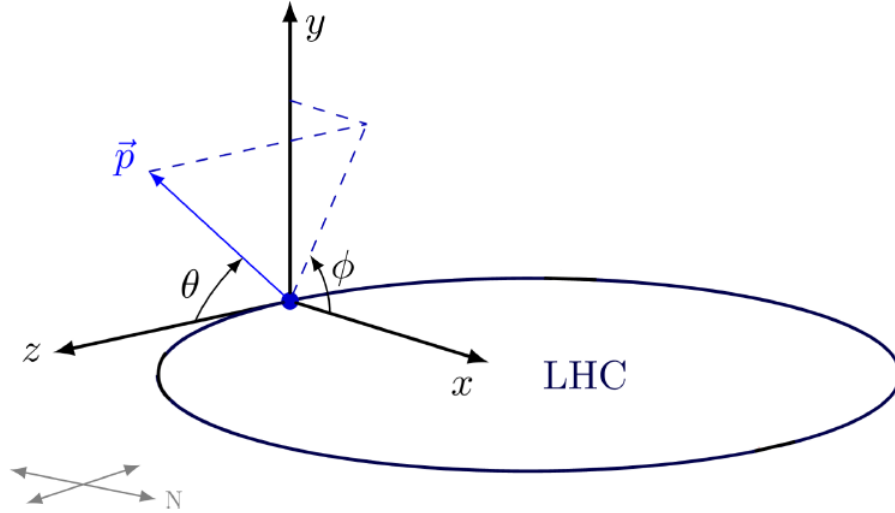


Figure 3.13: Acceptance for Spin-0, Spin- $\frac{1}{2}$  and Spin-1 Monopole Pair Production with Magnetic Charge  $2g_D$ .

It should be noted that HECOs trapped in the MMT detector lack a magnetic charge and cannot be detected by MoEDAL's SQUID detector. This means that HECOs can only be detected by the NTDs. The distribution of the MoEDAL NTD detectors and the kinematics of the produced particles convoluted with the VELO material immediately surrounding IP8 determine these curves. Only a partial, non-uniform coverage of the solid angle is provided by the prototype MoEDAL detector. This changes when we consider the LHC Run-2 MoEDAL detector.

Figure 3.13 displays the acceptance curves for Spin-0, Spin- $\frac{1}{2}$  and Spin-1 monopoles discovered by combining the NTD and MMT detectors. The rest of the acceptance curves are shown in the Appendix 5.1.2 in Figure 5.3. The prototype detector used for LHC Run-1 is the subject of the acceptances depicted in Figures 3.12 and 3.13. The Full Run-2 detector has a slightly higher acceptance rate.

The degree to which the detector elements' arrangement in theta ( $\theta$ ) corresponds to the corresponding theta distribution of the DY-produced HECOs is the primary cause of the difference between the acceptances for Spin-0, Spin- $\frac{1}{2}$  and Spin-1 HECOs. We have compared the kinematic quantities of the uncut signal -momentum ( $p$ ), theta ( $\theta$ ) and phi ( $\phi$ ) - to the corresponding distributions for the events that meet the selection criteria to demonstrate this point. Figure 3.14 defines the theta ( $\theta$ ) and phi ( $\phi$ ) angles.



**Figure 3.14:** The coordinate system used in the analysis

Given the significant difference between the number of generated and selected events, each plot was normalized to the highest amplitude bins as determined by the Freedman-Diaconis rule [133] in order to make the comparison more understandable. Figures 3.15, 3.16 and 3.17 show the kinematic variables we plotted for the DY production for Spin-0, Spin- $\frac{1}{2}$  and Spin-1 HECOs with a mass of 100GeV and an electric charge of 50e respectively. Figure 3.18 displays the corresponding plots for DY production via photon/ $Z^0$  exchange, which only affects the Spin- $\frac{1}{2}$  case. Similarly, Figures 3.19, 3.20 and 3.21 show the kinematic variables we plotted for the DY production for Spin-0, Spin- $\frac{1}{2}$  and Spin-1 monopoles with a mass of 1000GeV and an electric charge of  $1g_D$  respectively for the NTD detector. Since we are able to detect monopoles using the MMT detector as well, Figures 3.22, 3.23 and 3.24 show the kinematic variables we plotted for the DY production for Spin-0, Spin- $\frac{1}{2}$  and Spin-1 monopoles with a mass of 1000GeV and an electric charge of  $1g_D$  respectively for the MMT detector.

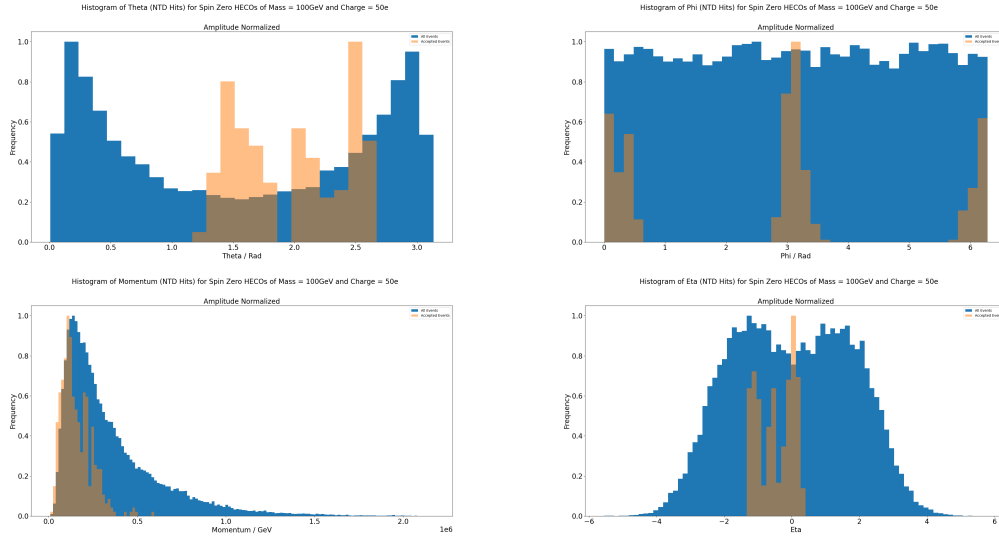


**Figure 3.15:** The  $\theta$ ,  $\phi$ , momentum and  $\eta$  distributions for Spin-0 HECOs of mass 100GeV and electric charge 50e, produced via the DY process via virtual photon exchange. In each case, 60K events were originally generated. The plots are normalized to the maximum amplitude. The blue histogram represents generated events and the underlying orange histogram shows the distribution of selected events.

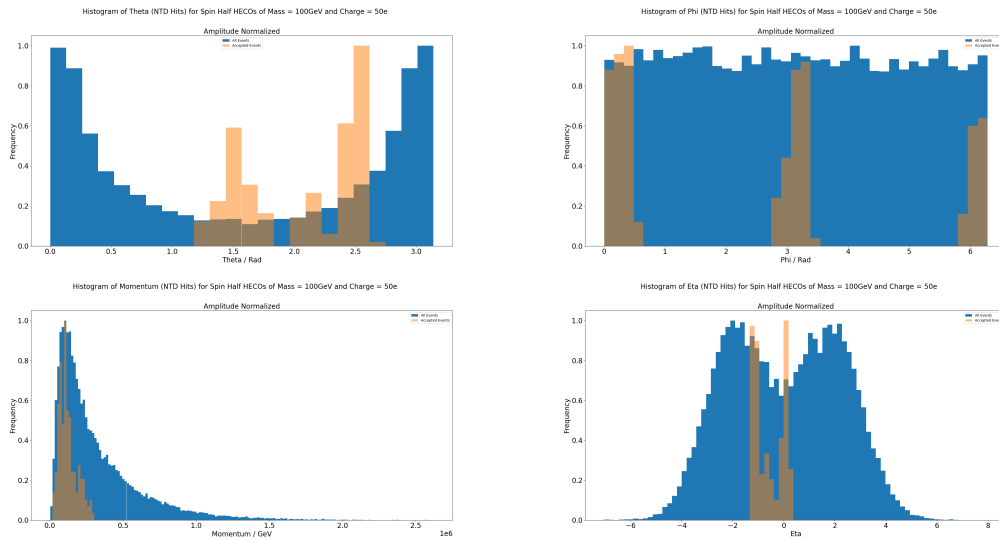


**Figure 3.16:** The  $\theta$ ,  $\phi$ , momentum and  $\eta$  distributions for Spin- $\frac{1}{2}$  HECOs of mass 100GeV and electric charge 50e, produced via the DY process via virtual photon exchange. In each case, 60K events were originally generated. The plots are normalized to the maximum amplitude. The blue histogram represents generated events and the underlying orange histogram shows the distribution of selected events.

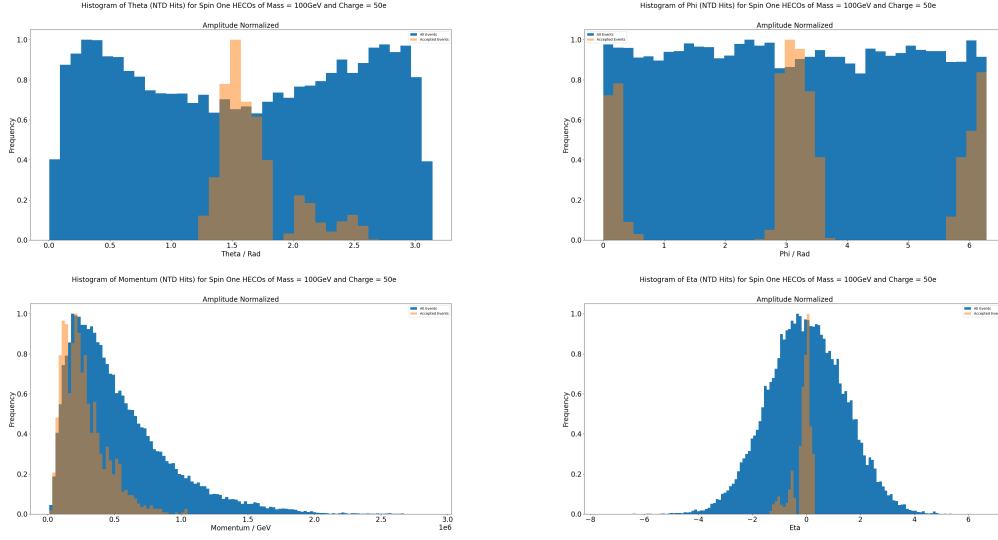


**Figure 3.17:** The  $\theta$ ,  $\phi$ , momentum and  $\eta$  distributions for Spin-1 HECOs of mass 100GeV and electric charge 50e, produced via the DY process via virtual photon exchange. In each case, 60K events were originally generated. The plots are normalized to the maximum amplitude. The blue histogram represents generated events and the underlying orange histogram shows the distribution of selected events.

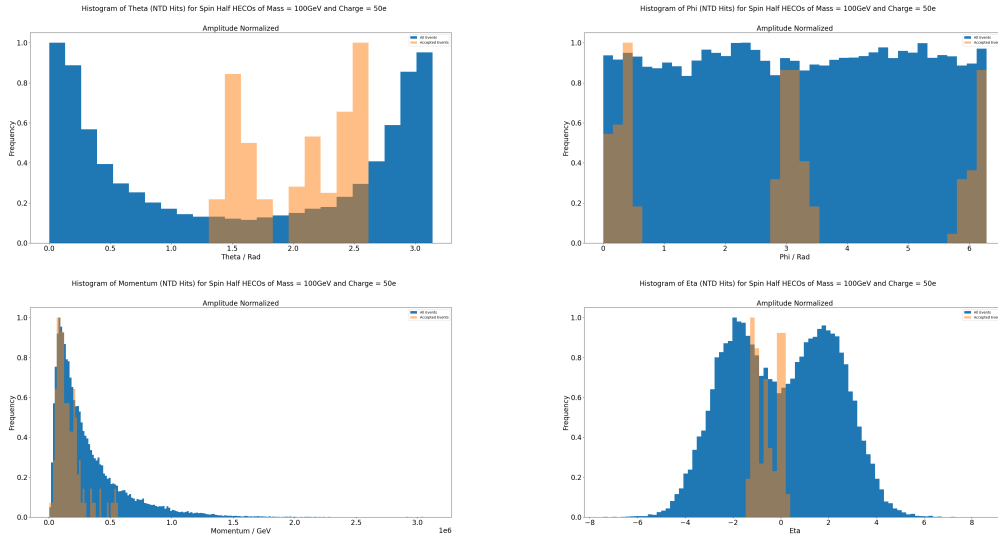


**Figure 3.18:** The  $\theta$ ,  $\phi$ , momentum and  $\eta$  distributions for Spin- $\frac{1}{2}$  HECOs of mass 100GeV and electric charge 50e, produced via the DY process via virtual photon and  $Z^0$  exchange. In each case, 60K events were originally generated. The plots are normalized to the maximum amplitude. The blue histogram represents generated events and the underlying orange histogram shows the distribution of selected events.

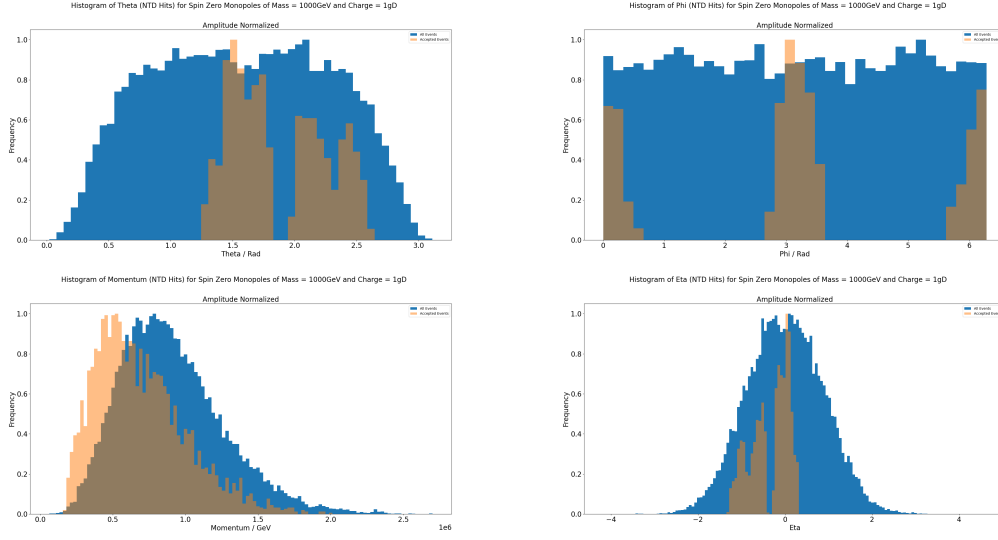


**Figure 3.19:** The  $\theta$ ,  $\phi$ , momentum and  $\eta$  distributions for Spin-0 monopoles of mass 1000GeV and electric charge  $1g_D$ , produced via the DY process via virtual photon exchange for the NTD detector. In each case, 60K events were originally generated. The plots are normalized to the maximum amplitude. The blue histogram represents generated events and the underlying orange histogram shows the distribution of selected events.

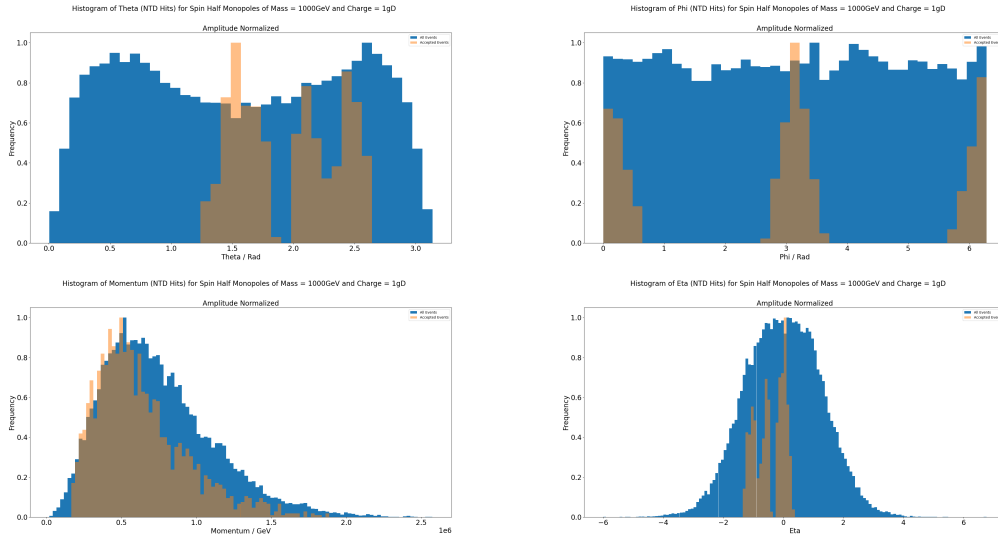


**Figure 3.20:** The  $\theta$ ,  $\phi$ , momentum and  $\eta$  distributions for Spin- $\frac{1}{2}$  monopoles of mass 1000GeV and electric charge  $1g_D$ , produced via the DY process via virtual photon exchange for the NTD detector. In each case, 60K events were originally generated. The plots are normalized to the maximum amplitude. The blue histogram represents generated events and the underlying orange histogram shows the distribution of selected events.

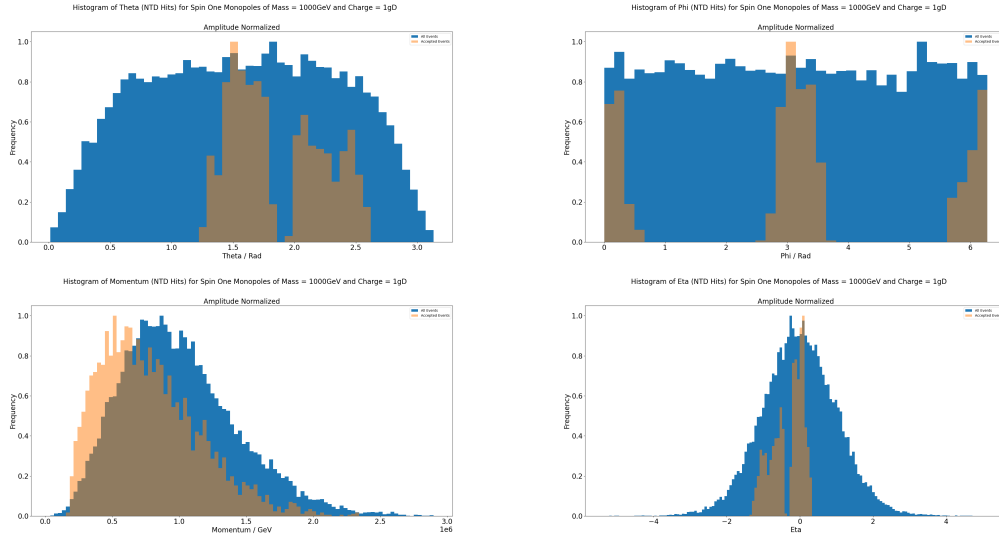


**Figure 3.21:** The  $\theta$ ,  $\phi$ , momentum and  $\eta$  distributions for Spin-1 monopoles of mass 1000GeV and electric charge  $1g_D$ , produced via the DY process via virtual photon exchange for the NTD detector. In each case, 60K events were originally generated. The plots are normalized to the maximum amplitude. The blue histogram represents generated events and the underlying orange histogram shows the distribution of selected events.

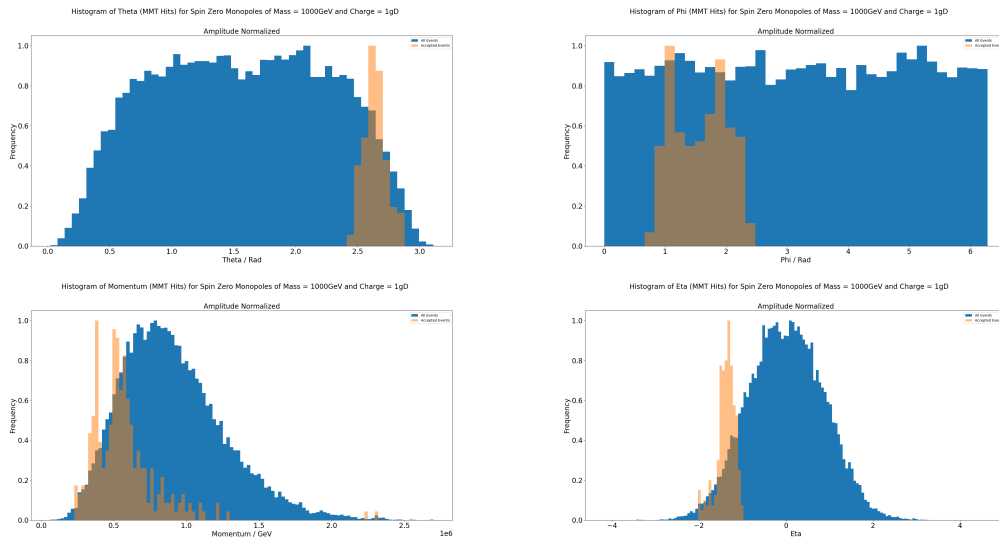


**Figure 3.22:** The  $\theta$ ,  $\phi$ , momentum and  $\eta$  distributions for Spin-0 monopoles of mass 1000GeV and electric charge  $1g_D$ , produced via the DY process via virtual photon exchange for the MMT detector. In each case, 60K events were originally generated. The plots are normalized to the maximum amplitude. The blue histogram represents generated events and the underlying orange histogram shows the distribution of selected events.

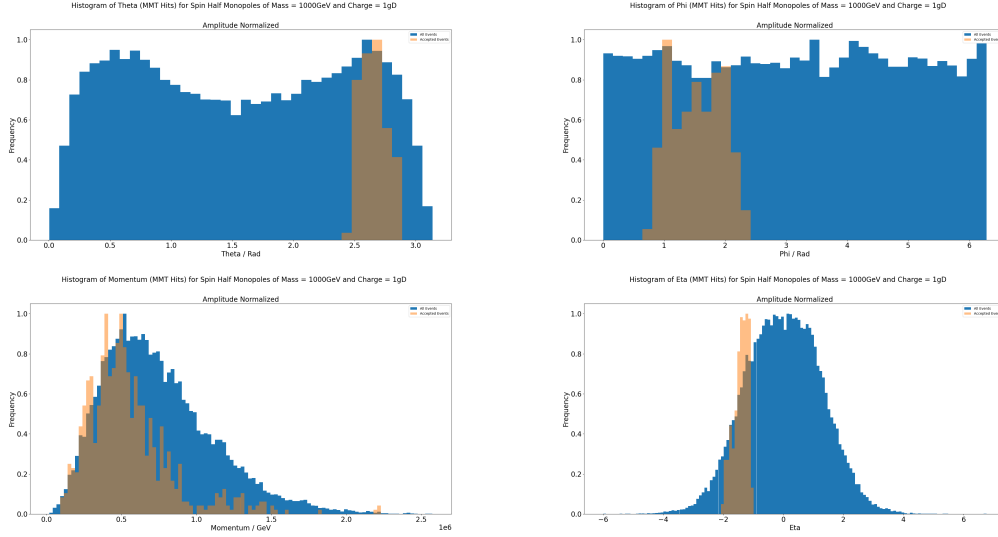


**Figure 3.23:** The  $\theta$ ,  $\phi$ , momentum and  $\eta$  distributions for Spin- $\frac{1}{2}$  monopoles of mass 1000GeV and electric charge  $1g_D$ , produced via the DY process via virtual photon exchange for the MMT detector. In each case, 60K events were originally generated. The plots are normalized to the maximum amplitude. The blue histogram represents generated events and the underlying orange histogram shows the distribution of selected events.

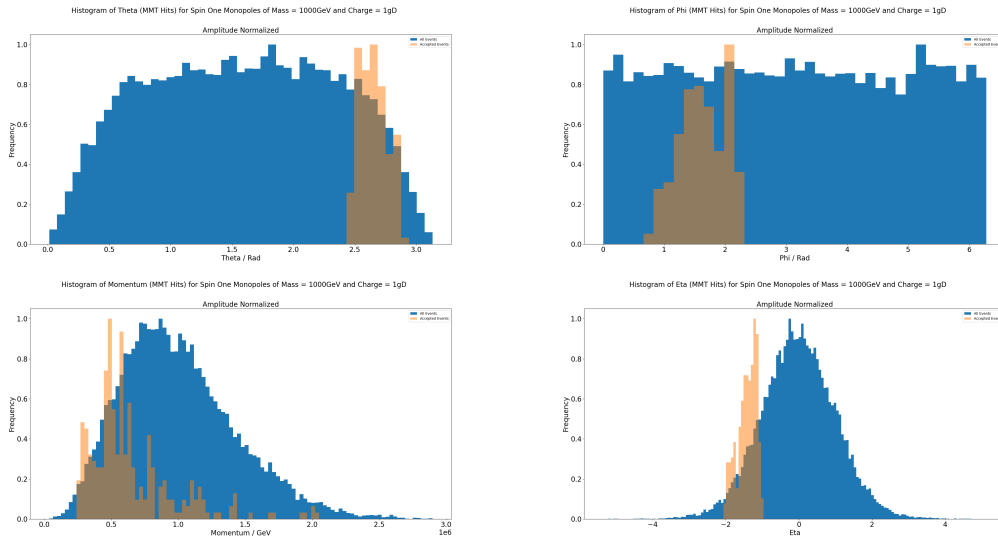


**Figure 3.24:** The  $\theta$ ,  $\phi$ , momentum and  $\eta$  distributions for Spin-1 monopoles of mass 1000GeV and electric charge  $1g_D$ , produced via the DY process via virtual photon exchange for the MMT detector. In each case, 60K events were originally generated. The plots are normalized to the maximum amplitude. The blue histogram represents generated events and the underlying orange histogram shows the distribution of selected events.

### 3.3.14 Analysis Results

MadGraph5 was used to generate events for monopole production via the Drell-Yan mechanism. Spin-0 HIPs, Spin- $\frac{1}{2}$  HIPs and Spin-1 HIPs were considered for 10 mass points of 20GeV, 40GeV, 100GeV, 200GeV, 500GeV, 1000GeV, 1500GeV, 2000GeV,

2500GeV and 3000GeV for events at a centre of mass (COM) energy of  $\sqrt{s} = 8\text{TeV}$ . Furthermore, events containing Spin- $\frac{1}{2}$  HECOs produced by the DY mechanism mediated by the  $Z^0$  boson were generated as well.

As was mentioned, MadGraph5 is a next to leading order Monte-Carlo (MC) generator. It is a framework that aims at providing all the elements necessary for SM (Standard Model) and BSM (Beyond Standard Model) phenomenology, such as the computations of cross sections, the generation of hard events and their matching with event generators, and the use of a variety of tools relevant to event manipulation and analysis. Processes can be simulated to LO (leading order) accuracy for any user-defined Lagrangian, and the NLO (next to leading order) accuracy in the case of QCD (Quantum Chromodynamics) corrections to SM processes. Matrix elements at the tree and one-loop-level can also be obtained.

For the DY (Drell-Yan) case, the proton beam option was selected. Furthermore, the energy of each beam was set to 4000GeV giving rise to a total COM (centre of mass) energy of 8TeV. After the MC simulation, the output files were analysed using ROOT (an analysis software based on python and C++ for CERN use) and passed through GAUSS (LHCb's toolkit for GEANT4 simulations) for a full detector study/simulation.

Each of the 125 NTD stacks of MoEDAL that were exposed during LHC Run-1 had its first Makrofol sheet etched and scanned as previously mentioned to look for signs of a HIP, like a magnetic monopole or a HECO, passing through the sheet.  $7.8\text{m}^2$  of plastic in all was analyzed. There were no candidate events seen. Furthermore, the MMT detector failed to trap any monopole candidates. The information from the full MoEDAL prototype detector that was used during Run-1 is being presented for the first time.

Magnetic monopoles can be found using both MMTs and NTDs. Consequently, the analysis includes both the NTD and MMT detectors collectively. The geometric acceptance of the NTD and MMT detectors from MoEDAL did not overlap during Run-1. Therefore, addition is used to combine the monopole signal that was picked up by the NTD and MMT detectors. However, since we lack a method to identify electrically charged particles trapped in the MMT detectors, we can only use the NTDs for the HECO analysis.

Due to the VELO detector of the LHCb, the primary cause of systematic error in this analysis is the incomplete knowledge of the amount of material between the interaction point and the MoEDAL NTD modules. The LHCb geometry accurately simulates the VELO vacuum vessel and the various VELO detector components within the confines of the LHCb's physics acceptance. However, there are no detailed technical drawings of other VELO components that do not have anything to do with physics such as cables, in-situ electronics, cooling pipes, different flanges, a vacuum pump, and a vacuum manifold. This intervening material is nominally between 0.1 and 8.0 radiation lengths ( $X_0$ ) thick, with an average thickness of about  $1.4X_0$  [134].

The estimate of the material in the Geant4 geometry description is the primary source of systematic uncertainty in this analysis. When compared to the best estimate of the material budget that is compatible with direct measurement and existing drawings, the uncertainty in the material map is modelled by two geometries that represent an excess and a deficit of material, using conservative estimates of uncertainties on material thicknesses and densities.

Uncertainties in the DY acceptances are caused by the systematic uncertainty in the material map. The resulting relative uncertainty for singly charged monopoles,  $|g| = g_D$  is on the order of 10% [105]. With an increase in electric and/or magnetic charge, this uncertainty increases as well. It is in the range of 10% – 20% for inter-

mediate masses of about 1TeV for doubly charged monopoles,  $|g| = 2g_D$ .

The position of the trapping detector, which is uncertain by an estimated 1cm, is another source of systematic error. Simulations indicate that this error is between 1%–17% [105]. The uncertainty in  $\frac{dE}{dx}$  as a function of  $\beta$ , which produces a 1%–10% relative uncertainty in the acceptance [105], is another source of systematic error. Another source of systematic error is on the variable  $p$  caused by the NTD etching and calibration process is shown on the bottom of Figure 3.9 for monopoles and HECOs. This error may result in an error on the threshold value for plastic detection as well as an error in the variation of the angle of incidence of the HIP relative to the NTD. These uncertainties, however, pale in comparison to the error on the material map mentioned earlier. The sources of systematic error listed above were all added in quadrature and included in the calculation of confidence limits.

Using a DY model for HECO and magnetic monopole production as a benchmark, we calculated the 95% C.L upper limits to the cross-section while assuming a  $\beta$ -independent monopole coupling and that the monopole can be of Spin-0, Spin- $\frac{1}{2}$  or Spin-1. The limit curves for HECOs are displayed in Figure 3.25. The trend of the limit curves changes as the HECO charge increases above 50e. This is due to the approximate 50e NTD threshold for detection of highly relativistic HECOs.

For Spin-0, Spin- $\frac{1}{2}$  and Spin-1 monopoles, the cross-section upper limits as a function of mass are shown in Figure 3.26. For HECOs and magnetic monopoles, respectively, Table 3.2 and Table 3.3 list the values of the corresponding 95% C.L. mass limits. We have included exclusive DY production limits for Spin- $\frac{1}{2}$  HECOs, both from photon exchange alone and from photon exchange with  $Z^0$  as well. This enables us to make a comparison of our results with the best charge limit on HECO production previously published by the ATLAS Collaboration [112], which only took into account DY production of HECOs through photon exchange. Due to destructive interference effects,

the cross-section of DY HECO production via photon exchange is slightly larger than that of DY HECO production via photon/ $Z^0$  exchange in the Spin- $\frac{1}{2}$  case and at the mass scale examined in this analysis. Similar Spin- $\frac{1}{2}$  mass limits to those obtained from HECOs produced by DY production via photon exchange only are obtained over the majority of the charge range when this lower cross-section is combined with the harder momentum spectrum and better acceptance of HECOs produced by DY production via photon/ $Z^0$  exchange.

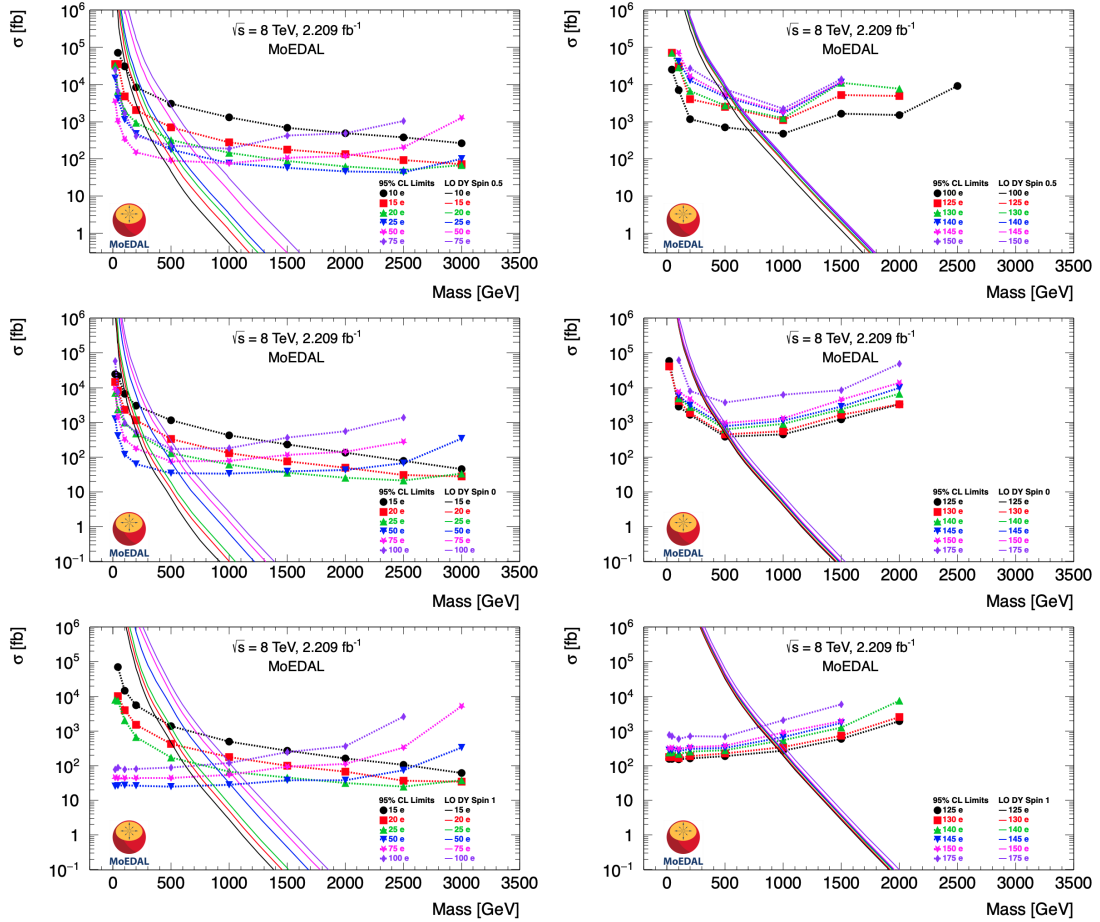


**Figure 3.25:** 95% CL mass limits in a DY production model of Spin-0, Spin- $\frac{1}{2}$  and Spin-1 HECO pair direct production in LHC  $p-p$  collisions.

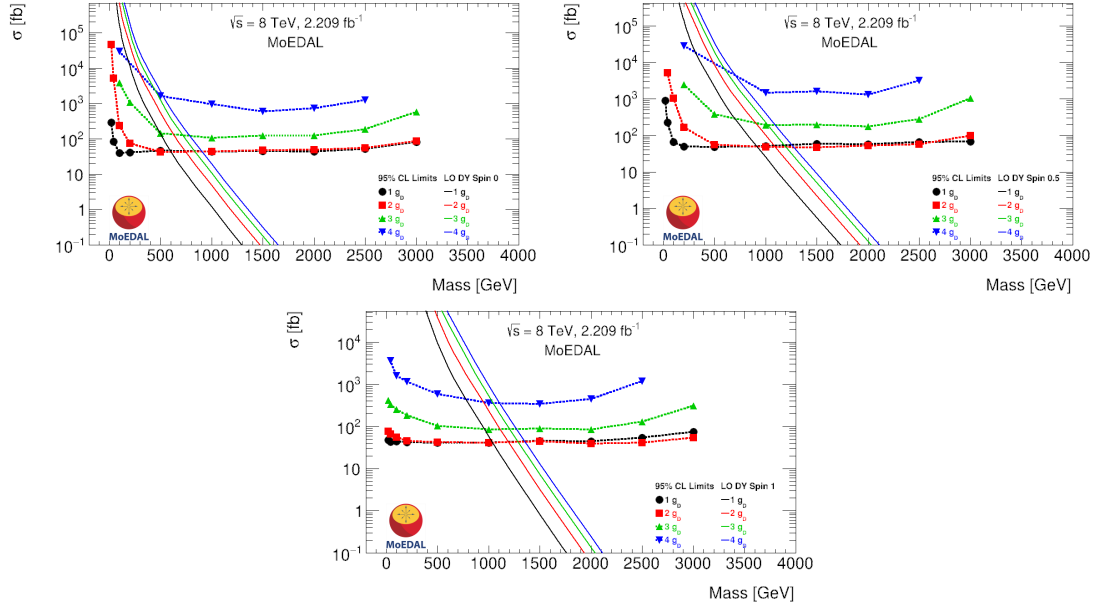


**Figure 3.26:** 95% CL mass limits in a DY production model of Spin-0, Spin- $\frac{1}{2}$  and Spin-1 monopole pair direct production in LHC  $pp$  collisions.

**Table 3.2:** 95% CL mass limits for HECO Pair Direct Production during Run-1 LHC  $p-p$  Collisions, Assuming  $\beta$ -Independent Couplings

	Electric Charge (e)											
	15	20	25	50	75	100	125	130	140	145	150	175
Spin	95% CL mass limits [GeV]											
0	110	190	310	580	580	560	510	510	490	470	460	380
1/2 ( $\gamma$ -exchange)	310	440	560	800	780	730	650	640	600	590	550	-
1/2 ( $\gamma/Z^0$ -exchange)	300	430	560	780	750	710	650	640	590	-	-	-
1	400	570	740	1010	1020	1000	970	950	930	921	900	850

**Table 3.3:** 95% CL mass limits for Monopole Pair Direct Production during Run-1 LHC  $p-p$  Collisions, Assuming  $\beta$ -Independent Couplings

	Magnetic Charge ( $g_D$ )			
	1	2	3	4
Spin	95% CL mass limits [GeV]			
0	590	740	710	520
1/2	910	1090	1020	700
1	1030	1190	1190	1110

### 3.3.15 Conclusions

During LHC Run-1, the prototype NTD system and aluminum components of the MoEDAL MMT detector were both subjected to 8TeV LHC collisions. Both detector systems were checked for the presence of magnetic monopoles and/or HECOs at the conclusion of LHC Run-1. Using semi-automatic and manual optical microscopes, the NTDs were etched and scanned to look for signs of a magnetic monopole or a HECO. A SQUID-based magnetometer was also used in the MMT case to check for the presence of trapped magnetic charge.

This is the first time that search results using NTD detectors have been utilized in a MoEDAL analysis. Only MMT detectors from MoEDAL were used in earlier MoEDAL searches [105]. The HIP search was therefore restricted to magnetic monopoles. The highly ionizing signature of the HIP can be registered in this search thanks to the use of the NTDs. This makes it possible to detect HIPs (HECOs) that are both magnetically and electrically charged. There were no candidates for magnetic monopoles. Limits on the DY production of magnetic monopole pairs were subsequently set for magnetic charges up to  $4g_D$  and mass as high as 1.2TeV for cross sections between approximately 40fb and 5pb.

These limits pale in comparison with those of the most recent Run-2 collider [108,112] despite the use of both the MMT and NTD sub-detectors. This is caused by a combination of factors, including Run-1's lower luminosity,  $E_{CM}$  and DY cross-section compared to Run-2 and Run-1's limited acceptance of MoEDAL's MMT and NTD prototype detectors compared to Run-2. There was no evidence for DY produced HECO pairs during this analysis. As a result, limits were placed on the DY production of HECO pairs with cross-sections ranging from approximately 30fb to 70pb, for electric charges between 15e and 175e, and masses between 110GeV and 1020GeV. The limits on DY production of HECOs is currently the strongest of any collider

experiment in terms of charge reach.

## 3.4 The Search for Dyons

*About 800kg of Aluminum are contained in the MoEDAL trapping detector. At the LHCb interaction point (IP8), it was subjected to  $6.46\text{fb}^{-1}$  of 13TeV proton-proton collisions during LHC Run-2. The aluminium volumes that make up the detector were subjected to a SQUID magnetometer in order to look for evidence of dyons (particles with electric and magnetic charge), which were captured in the trapping detector. A persistent current that would be induced in the SQUID magnetometer would indicate the presence of a trapped dyon. We exclude dyons with magnetic charges up to five Dirac charges ( $5g_D$ ) and electric charges up to 200 times the fundamental electric charge for mass limits in the range of 750GeV to 1910GeV, as well as monopoles with magnetic charges up to and including five Dirac charges for mass limits in the range of 870GeV to 2040GeV, on the basis of a Drell-Yan production model.*

### 3.4.1 Introduction

Since Dirac showed in 1931 [1] that the existence of the magnetic monopole is consistent with quantum mechanics under the condition that the quantization condition (in SI units)  $\frac{g}{e} = n \left(\frac{c}{2\alpha}\right)$  is satisfied, where  $g$  is the magnetic charge,  $e$  is a unit electric charge,  $c$  is the speed of light,  $\alpha$  is the fine structure constant, and  $n$  is an integer. This is also reflected in Equation 1.42. One Dirac charge is indicated by when  $n = 1$ , then  $g = g_D$ .

Direct searches for magnetic monopoles have been conducted for a very long time at accelerators [135], most recently at the LHC [69, 104–108, 112]. In addition, there have been extensive searches for monopole relics from the early Universe in cosmic rays and in materials [45, 101, 113].

### 3.4.2 Theory

Julian Schwinger first postulated the existence of the dyon, a particle with both a magnetic and an electric charge, in 1969 [118]. By taking into account the interaction of two dyons, Schwinger obtained the following charge quantization condition,

$$e_1 g_2 - e_2 g_1 = \frac{n}{2} \hbar c \quad (3.10)$$

where  $e_1$ ,  $e_2$  and  $g_1$ ,  $g_2$  are the electric and magnetic charges of the two dyons, respectively. The electric charge of the dyon is not fixed by this quantization condition on its own and there is no a priori restriction on the size of the electric charge of the dyon. However, semi-classical reasoning has extensively examined the matter of the charge of the quantum dyon [136–139] and it has been determined that in CP-conserving theories, the dyon charge is quantized as an integer multiple of the fundamental charge,  $q = ne$ .

This is no longer the case when the theory accepts CP non-conservation (or when CP conservation is violated). The vacuum angle  $\theta$ , or "theta term", which may be introduced to the Lagrangian for the Yang-Mills theory without impairing renormalizability, characterizes the topologically nontrivial vacuum structure of non-Abelian gauge theories. The non-Abelian monopole of 't Hooft and Polyakov was created by the Georgi-Glashow model, which Witten [140] explored in the context of, demonstrating that dyons are magnetic monopoles with fractional electric charge. The relationship between the electric charge of the dyon and  $\theta$  was derived by Witten and it reads as such,

$$q = ne - \frac{e\theta}{2\pi} \quad (3.11)$$

According to experimental data, CP is only weakly violated. One would expect the dyon charge to have a value that is nearly but not quite an integer since the deviation from integer charge of the monopole is proportional to the intensity of the

CP violation. In several particle-physics theories, including Grand Unified Theories

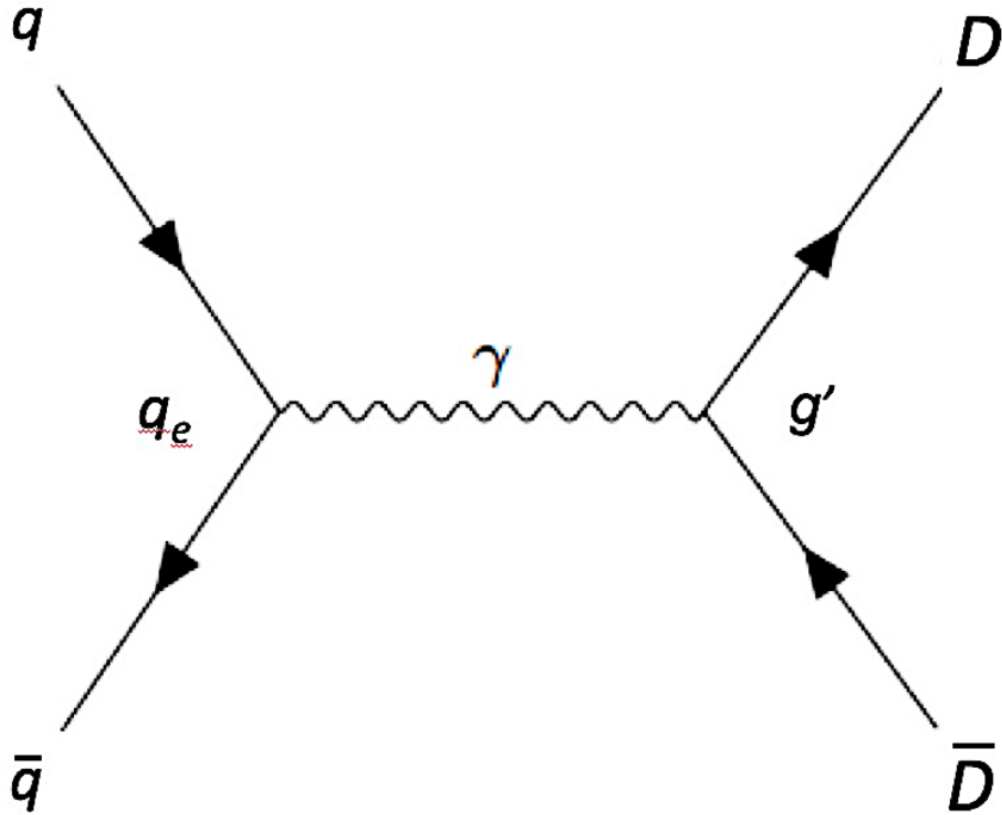


**Figure 3.27:** A Feynman-like diagram for the benchmark Drell-Yan mechanism used in direct dyon-dyon pair production at leading order. In the eikonal approximation, which is applicable for LHC energy, the coupling  $g'$  is given by  $\sqrt{g^2 + q^2}$ .

(GUTs), Einstein-Yang-Mills theories, Kaluza-Klein theory, string theories, and M-theories, it has been demonstrated, since Schwinger's original work, that in general, dyons do appear in theories with monopoles. Additionally, other theoretical hypotheses have been proposed that include electroweak (EW) dyons and monopoles that might be discovered in the LHC or the High-Luminosity LHC (HL-LHC) [141]. We also point out that cosmology would be significantly affected by the generation of such EW dyons and monopoles during the EW phase transition in the early Universe [142].

In principle, the electric charge of a dyon may be quite large. Q-balls [120, 121], aggregates of  $ud$ - [122], or  $s$ -quark matter [123], and the remnants of microscopic black holes [124] are a few further suggested instances of highly electrically charged objects

(HECOs) which are (pseudo-) stable. Additionally, extensive accelerator searches for HECOs have been made [100, 102, 104]. An earlier excluded charge range of  $20 < |z| < 60$  [104] has recently been expanded by ATLAS to  $60 < |z| < 100$  [112], where  $z$  is the electric charge [143]. At the time of writing, there are no prior accelerator searches for dyons. In accelerator-based searches for monopoles [69, 104–108, 112], the Drell-Yan (DY) production mechanism is widely used because it offers a straightforward benchmark model of monopole-pair formation.

As a baseline for dyon production, we utilize a model of DY production that is comparable here. The same spins of Spin-0, Spin- $\frac{1}{2}$  and Spin-1 are taken into account as in the earlier MoEDAL monopole searches [107, 108], and models were created in MadGraph5 [90] using the Universal FeynRules Output detailed in Ref. [129]. For the DY process, we employed tree-level diagrams and the Parton distribution functions NNPDF23 [144]. In the fundamental DY cross-section,  $g^2 + q^2$  replaces the square of the magnetic charge of the monopole,  $g^2$ , where  $q$  represents the electric charge of the dyon as previously described. In other words, in the case of the dyon,

$$g^2 \rightarrow g^2 + q^2 \tag{3.12}$$

This scaling is consistent with the dual effective theory proposed by Milton and Gamberg [145, 146] and when applied to dyons, the theoretical framework provided for monopoles in Ref. [129].

Due to the dyon's electric charge, there are two significant differences between the signature of a dyon and that of a magnetic monopole at the LHC. Firstly, relativistic monopole with a magnetic charge of  $ng_D$  where  $n \geq 1$  and a fractional velocity of  $\beta = \frac{v}{c}$  has a different ionization energy loss mechanism as compared to an electrically charged particle. The Ahlen formula 3.5 and 3.6 suggests that a relativistic monopole loses a lot of energy when the velocity of the monopole is large and the Bethe-Bloch formula 3.4 suggests the inverse is true for an electrically charged particle. On the

other hand, the ionization energy loss of a dyon is equal to the sum of the energy losses brought on by its magnetic and electric charges, each of which has a unique velocity dependency.

Secondly, in a solenoidal field, the magnetic monopole moves on a curved trajectory in the  $r - z$  plane without bending in the transverse plane. Here,  $z$  denotes the direction of the field lines and  $r$  is the radial dimension. This is the exact opposite of how an electrically charged particle would behave in the same field. In contrast, the trajectory of a dyon in a solenoidal field is curved in both the  $r - z$  plane and the plane transverse to the  $r - z$  plane. Thus, the dyon follows a different path as compared to an isolated electric or magnetic charge.

### 3.4.3 Detection of Dyons in MoEDAL

When a monopole or dyon passes through MoEDAL, its reaction is significantly different from that of ATLAS and CMS, the general-purpose LHC experiments. The MoEDAL detector, installed at Interaction Point 8 (IP8) of the LHC along with LHCb, uses two novel passive detection techniques tailored for finding highly ionizing particles (HIPs).

The first, which was used in this analysis, uses a trapping detector, the Magnetic Monopole Trapper (MMT), weighing approximately 800kg and made of 2400 Aluminum bars to trap HIPs for further research. The second is made up of 186 Nuclear Track Detector (NTD) stacks in an array. 1m to 2m from IP8, MMT volumes are deployed upstream (known as the forward MMT) and on both sides (known as the side MMT) in three approximately equal masses.

The ETH Zurich Laboratory for Natural Magnetism houses a SQUID magnetome-

ter which is used to detect magnetic charge. After the MMTs have been exposed to LHC collisions, they are passed through the SQUID. More details on MoEDAL's sub-detectors can be found in Section 2.2 as well as Ref. [78, 134].

As of writing, the only experiments to report limits on monopole production at the LHC are ATLAS and MoEDAL [69, 104–108, 112]. The combined photon-fusion and DY monopole-pair production methods are included in MoEDAL's most recent search results [108], with the former process occurring for the first time at the LHC. As of writing, the strongest limits on magnetic charges to date for a collider experiment were set using  $4.0\text{fb}^{-1}$  of data to set mass limits between  $1500\text{GeV}$  and  $3750\text{GeV}$  for Spin-0, Spin- $\frac{1}{2}$  and Spin-1 monopoles, as well as cross-section upper limits as low as  $11\text{fb}$ . These limits are based on an unambiguous signature and a direct search for magnetic charge. A recent ATLAS search [112] set 95% Confidence Level (C.L.) mass limits of  $1850\text{GeV}$  and  $2370\text{GeV}$  for the DY production of Spin-0 and Spin- $\frac{1}{2}$  monopoles with charge  $1g_D$  respectively. For charge  $2g_D$  monopoles, the equivalent ATLAS limits are  $1725\text{GeV}$  and  $2125\text{GeV}$  respectively. Based on the ionizing properties of magnetic monopoles or dyons, these are now the best limits in the world for magnetic charge  $g_D = 2$ .

Due to the interaction between the monopole and the nuclear magnetic moment, a monopole is assumed to be stopped when its velocity,  $\beta$ , falls to  $10^{-3}$  and then bound to the nucleus [75–77, 132]. A predicted monopole-nucleus binding energy (BE) of  $0.5\text{MeV}$  to  $2.5\text{MeV}$  [132] is given by the anomalously large magnetic moment of Aluminum. These binding energies are comparable to the splittings in the shell model. Therefore, it is a reasonable assumption that the high magnetic field around the monopole will in any event cause the nucleus to rearrange, enabling it to form a strong bond with the monopole. Monopoles with this BE will be permanently bound, requiring fields greater than approximately  $5\text{T}$  to free them, according to Ref. [132]. We note that the MMT volumes are never exposed to such intense magnetic fields.

When the velocity,  $\beta$ , of the dyon falls to  $10^{-3}$ , it is also expected to stop. However, the electric charge of the dyon makes binding to the nucleus an ambiguity. We make the conservative assumption that only dyons with negative electric charges are bound in our analysis because, in this case, their Coulomb attraction to the positive charge of the nucleus strengthens the interaction between its magnetic charge and the large anomalous nuclear magnetic moment of the aluminum nucleus. The assumption that DY produces dyon-antidyon pairings implies indirect sensitivity to positively-charged dyons at the same level, despite the trapping condition requiring the dyon to be negatively electrically charged. As was described in Section 2.2, if a magnetic monopole is trapped in the MMT's Aluminum bars, it is identified and measured as a persistent current in the coil of the SQUID. Note that the coil is looped around the transport axis of the Aluminum bars.

A dc SQUID long-core magnetometer (2G Enterprises Model 755) installed at the Laboratory for Natural Magnetism at ETH Zurich was used to scan all 2400 trapping detector samples in 2018. By multiplying the measured magnetometer response by a calibration constant,  $C$ , a magnetic pole  $P$  in Dirac charge units is obtained. Two different techniques, which are both described in more detail in Section 2.2, were used to calibrate the device. The first method, based on the superposition principle, combines measurements made at 1mm intervals with a dipole sample of known magnetic moment  $\mu = 2.98 \times 10^6 \text{Am}^2$  to determine the response of a single magnetic pole of strength  $P = 9.03 \times 10^5 g_D$ . The second method employs a long, thin solenoid that provides  $P = 32.4 g_D \mu\text{A}^{-1}$  for a range of currents between  $0.01 \mu\text{A} - 10 \mu\text{A}$  to directly measure the impact of a magnetic pole of known strength. Figure 3.28 displays the calibration measurement results along with the calibration constant that was determined using the first method. The calibration uncertainty in the pole strength can be thought of as the 10% difference between the two methods. In the range of  $0.3 g_D - 300 g_D$ , the magnetometer response is observed to be linear and charge symmetric. Through-

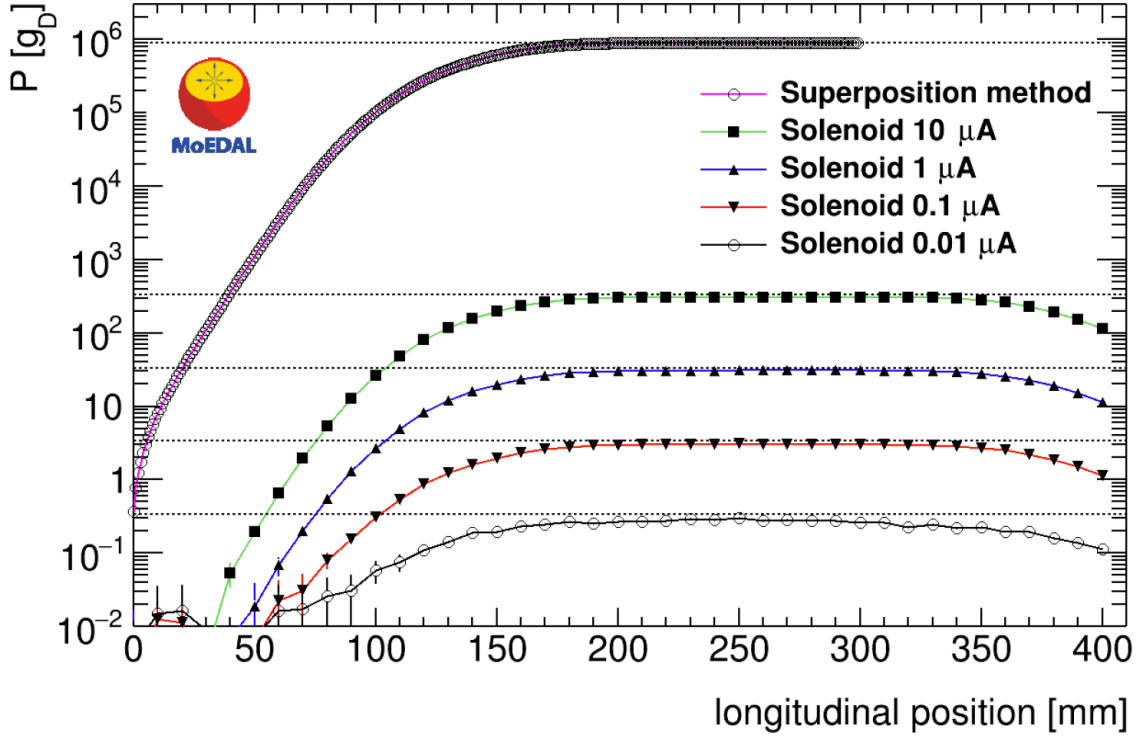


**Figure 3.28:** Results of the calibration measurements with the superposition method using a magnetic dipole sample, and the solenoid method with  $P = 32.4g_D\mu\text{A}^{-1}$  and various currents. The dashed lines represent the expected plateau values in units of Dirac charge. The calibration constant is tuned using the measurement from the superposition method.

out the campaign, the plateau value of the calibration dipole sample was repeatedly measured and found to be stable to within less than 1%. Three samples at a time, separated by a distance of 46cm, were loaded onto a moveable conveyer tray made of carbon fiber and moved through the magnetometer’s sensing region. Due to the fact that speed increases the likelihood and size of potential spurious offsets, the transport speed was set to the lowest possible level of  $2.54\text{cm s}^{-1}$  [107]. A persistent current in the superconducting coil surrounding the transport axis that represents the magnetic charge present in a sample is used to measure it. This is the difference between the currents measured before ( $I_1$ ) and after ( $I_2$ ) a sample has passed through the sensing coil, after the corresponding contributions of the empty trays ( $I_2^{\text{tray}}$  and  $I_1^{\text{tray}}$ ) have been taken into account. Equation 3.2 calculates the magnetic pole strength present in a sample and expresses it in terms of Dirac charges. The results of the two scans on each sample are depicted in Figure 3.29. During their passage through the superconducting loop, the samples are not exposed to any external magnetic fields that might

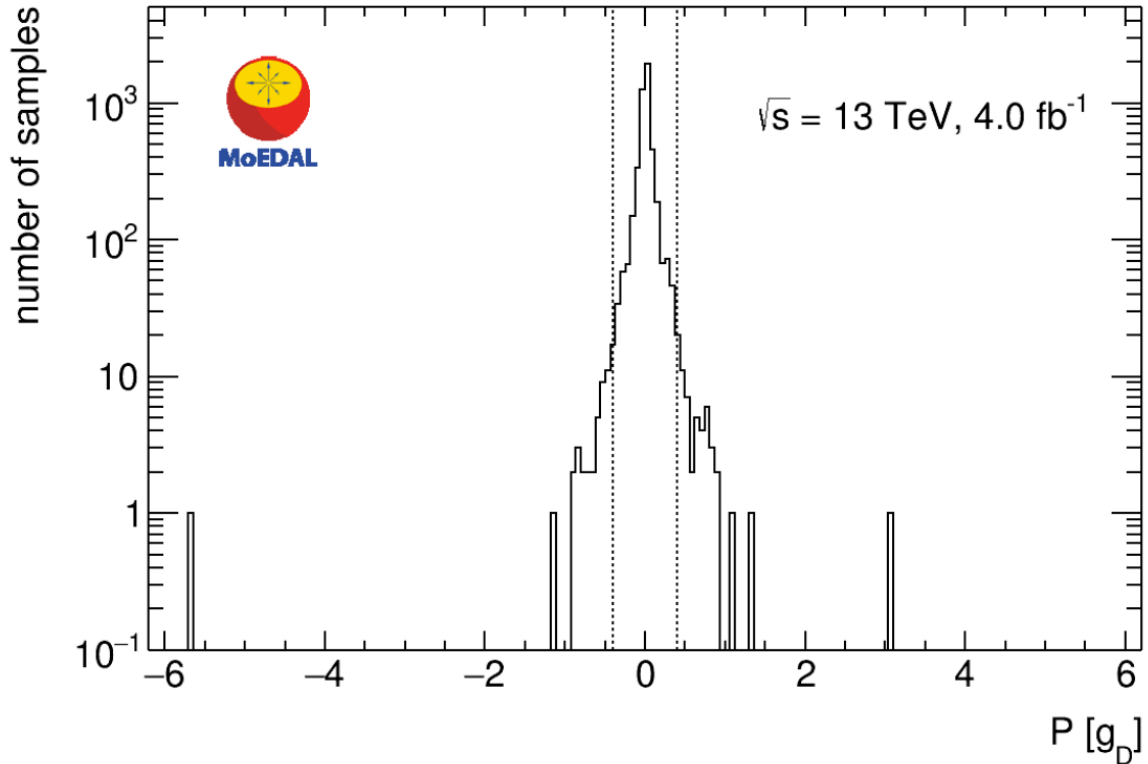


**Figure 3.29:** Magnetic pole strength (in units of Dirac charge) measured in the 2400 aluminum samples of the MoEDAL trapping detector exposed to 13TeV collisions in 2015 – 2017, with every sample scanned twice.

potentially free a monopole from the material. The ferromagnetic impurities in the sample, noise currents in the SQUID feedback loop, and other well-known instrumental and environmental factors may cause spurious flux jumps that cause the observed outliers [105]. The sample was regarded as a candidate whenever the measured pole strength in either of the two measurements deviated from zero by more than  $0.4g_D$ . False negative results are greatly diminished by this process. Thus, 87 candidate samples in total were found. Repeated measurements of a sample with a real monopole would always produce the same nonzero result, whereas repeated measurements of a sample without a monopole would always produce results consistent with zero. As can be seen in Figure 3.30, the candidates were repeatedly scanned, and it was discovered that the majority of the measured pole strengths for each candidate fell below the cutoff of  $0.4g_D$ . At least two scans were performed on each MMT sample. A sample containing a dyon would repeatedly and consistently produce non-zero measurements that correspond to the magnetic charge of said dyon. Values that are consistent with

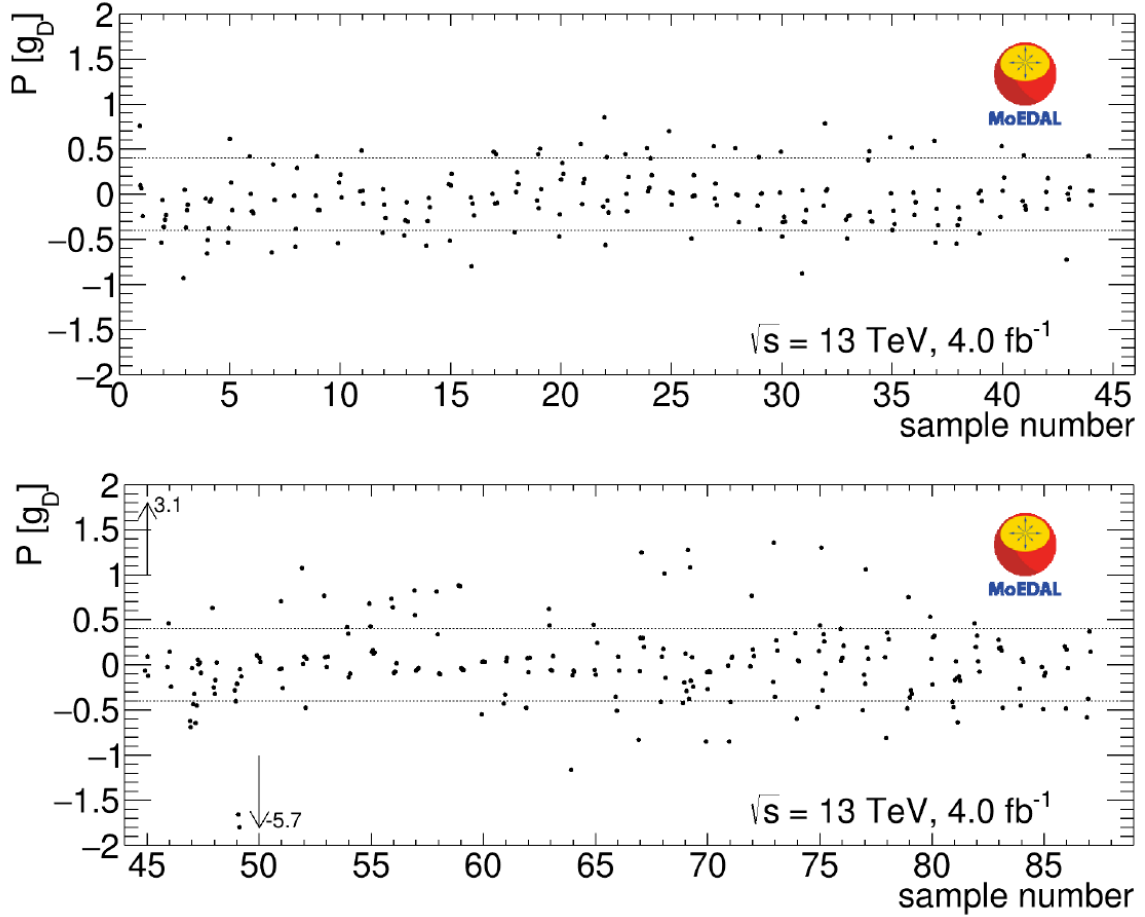


**Figure 3.30:** Results of multiple pole strength measurements (in units of Dirac charge) for the 87 candidate samples for which at least one of the two first measurement values was above the threshold  $|g| > 0.4g_D$ . More values are observed below threshold than above threshold for all of them, excluding the presence of a monopole with  $|g| > g_D$ .

zero would be recorded in the absence of a dyon. A sample is deemed a candidate if its measured pole strength, in any or both of the two initial measurements, deviates from zero by more than  $0.4g_D$ . The likelihood of false negatives was greatly decreased in this method.

In total, 87 candidates were found in the data collected in 2015, 2016 and 2017, which corresponds to  $4.0\text{fb}^{-1}$ . In the 2018 data (LHC Run-2), where  $2.46\text{fb}^{-1}$  of luminosity was recorded, only 29 candidates were obtained. We repeatedly scanned the MMT volumes that contained dyon candidates. The bulk of the measured pole strengths for each candidate were determined to be below the cutoff of  $0.4g_D$ . For a charge of  $\pm 1g_D$ , it was discovered that the greatest likelihood of missing a dyon in a single measurement was 0.53%. During Run-A of the LHC (2015–2017), two

passes were made for each sample, therefore the chance of missing the dyon twice is extremely unlikely – a mere 0.0028%. Additionally, it was discovered in LHC Run-A data that candidate events were associated with SQUID signal fluctuations that were larger than average. Using the 87 candidate events obtained during Run-A of the LHC, it was determined that the likelihood of missing a Dyon candidate in this situation was 0.2%. These odds decrease as magnetic charge rises.

To quantify the probability of a false negative the distribution of the measured persistent current was fitted using the sum of four Gaussian curves centred around zero with different amplitudes and width. The resulting fitted curve was integrated over the relevant ranges in order to extract the probability of mis-measurement in this range and the the probability that a dyon contained in the sample would yield a persistent current below threshold and be missed. In order to obtain a conservative estimate of the probability to miss a dyon candidate, a fit was performed on the data taken in Run-A only. We did not use the Run-B (2018) data in this estimate since it was taken after a major overhaul of the SQUID magnetometer which reduced the random fluctuations of the signal of the SQUID. The maximum probability for missing a monopole in a single measurement was found to be 0.53% for a charge of  $\pm 1g_D$ . As two passes were made for each sample during Run-A we have the negligible probability of missing the dyon twice of 0.0028%.

There was also the possibility that we mis-measured several times while performing the multiple measurements performed on candidate events. In the Run-A data candidate events were associated with greater than average fluctuations in the SQUID signal. A fit was performed to the measured currents for all measurements made on the 87 candidate events. In this case the maximum probability of missing the dyon in a single measurement is 6.5% for a charge of  $1g_D$ . With the criterion that we should have more measurement below threshold than above and considering that there were at least four re-measurements for each candidate, the worst case was where we miss

three candidates out of five for a charge of  $1g_D$ . The probability for this eventuality is 0.2%.

### 3.4.4 Acceptance of the Run-2 MoEDAL MMT Sub-Detector

The acceptance for the MMT sub-detector system, as was mentioned in Section 2.2, is defined to be the fraction of events in which at least one dyon of the pair produced dyons is trapped in the MMT. The ionization energy loss of dyons when they pass through matter [30, 97, 147, 148] and the information of the material the dyon traverses [105, 134] are used to establish the trapping condition, which is then implemented in a simulation called GAUSS, based on GEANT4 [84]. The kinematics and overall trapping acceptance are determined by the pair-production model for a given dyon spin and mass. Uncertainties in the material description account for the majority of the uncertainty in the acceptance [105–107]. By simulating the addition and removal of hypothetical material from the nominal geometry model, this contribution may be estimated. It must be noted that the NTD sub-detector system was not used in this analysis (although in principle, it could have been).

Three factors contribute to acceptance loss. The first is brought on by the constrained geometrical range of the MMT detector and the spin reliance of the geometrical acceptance. The second is due to the smaller effective ionizing power carried by the heavier and slower dyons passing right through the MMT detector. Recall that the energy loss per unit distance is directly proportional to velocity in the case of magnetic charge as per the Ahlen formula 3.5 and 3.6. The third is due to the fact that the dyon may be absorbed in the material comprising the VELO detector which encompasses IP8 before it reaches the MMT detector.

The maximum acceptance is for dyons with Spin-1 and magnetic charge  $2g_D$ , where the acceptance is greater than or equal to 2.1% for masses up to 3TeV and electric charges up to 50e. For dyons that carry a magnetic charge of at least  $6g_D$  and for all

values of electric charge, the acceptance is less than 0.1% for the whole mass range taken into account. This study is sensitive to dyon electric and magnetic charges up to a maximum of approximately  $200e$  and  $5g_D$ , respectively. The material that particles which are accepted by the MoEDAL detectors encounter before they reach the detector ranges from  $0.1X_0$  to  $8X_0$  radiation lengths ( $X_0$ ), with an average radiation length of about  $1.4X_0$ . The estimated amount of material in the GEANT4 geometry description, which results in a relative uncertainty of 10% for  $1g_D$  dyons [105], is the main source of systematic uncertainty. When the magnetic and electric charge reaches  $6g_D$ , the level of uncertainty becomes too high for the analysis to be useful for Spin-0 and Spin- $\frac{1}{2}$  dyons. For Spin-1 dyons, however, limits can be set for magnetic charges of  $6g_D$  and electric charges of  $1e$  to  $50e$ .

Figures 3.31 and 3.32 provide an illustration of the MoEDAL MMT acceptance curves for Spin- $\frac{1}{2}$ , Spin-0, and Spin-1 Dyons with magnetic charge  $1g_D$  and electric charges  $25e$  and  $50e$  produced by a DY process using virtual photon exchange respectively. The rest of the acceptance curves are shown in the Appendix 5.2.1 in Figures 5.4 to Figures 5.14.

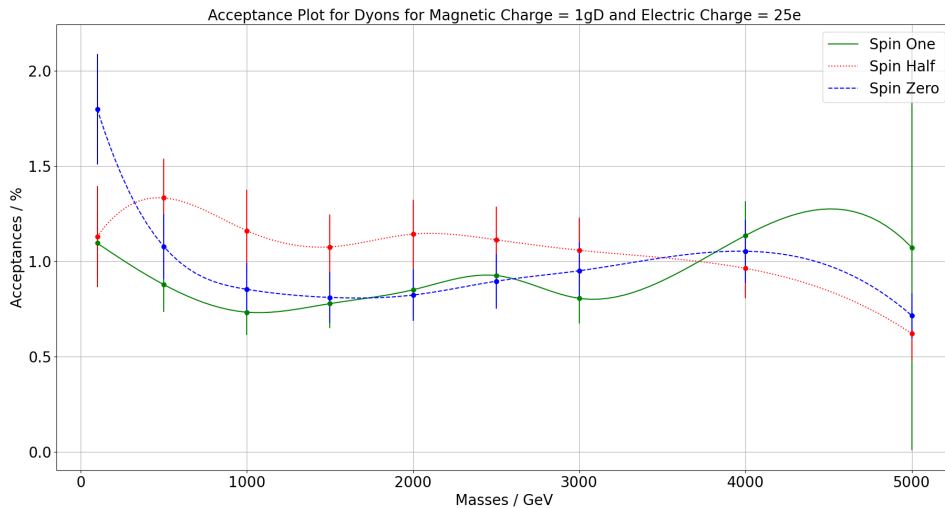


**Figure 3.31:** Acceptance for Spin-0, Spin- $\frac{1}{2}$  and Spin-1 Dyons with Magnetic Charge  $1g_D$  and Electric Charges  $25e$ .

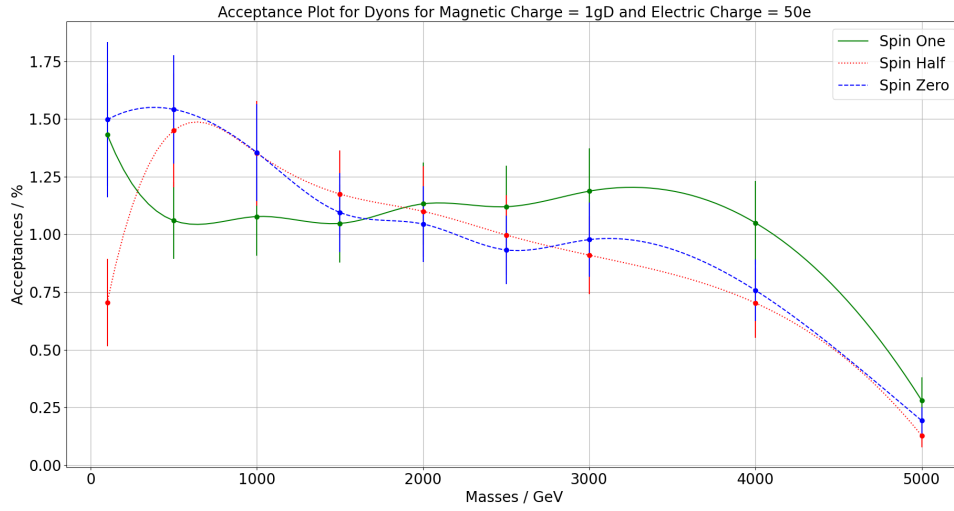


**Figure 3.32:** Acceptance for Spin-0, Spin- $\frac{1}{2}$  and Spin-1 Dyons with Magnetic Charge  $1g_D$  and Electric Charges  $50e$ .

The degree to which the detector elements' arrangement in theta ( $\theta$ ) corresponds to the corresponding theta distribution of the DY-produced Dyons is the primary cause of the difference between the acceptances for Spin-0, Spin- $\frac{1}{2}$  and Spin-1 MMTs. We have compared the kinematic quantities of the uncut signal - momentum ( $p$ ), theta ( $\theta$ ) and phi ( $\phi$ ) - to the corresponding distributions for the events that meet the selection criteria to demonstrate this point. Figure 3.14 defines the theta ( $\theta$ ) and phi ( $\phi$ ) angles.

Given the significant difference between the number of generated and selected events, each plot was normalized to the highest amplitude bins as determined by the Freedman-Diaconis rule [133] in order to make the comparison more understandable. Figures 3.33, 3.34 and 3.35 show the kinematic variables we plotted for the DY production for Spin-0, Spin- $\frac{1}{2}$  and Spin-1 Dyons with a mass of  $1000\text{GeV}$  and an electric charge of  $0e$  respectively. Figures 3.36, 3.37 and 3.38 show the kinematic variables we plotted for the DY production for Spin-0, Spin- $\frac{1}{2}$  and Spin-1 Dyons with a mass of  $1000\text{GeV}$  and an electric charge of  $50e$  respectively.

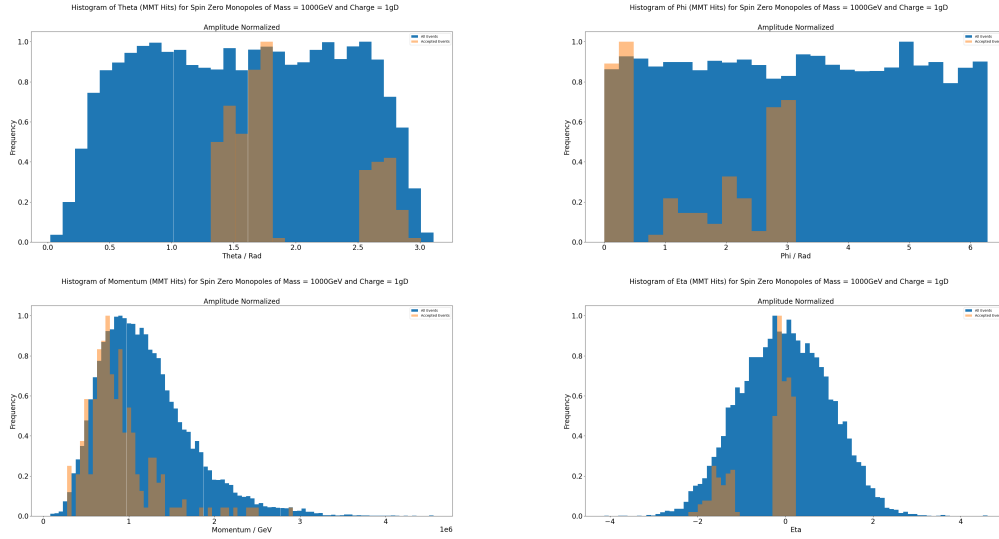


**Figure 3.33:** The  $\theta$ ,  $\phi$ , momentum and  $\eta$  distributions for Spin-0 HECOs of mass 1000GeV and electric charge  $0e$ , produced via the DY process via virtual photon exchange. In each case, 60K events were originally generated. The plots are normalized to the maximum amplitude. The blue histogram represents generated events and the underlying orange histogram shows the distribution of selected events.

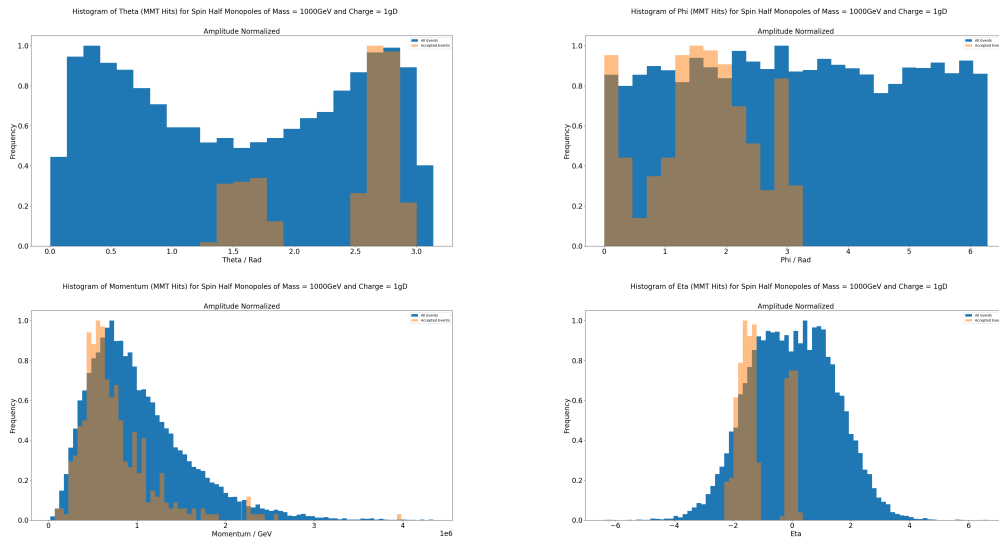


**Figure 3.34:** The  $\theta$ ,  $\phi$ , momentum and  $\eta$  distributions for Spin- $\frac{1}{2}$  HECOs of mass 1000GeV and electric charge  $0e$ , produced via the DY process via virtual photon exchange. In each case, 60K events were originally generated. The plots are normalized to the maximum amplitude. The blue histogram represents generated events and the underlying orange histogram shows the distribution of selected events.

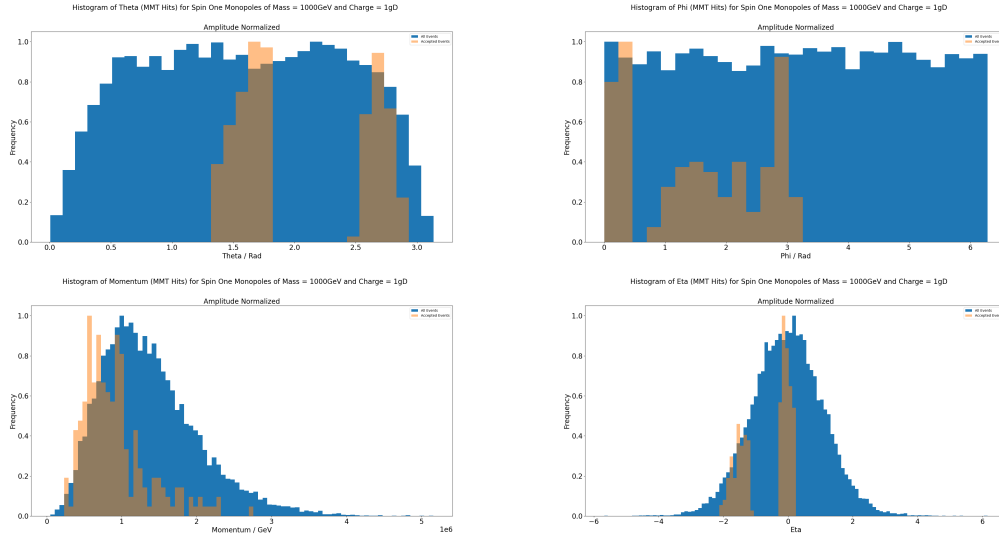


**Figure 3.35:** The  $\theta$ ,  $\phi$ , momentum and  $\eta$  distributions for Spin-1 HECOs of mass 1000GeV and electric charge  $0e$ , produced via the DY process via virtual photon exchange. In each case, 60K events were originally generated. The plots are normalized to the maximum amplitude. The blue histogram represents generated events and the underlying orange histogram shows the distribution of selected events.

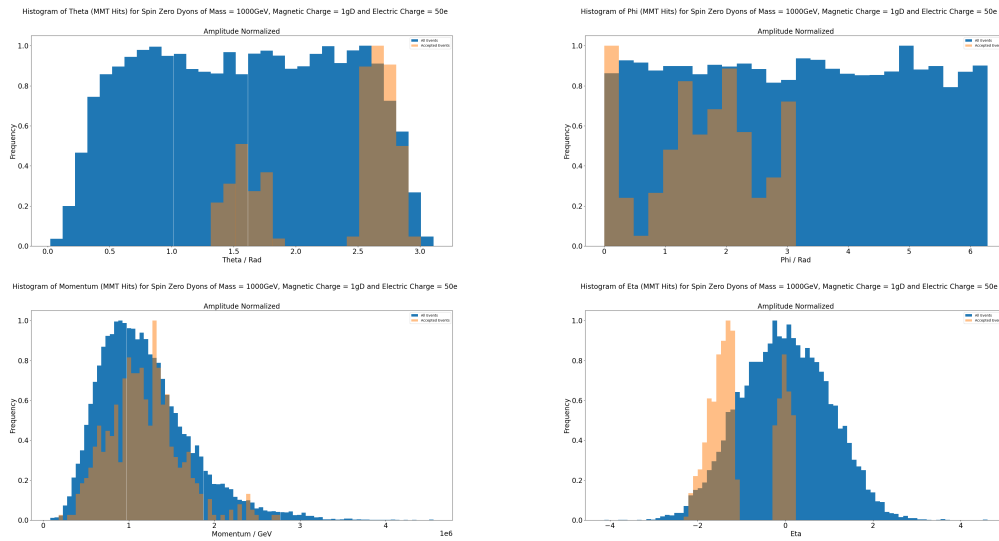


**Figure 3.36:** The  $\theta$ ,  $\phi$ , momentum and  $\eta$  distributions for Spin-0 HECOs of mass 1000GeV and electric charge  $0e$ , produced via the DY process via virtual photon exchange. In each case, 60K events were originally generated. The plots are normalized to the maximum amplitude. The blue histogram represents generated events and the underlying orange histogram shows the distribution of selected events.

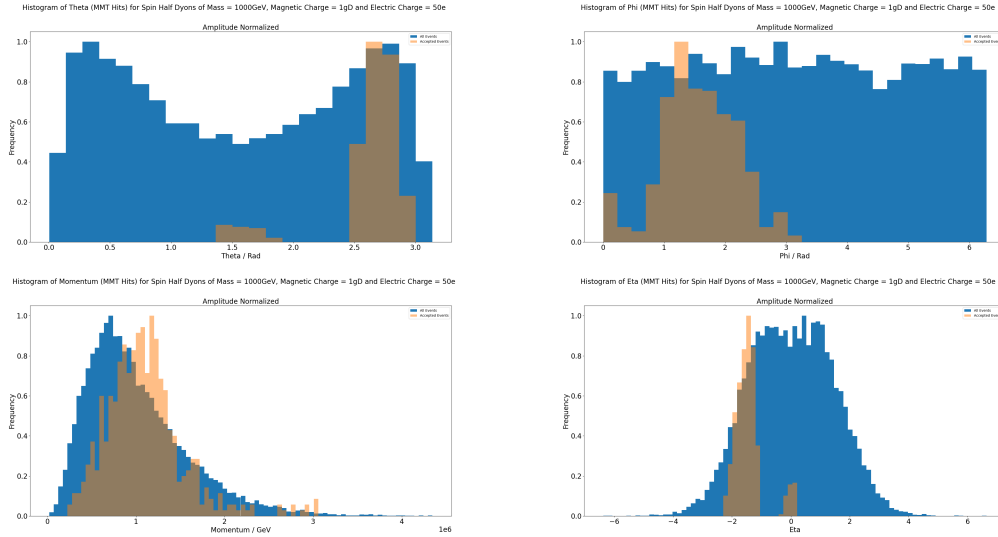


**Figure 3.37:** The  $\theta$ ,  $\phi$ , momentum and  $\eta$  distributions for Spin- $\frac{1}{2}$  HECOs of mass 1000GeV and electric charge  $0e$ , produced via the DY process via virtual photon exchange. In each case, 60K events were originally generated. The plots are normalized to the maximum amplitude. The blue histogram represents generated events and the underlying orange histogram shows the distribution of selected events.

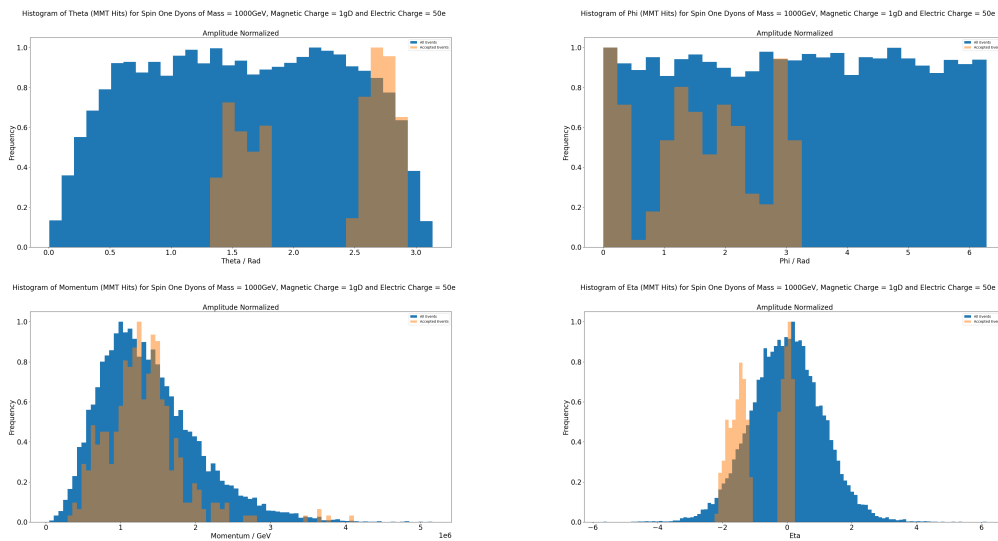


**Figure 3.38:** The  $\theta$ ,  $\phi$ , momentum and  $\eta$  distributions for Spin-1 HECOs of mass 1000GeV and electric charge  $0e$ , produced via the DY process via virtual photon exchange. In each case, 60K events were originally generated. The plots are normalized to the maximum amplitude. The blue histogram represents generated events and the underlying orange histogram shows the distribution of selected events.

### 3.4.5 Analysis Results

Cross-section upper limits at 95% C.L are calculated using a DY model as a benchmark for the production of dyons and magnetic monopoles for a magnetic charge up to  $5g_D$  and an electric charge up to  $200e$  in the case of dyons assuming a  $\beta$ -independent

coupling for 3 spins - Spin-0, Spin- $\frac{1}{2}$  and Spin-1. Due to the material that makes up the VELO detector at the LHCb, located between IP8 and the MMT detector, absorbing greater charges, these figures indicate the upper limit of this search's sensitivity.

Figures 3.39 and 3.40 show the limit plots for DY Spin-0 Dyon-Pair Production. Figures 3.41 and 3.42 shows the limit plots for DY Spin- $\frac{1}{2}$  Dyon-Pair Production. Figures 3.43, 3.44 and 3.45 shows the limit plots for DY Spin-1 Dyon-Pair Production. These limits are obtained based on the estimates of the acceptances and their corresponding uncertainties, the delivered integrated luminosity of  $6.46\text{fb}^{-1}$  corresponding to the full 2015 – 2018 exposure to 13TeV  $p - p$  collisions measured with a precision of 4% [149] as well as the fact that no magnetic charges were observed in the MMTs. Mass limits were obtained and given in Table xx using cross-sections that were computed at leading order. It is crucial to remember that perturbative field theory is usually used to compute such DY cross-sections. However, the monopole-photon coupling is too strong to use perturbative field theory to compute these DY cross-sections. The mass limits provided are therefore simply indicative.

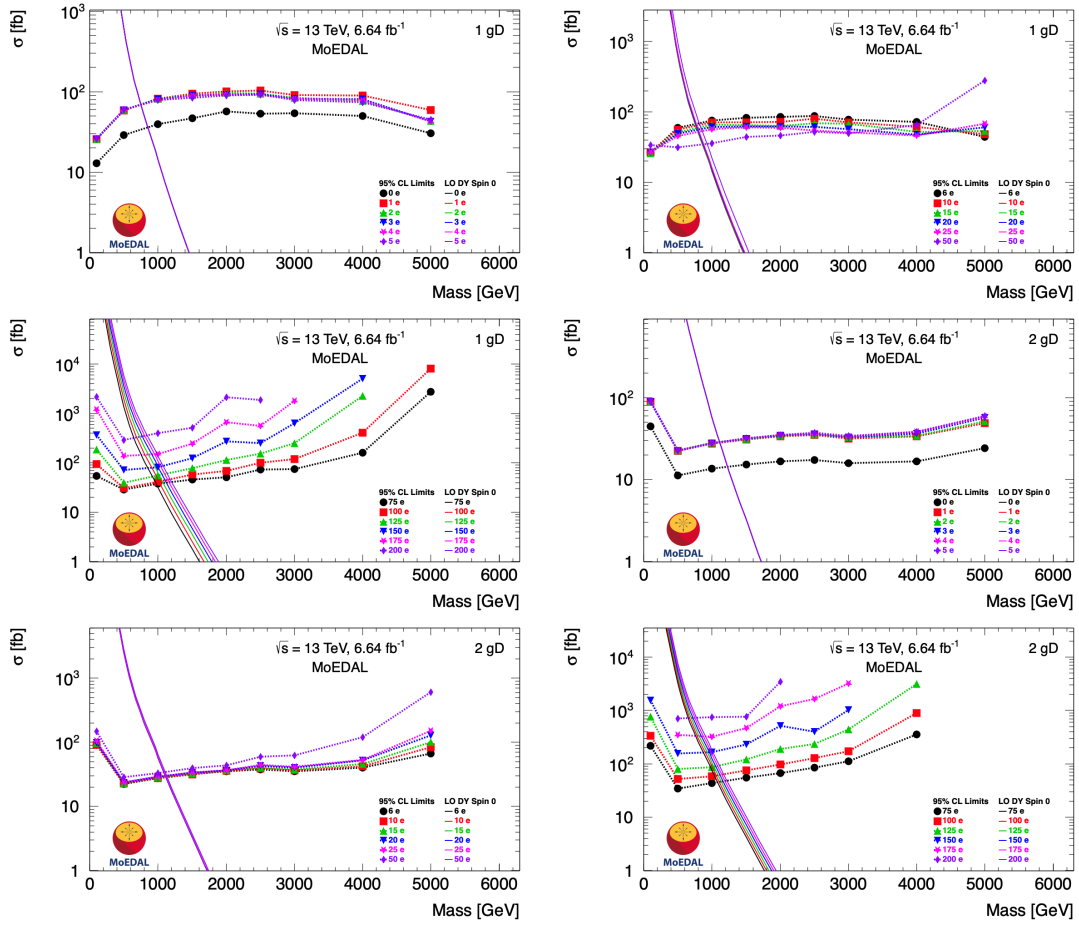


**Figure 3.39:** Cross-section upper limits at 95% C.L. for DY Spin-0 Dyon-Pair Production, with magnetic charges  $1g_D - 2g_D$  and multiple electric charges, in 13TeV  $p - p$  collisions. The solid lines are leading-order cross-section calculations.

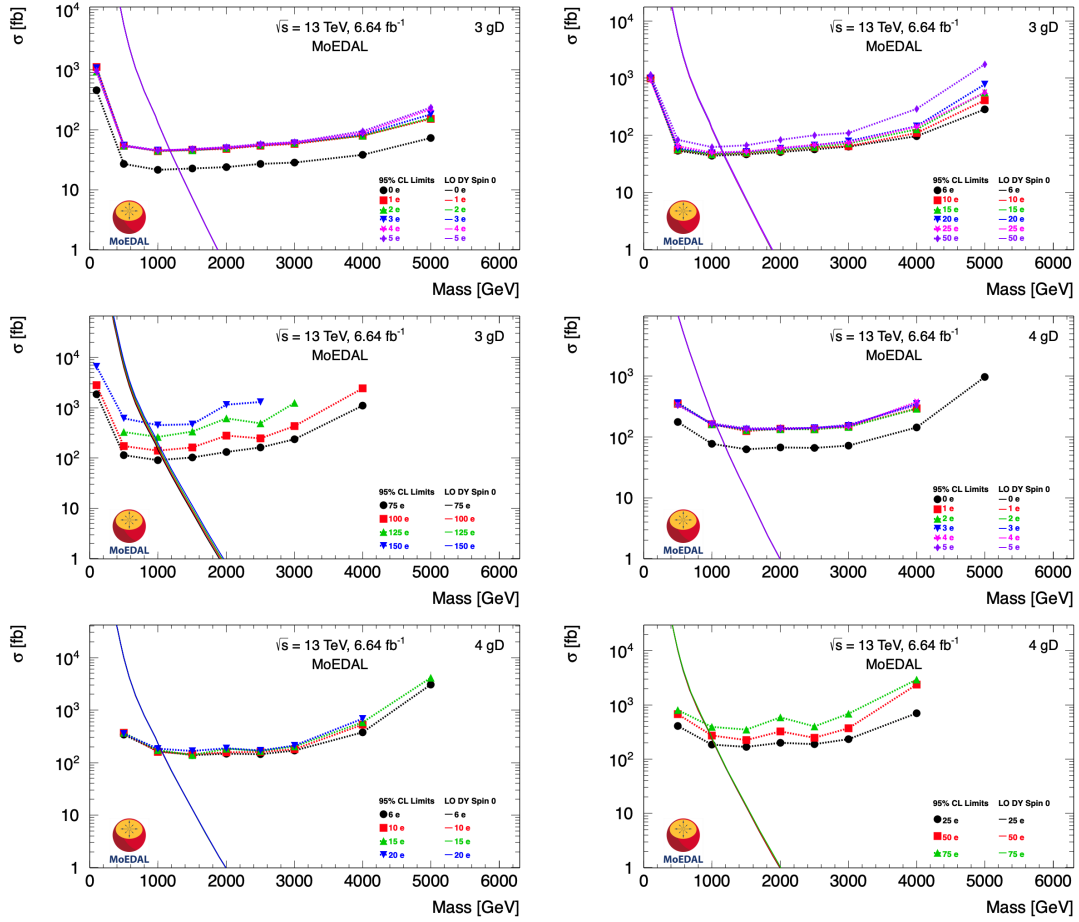


**Figure 3.40:** Cross-section upper limits at 95% C.L. for DY Spin-0 dyon-pair production, with magnetic charges  $3g_D - 4g_D$  and multiple electric charges, in 13TeV  $p - p$  collisions. The solid lines are leading-order cross-section calculations.

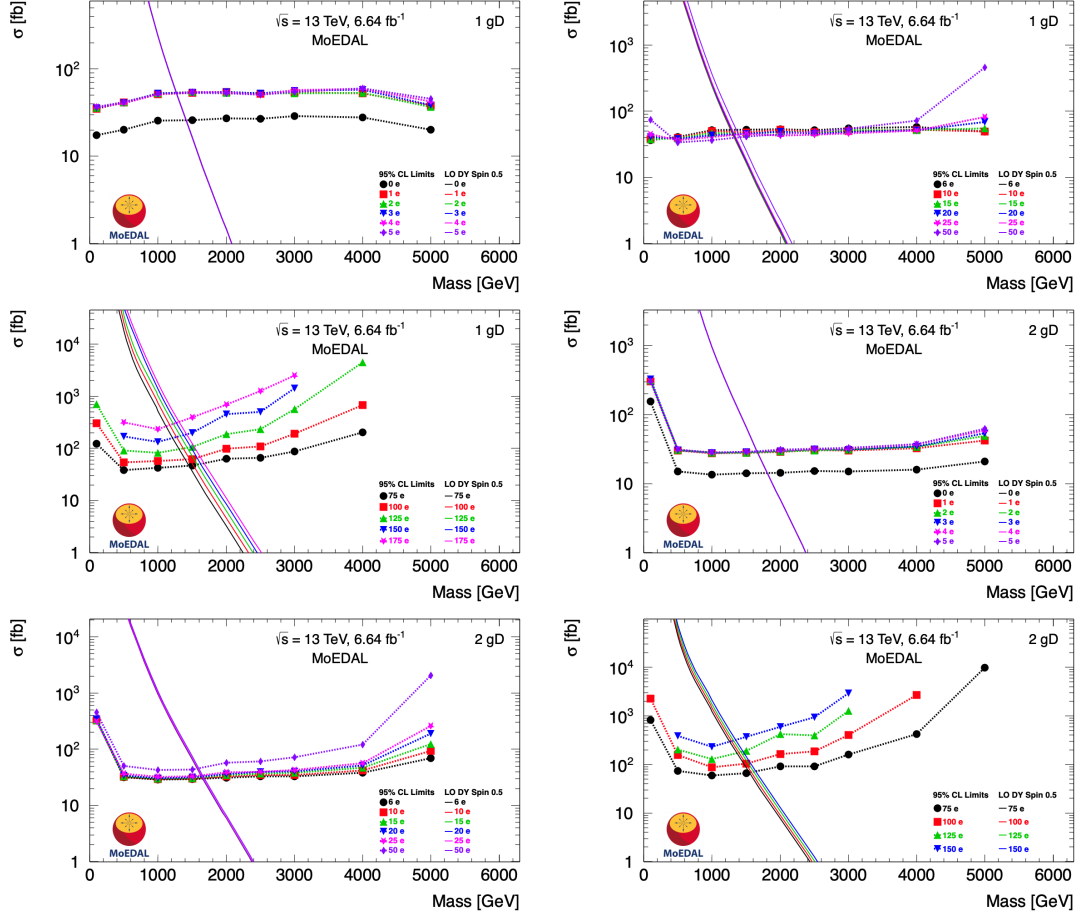


**Figure 3.41:** Cross-section upper limits at 95% C.L. for DY Spin- $\frac{1}{2}$  Dyon-Pair Production, with magnetic charges  $1g_D - 2g_D$  and multiple electric charges, in 13TeV  $p - p$  collisions. The solid lines are leading-order cross-section calculations.

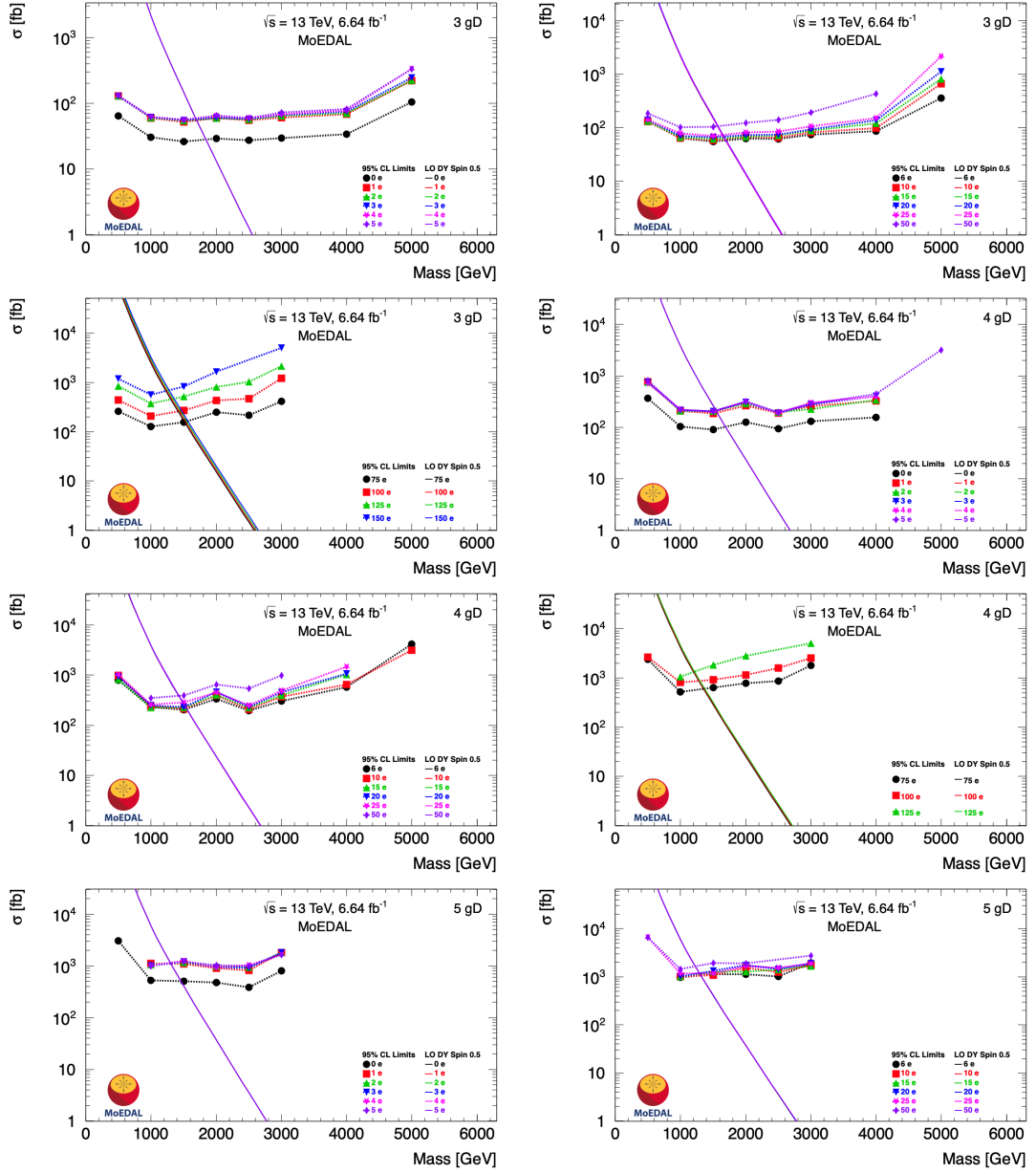


**Figure 3.42:** Cross-section upper limits at 95% C.L. for DY Spin- $\frac{1}{2}$  dyon-pair production, with magnetic charges  $3g_D - 5g_D$  and multiple electric charges, in 13TeV  $p - p$  collisions. The solid lines are leading-order cross-section calculations.

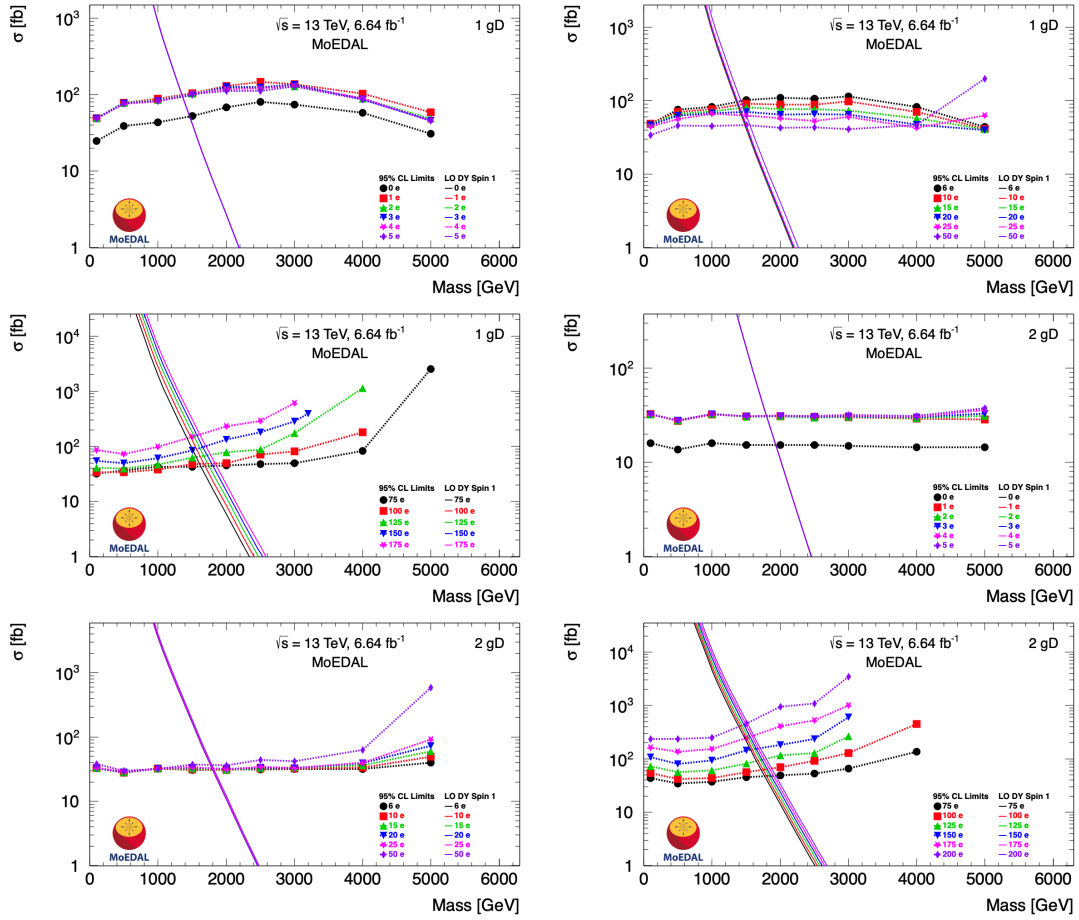


**Figure 3.43:** Cross-section upper limits at 95% C.L. for DY Spin-1 Dyon-Pair Production, with magnetic charges  $1g_D - 2g_D$  and multiple electric charges, in 13TeV  $p - p$  collisions. The solid lines are leading-order cross-section calculations.

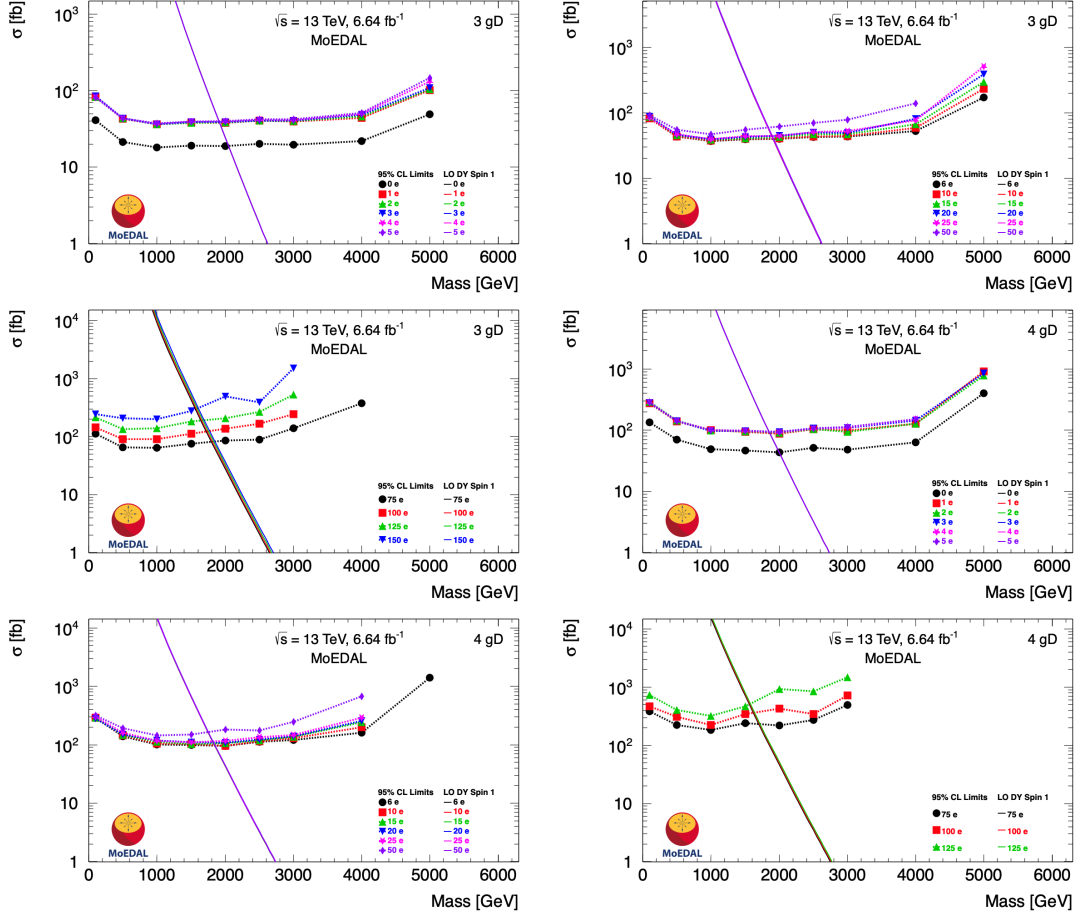


**Figure 3.44:** Cross-section upper limits at 95% C.L. for DY Spin-1 dyon-pair production, with magnetic charges  $3g_D - 4g_D$  and multiple electric charges, in 13TeV  $p - p$  collisions. The solid lines are leading-order cross-section calculations.

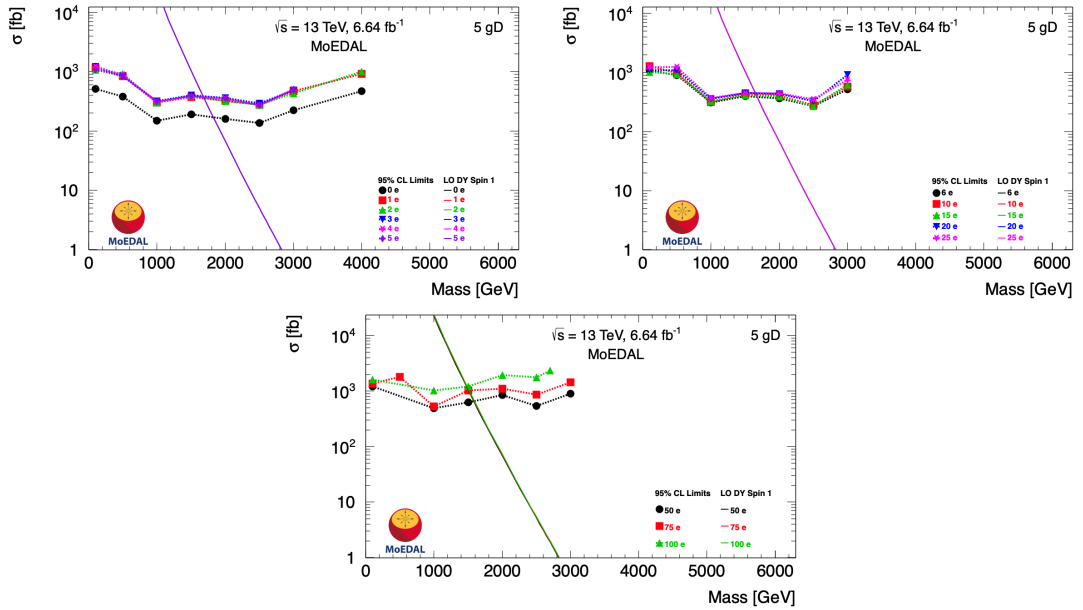


**Figure 3.45:** Cross-section upper limits at 95% C.L. for DY Spin-1 dyon-pair production, with magnetic charge  $5g_D$  and multiple electric charges, in 13TeV  $p - p$  collisions. The solid lines are leading-order cross-section calculations.

**Table 3.4:** 95% C.L. Mass Limits Found in a Drell-Yan Production Model for Spin-0, Spin- $\frac{1}{2}$  and Spin-1 Dyon Pair Direct Production in LHC  $p - p$  Collisions, Assuming  $\beta$ -Independent Couplings

Magnetic Charge / $g_D$	Spin	Electric Charge / e																	
		0	1	2	3	4	5	6	10	15	20	25	50	75	100	125	150	175	200
		95 % C.L Mass Limits / GeV																	
1	0	870	750	750	750	750	750	750	760	780	790	810	920	970	1010	1010	1000	950	840
2	0	1240	1110	1110	1110	1110	1110	1110	1120	1120	1110	1110	1110	1070	1050	1020	950	870	770
3	0	1300	1170	1170	1170	1170	1170	1160	1170	1170	1160	1160	1130	1070	1020	940	850	-	-
4	0	1200	1060	1060	1060	1060	1060	1060	1060	1060	1040	1030	970	900	-	-	-	-	-
1	1/2	1410	1270	1270	1270	1270	1260	1280	1300	1310	1330	1400	1450	1460	1420	1370	1310	-	-
2	1/2	1810	1660	1660	1660	1660	1650	1650	1650	1640	1640	1600	1550	1500	1420	1320	-	-	-
3	1/2	1840	1700	1700	1690	1690	1680	1670	1670	1650	1640	1580	1500	1420	1330	1280	-	-	-
4	1/2	1680	1560	1550	1550	1540	1540	1530	1520	1510	1480	1420	1340	1280	1210	-	-	-	-
5	1/2	1460	1300	1300	1300	1300	1300	1300	1290	1290	1290	1220	-	-	-	-	-	-	-
1	1	1460	1340	1340	1350	1350	1340	1360	1390	1420	1450	1550	1620	1670	1670	1650	1610	-	-
2	1	1930	1790	1790	1790	1790	1790	1800	1800	1790	1790	1780	1770	1740	1710	1640	1590	1520	-
3	1	2040	1910	1910	1910	1900	1900	1900	1890	1890	1890	1840	1790	1730	1670	1600	-	-	-
4	1	1990	1860	1850	1850	1840	1840	1840	1840	1830	1820	1810	1750	1690	1620	1570	-	-	-
5	1	1820	1690	1680	1680	1670	1660	1670	1650	1660	1640	1640	1570	1500	1480	-	-	-	-

As a sanity check, it is somewhat useful to compare dyon limits with monopole limits of the same order using the same dataset and analogous search and/or analysis methods. Therefore, comparing the smallest electric charge of the dyon,  $1e$ , with the monopole [108], we find that the mass limits obtained for the dyon are, unsurprisingly, equivalent to or better than those obtained in the monopole search as shown in Table 3.4.

### 3.4.6 Conclusions

In conclusion, we investigated for the first time at an accelerator the direct production of dyon-antidyon pairs via the DY mechanism. A SQUID-based magnetometer was used to scan the aluminium components of the MoEDAL trapping detector exposed to 13TeV  $p - p$  LHC collisions during Run-2 in order to check for the presence of trapped magnetic charge belonging to monopoles and/or dyons. Our scanning process failed to observe any candidates, and cross-section upper limits as low as 30fb were established. As was stated earlier, the trapping condition assumes the dyon to be negatively charged in order that we may be conservative to a reasonable extent. Benchmark DY production model was used to establish mass limits for dyons with magnetic charges up to  $5g_D$ , electric charges between  $1e$  and  $200e$ , and Spin-0, Spin- $\frac{1}{2}$  and Spin-1 dyons in the range of 750GeV to 1910GeV. For magnetic charges in the

---

same range, the equivalent mass limitations for magnetic monopoles are 870GeV to 2040GeV. We point out that numerous earlier searches for HIPs should theoretically also be sensitive to dyons. However, to date and at the time of writing, no explicit search for dyons has ever been made.

# Chapter 4

## Conclusion

*"Every truth has two sides; it is as well to look at both before we commit ourselves to either"* - Aesop

Fundamental concerns like charge quantization and the nature of dark matter are addressed with predictions of particles beyond the scope of the Standard Model, such as magnetic monopoles, highly electrically charged objects (HECOs) and/or dyons.

The presence of monopoles is predicted by a number of theories, beginning with Dirac's theory and extending through to Cho-Maison electroweak models and different GUT models. The electroweak theories anticipate monopoles with masses on the order of several TeV within the LHC range, but the Dirac model offers no predictions for monopole mass.

Diverse methods have been used to look for such exotic particles during the last few decades. The searches discussed in this thesis are merely an addition to the numerous searches that have already been conducted at the LHC using a variety of different techniques to find monopoles that might have been created in the 8 TeV and 13 TeV proton-proton collisions during Run-1 and Run-2 of the Large Hadron Collider (LHC) respectively.

These exotic particles are identified by their strongly ionizing signal in MoEDAL. With its ground-breaking architecture and design, the MoEDAL experiment looks for magnetic monopoles and other highly ionizing particles (HIPs). This essentially passive detector is used for a variety of purposes in the LHCb VELO cavern at Interaction Point-8.

To begin, it locates fresh particle tracks using Nuclear Track Detectors (NTDs). Second, if these exotic particles are captured, the detector's special ability to trap them by usage of the Magnetic Monopole Trapping (MMT) detector will enable detailed study of them.

The NTD and MMT detectors' data from exposure to  $2.209\text{fb}^{-1}$  of 8 TeV proton-proton collisions is provided in this thesis. The data was used to look for any traces of HIPs and the analyses was focused on the search for magnetic monopoles and HECOs. Additionally, a dyon search using just the MMTs during Run-2 of the LHC was presented as well.

This is the first time a trapping array that is both scalable and reusable has been used at an accelerator facility. Both the MMT and NTD detectors had no potential monopole and/or HIP candidates.

By employing both the MMT and NTD detectors, MoEDAL with its limited solid angle coverage and modest luminosity explores charge, mass, and energy ranges that other LHC experiments are unable to access.

The NTD and MMT detection methods combined offer a direct measurement of a monopole magnetic charge based only on its magnetic characteristics, allowing for an unambiguous background-free evaluation of a signal and the ability to make a discovery rapidly. Furthermore, the capture of a monopole in the MMT detector system

would herald a new era in physics.

# Bibliography

- [1] P. A. M. Dirac, “Quantized Singularities in the Electromagnetic Field,” *Proc. Roy. Soc. Lond.*, vol. A, no. 133, p. 60–72, 1931. (Cited on pages [iii](#), [4](#), [6](#), [7](#), [20](#), [70](#), and [103](#).)
- [2] MoEDAL Collaboration, “Search for highly-ionizing particles in pp collisions at the LHC’s Run-1 using the prototype MoEDAL detector,” *Eur.Phys.J.C*, vol. 82, no. 8, 2022. (Cited on page [iv](#).)
- [3] MoEDAL Collaboration, “First Search for Dyons with the Full MoEDAL Trapping Detector in 13 TeV pp Collisions,” *Phys. Rev. Lett.*, vol. 126, no. 071801, 2021. (Cited on page [iv](#).)
- [4] S.Balestra et al., “Bulk etch rate measurements and calibrations of plastic nuclear track detectors,,” *NIM-B*, vol. 254, pp. 254–258, 2007. (Cited on pages [xiv](#), [79](#), [80](#), and [81](#).)
- [5] Pierre Curie, “Sur la possibilite d’existence de la conductibilite magnetique et du magnetisme libre (On the possible existence of magnetic conductivity and free magnetism),” *Seances de la Societe Francaise de Physique (Paris)*, p. 76, 1984. (Cited on page [4](#).)
- [6] J. D. Jackson, “Classical Electrodynamics,” *John Wiley and Sons Inc*, vol. 3rd Edition, 1999. (Cited on page [4](#).)
- [7] Suresh Govindarajan, “Lectures on Classical Field Theory,” vol. 30, 2013. (Cited on pages [5](#) and [6](#).)

- [8] P. A. M. Dirac, “A theory of electrons and protons,” *Proc. Roy. Soc. Lond.*, vol. A, no. 126, p. 361, 1930. (Cited on page 7.)
- [9] J.R. Oppenheimer, “On the Theory of Electrons and Protons,” *Physical Review*, vol. 35, p. 562, 1930. (Cited on page 7.)
- [10] Y. Aharonov and D. Bohm, “Significance of electromagnetic potentials in the quantum theory,” *Phys. Rev.*, no. 115, pp. 485–491, 1959. (Cited on page 9.)
- [11] J. S. Schwinger, “Magnetic charge and quantum field theory,” *Phys. Rev.*, vol. 144, pp. 1087–1093, 1966. (Cited on page 13.)
- [12] J. S. Schwinger, “Sources and magnetic charge,” *Phys. Rev.*, vol. 173, p. 1536–1544, 1968. (Cited on page 13.)
- [13] T. Vachaspati and M. Barriola, “A New class of defects,” *Phys. Rev. Lett.*, vol. 69, pp. 1867–1870, 1992. (Cited on page 15.)
- [14] M. Barriola and T. Vachaspati and M. Bucher, “Embedded defects,” *Phys. Rev.*, vol. D, no. 50, pp. 2819–2825, 1994. (Cited on page 15.)
- [15] Y. M. Cho and D. Maison, “Monopoles in Weinberg-Salam model,” *Phys. Lett.*, vol. B, no. 391, pp. 360–365, 1997. (Cited on pages 15, 21, 24, and 71.)
- [16] Y. M. Cho and K. Kimm and J. H. Yoon, “Mass of the Electroweak Monopole,” *Mod. Phys. Lett.*, vol. A, no. 31, 2016. (Cited on pages 15 and 71.)
- [17] J. Ellis and N. E. Mavromatos and T. You, “The Price of an Electroweak Monopole,” *Phys. Lett.*, vol. B, no. 756, pp. 29–35, 2016. (Cited on pages 15, 28, and 71.)
- [18] P. Q. Hung, “A model of electroweak-scale right-handed neutrino mass,” *Phys. Lett. B*, vol. 649, pp. 275–279, 2007. (Cited on page 15.)
- [19] P.Q.Hung, “Topologically stable, finite energy electroweak-scale monopoles,” *Nucl. Phys. B*, vol. 962, no. 115278, 2021. (Cited on pages 15, 28, 71, and 73.)

- [20] H. Georgi and S. Glashow, “S. Unity of all elementary particle forces.,” *Phys. Rev. Lett*, vol. 32, pp. 438–441, 1974. (Cited on pages 16 and 70.)
- [21] J. Ellis and P. Q. Hung and N. Mavromatos, “An Electroweak Monopole, Dirac Quantization and the Weak Mixing Angle,” *Nuclear Physics B*, vol. 969, no. 115468, 2021. (Cited on pages 18, 19, 28, 71, and 73.)
- [22] H.B.Nielsen and P.Olesen, “Vortex-line Models for Dual Strings,” *Nuclear Physics B*, vol. 61, pp. 45–61, 1973. (Cited on page 26.)
- [23] Yoichiro Nambu, “String-Like Configurations in the Weinberg-Salam Theory,” *Nuclear Physics B*, vol. 130, p. 505, 1977. (Cited on page 26.)
- [24] G. ’t Hooft, “Magnetic Monopoles in Unified Gauge Theories,” *Nucl. Phys.*, vol. B, no. 79, pp. 276–284, 1974. (Cited on pages 26, 38, and 70.)
- [25] A. M. Polyakov, “Particle Spectrum in the Quantum Field Theory,,” *JETP Lett.*, vol. 20, pp. 194–195, 1974. (Cited on pages 26, 38, and 70.)
- [26] B.Julia, A.Zee, “Poles with both magnetic and electric charges in non-Abelian gauge theory,” *Physical Review D*, vol. 11, no. 8, 1975. (Cited on page 28.)
- [27] S. Burdin and A. Firan and and W. Taylor, “A Search for Magnetic Monopoles at ATLAS,” 2012. (Cited on page 29.)
- [28] ATLAS Collaboration, “Search for Magnetic Monopoles using the ATLAS Detector,” 2010. (Cited on page 29.)
- [29] Y. Kazama and C. N. Yang and A. S. Goldhaber, “Scattering of a Dirac particle with charge  $Ze$  by a fixed magnetic monopole,” *Phys. Rev.*, vol. D, no. 15, pp. 2287–2299, 1977. (Cited on page 31.)
- [30] S. P. Ahlen, “Stopping-power formula for magnetic monopoles,” *Phys. Rev.*, vol. D, no. 17, pp. 229–233, 1978. (Cited on pages 31, 65, and 114.)

- [31] MoEDAL Collaboration, “Search for magnetic monopoles with the MoEDAL prototype trapping detector in 8 TeV proton-proton collisions at the LHC,” *JHEP*, vol. 8, 2016. (Cited on pages 33 and 35.)
- [32] K. Kinoshita et al., “Search for Highly Ionizing Particles in  $e^+e^-$  annihilations at  $\sqrt{s} = 91.1\text{GeV}$ ,” *Phys. Rev.*, vol. D, no. 46, pp. R881–R884, 1992. (Cited on page 33.)
- [33] SLIM Collaboration, “Search for ‘light’ magnetic monopoles,” (Cited on pages 33 and 41.)
- [34] P. B. Price and E. K. Shirk and W. Z. Osborne and L. S. Pinsky, “Further measurements and reassessment of the magnetic-monopole candidate,” *Phys. Rev.*, vol. D, no. 18, pp. 1382–1421, 1978. (Cited on pages 33 and 36.)
- [35] MACRO Collaboration, “Final results of magnetic monopole searches with the MACRO experiment,” *Eur. Phys. J.*, vol. C, no. 25, pp. 511–522, 2002. (Cited on pages 33, 36, 39, and 86.)
- [36] SLIM Collaboration, “Magnetic Monopole Search at high altitude with the SLIM experiment,” *Eur. Phys. J.*, vol. C, no. 55, pp. 57–63, 2008. (Cited on pages 33, 41, and 86.)
- [37] K. A. Milton, “Theoretical and experimental status of magnetic monopoles,” *Rept. Prog. Phys.*, vol. 69, pp. 1637–1712, 2006. (Cited on pages 34 and 54.)
- [38] A. Roeck and A. Katre and P. Mermoud and D. Milstead and T. Sloan, “Sensitivity of LHC experiments to exotic highly ionising particles,” *The European Physical Journal*, vol. C, no. 72, pp. 1–18, 2012. (Cited on page 34.)
- [39] (Cited on pages 34 and 42.)
- [40] H. H. Kolm and F. Villa and A. Odian, “Search for magnetic monopoles,” *Phys. Rev.*, vol. D, no. 4, p. 1285, 1971. (Cited on pages 34 and 42.)

- [41] R. L. Fleischer et al., “Search for magnetic monopoles in deep ocean deposits,” *Phys. Rev.*, vol. 184, pp. 1393–1397, 1969. (Cited on pages 34 and 42.)
- [42] R. L. Fleischer and I. S. Jacobs and W. M. Schwarz and P. B. Price and H. G. Goodell, “Search for multiply charged dirac magnetic poles,” *Phys. Rev.*, vol. 177, pp. 2029–2035, 1969. (Cited on pages 34 and 42.)
- [43] R. A. Carrigan and F. A. Nezrick and B. P. Strauss, “Search for misplaced magnetic monopoles,” *Phys. Rev.*, vol. D, no. 13, pp. 1823–1825, 1976. (Cited on page 34.)
- [44] V. A. Petukhov and M. N. Yakimenko, “Search for the Dirac Monopole,” *Nucl. Phys.*, vol. 49, p. 87, 1963. (Cited on page 34.)
- [45] S. Burdin et al., “Non-collider searches for stable massive particles,” *Phys. Rept.*, vol. 582, pp. 1–52, 2015. (Cited on pages 34, 42, 69, and 103.)
- [46] P. B. Price and E. K. Shirk and W. Z. Osborne and L.S. Pinsky, “Evidence for Detection of a Moving Magnetic Monopole,” *Phys. Rev. Lett.*, vol. 35, pp. 487–490, 1975. (Cited on page 36.)
- [47] S. N. Anderson and J. J. Lord and S. C. Strausz and R. J. Wilkes, “Possible evidence for magnetic monopole interactions: Anomalous long range alpha particle tracks deep underground,” *Phys. Rev.*, vol. D, no. 28, 1983. (Cited on page 36.)
- [48] A. D. Caplin and M. Hardiman and M. Koratzinos and J. C. Schouten, “Observation of an Unexplained Event From a Magnetic Monopole Detector,” *Nature*, vol. 321, pp. 402–406, 1986. (Cited on page 37.)
- [49] J. Preskill, “Magnetic monopoles,” *Ann. Rev. Nucl. Part. Sci.*, vol. 34, pp. 461–530, 1984. (Cited on page 38.)
- [50] E.N.Parker, “The Origin of Magnetic Fields,” *Astrophys. J.*, vol. 160, p. 383, 1970. (Cited on page 38.)

- [51] MACRO Collaboration, “The MACRO detector at Gran Sasso,” *Nucl. Instrum. Meth.*, vol. A, no. 486, pp. 663–707, 2002. (Cited on page 39.)
- [52] S. D. Wick and T. W. Kephart and T. J. Weiler and P.L. Biermann, “Signatures for a cosmic flux of magnetic monopoles,” *Astropart. Phys.*, vol. 18, 2003. (Cited on page 40.)
- [53] M. Detrixhe et. al, “Ultrarelativistic magnetic monopole search with the ANITA-II balloon-borne radio interferometer,” *Phys. Rev.*, vol. D, no. 83, 2011. (Cited on page 40.)
- [54] ANTARES Collaboration, “ANTARES: the first undersea neutrino telescope,” *Nucl. Instrum. Meth.*, vol. A, no. 656, pp. 11–38, 2011. (Cited on page 40.)
- [55] ANTARES Collaboration, “Search for Relativistic Magnetic Monopoles with the ANTARES Neutrino Telescope,” *Astropart. Phys.*, vol. 35, pp. 634–640, 2012. (Cited on page 40.)
- [56] IceCube Collaboration, “First Year Performance of The IceCube Neutrino Telescope,” *Astropart. Phys.*, vol. 26, pp. 155–173, 2006. (Cited on page 41.)
- [57] Super-Kamiokande Collaboration, “Search for GUT monopoles at Super-Kamiokande,” *Astropart. Phys.*, vol. 36, pp. 131–136, 2012. (Cited on page 41.)
- [58] D. F. Bartlett and D. Soo and R. L. Fleischer and H. R. Hart, Jr. and A. Mogro-Campero, “Search for Cosmic Ray Related Magnetic Monopoles at Ground Level,” *Phys. Rev.*, vol. D, no. 24, p. 612, 1981. (Cited on page 42.)
- [59] P. H. Eberhard and R. R. Ross and L. W. Alvarez and R. D. Watt, “Search for magnetic monopoles in lunar material,” *Phys. Rev.*, vol. D, no. 4, p. 3260, 1971. (Cited on page 43.)

- [60] R. R. Ross and P. H. Eberhard and L. W. Alvarez and R. D. Watt, “Search for magnetic monopoles in lunar material using an electromagnetic detector,” *Phys. Rev.*, vol. D, no. 8, p. 698, 1973. (Cited on page 43.)
- [61] L3 Collaboration, “Search for anomalous  $Z \rightarrow \gamma \gamma \gamma$  events at LEP,” *Phys. Lett.*, vol. B, no. 345, pp. 609–615, 1995. (Cited on page 44.)
- [62] D0 Collaboration, “A Search for heavy point - like Dirac monopoles,” *Phys. Rev. Lett.*, vol. 81, pp. 524–529, 1998. (Cited on page 44.)
- [63] I. F. Ginzburg and S. L. Panfil, “The Possibility of Observation of Heavy Dirac-schwinger Magnetic Pole,” *Sov. J. Nucl. Phys.*, vol. 36, p. 850, 1982. (Cited on page 44.)
- [64] A. De Rujula, “Effects of virtual monopoles,” *Nucl. Phys.*, vol. B, no. 435, pp. 257–276, 1995. (Cited on page 44.)
- [65] J. L. Pinfold et al., “Search for highly ionizing particles produced at the OPAL intersection point at LEP,” *Phys. Lett.*, vol. B, no. 316, pp. 407–411, 1993. (Cited on page 45.)
- [66] H1 Collaboration, “A Direct search for stable magnetic monopoles produced in positron-proton collisions at HERA,” *Eur. Phys. J.*, vol. C, no. 41, pp. 133–141, 2005. (Cited on page 45.)
- [67] G. R. Kalbfeisch and W. Luo and K. A. Milton and E. H. Smith and M. G. Strauss, “Limits on production of magnetic monopoles utilizing samples from the D0 and CDF detectors at the Tevatron,” *Phys. Rev.*, vol. D, no. 69, 2004. (Cited on page 46.)
- [68] CDF Collaboration, “Direct search for Dirac magnetic monopoles in  $p\bar{p}$  collisions at  $\sqrt{s} = 1.96\text{TeV}$ ,” *Phys. Rev. Lett.*, vol. 96, 2006. (Cited on page 46.)

- [69] ATLAS Collaboration, “Search for magnetic monopoles in  $\sqrt{s} = 7\text{TeV}$  pp collisions with the ATLAS detector,” *Phys. Rev. Lett.*, vol. 109, 2012. (Cited on pages 46, 69, 72, 103, 106, and 108.)
- [70] L. Evans and P. Bryant, “LHC Machine,” *Journal of Instrumentation*, vol. 3, 2008. (Cited on pages 47, 48, and 49.)
- [71] MoEDAL Collaboration, “Technical Design Report of the MoEDAL Experiment,” *CERN LHCC*, p. 76, 2009. (Cited on pages 50, 51, 52, and 69.)
- [72] MoEDAL Collaboration, “The Physics Programme Of The MoEDAL Experiment At The LHC,” *Int. J. Mod. Phys.*, vol. A, no. 29, 2014. (Cited on pages 51, 52, 56, 69, and 71.)
- [73] MoEDAL Collaboration, “MoEDAL: Seeking magnetic monopoles and more at the LHC,” *PoS EPS-HEP 2015*, 2015. (Cited on pages 51 and 52.)
- [74] L.P. Gamberg and G.R. Kalbfleisch and K.A. Milton, “Direct and indirect searches for low mass magnetic monopoles,” *Found. Phys. Private communication from Kimball A. Milton, January 26th 2021.*, vol. 30, no. 543, 2000. (Cited on page 55.)
- [75] C.J. Goebel, “Binding of nuclei to monopoles, in Monopole ’83,” *J.L. Stone ed., Plenum*, p. 333, 1984. (Cited on pages 55, 76, and 108.)
- [76] L. Bracci and G. Fiorentini, “Interactions of Magnetic Monopoles With Nuclei and Atoms,” *Nucl. Phys. B*, vol. 232, no. 236, 1984. (Cited on pages 55, 76, and 108.)
- [77] K. Olausen and R. Sollie, “Form-factor effects on nucleus-magnetic monopole binding,” *Nucl.Phys.B*, vol. 255, no. 465, 1985. (Cited on pages 55 and 108.)
- [78] J. L. Pinfold, “The MoEDAL Experiment at the LHC – a New Light on the Terascale Frontier,” *J. Phys. Conf. Ser.*, vol. 631, 2015. (Cited on pages 56 and 108.)

- [79] A. De Roeck et al., “Development of a magnetometer-based search strategy for stopped monopoles at the Large Hadron Collider,” *The European Physical Journal*, vol. C, no. 72, pp. 1–9, 2012. (Cited on pages 59, 63, and 77.)
- [80] H. S. C. Chen, “Note on the Magnetic Pole,” *American Journal of Physics*, vol. 33, pp. 563–565, 1965. (Cited on page 59.)
- [81] MoEDAL Collaboration, “Search for magnetic monopoles with the MoEDAL forward trapping detector in 13 TeV proton-proton collisions at the LHC ,” *Phys. Rev. Lett.*, vol. 118, no. 061801 arXiv:1611.06817 [hep-ex], 2017. (Cited on page 61.)
- [82] GEANT4 Collaboration, “GEANT4 physics lists,” 2014. (Cited on page 64.)
- [83] GEANT4 Collaboration, “<http://geant4.cern.ch/support/>,” (Cited on page 64.)
- [84] GEANT4 Collaboration, “GEANT4 developments and applications,” *IEEE Trans. Nucl. Sci.*, vol. 53, p. 270, 2006. (Cited on pages 64 and 114.)
- [85] GEANT4 Collaboration, “GEANT4: A Simulation toolkit,” *Nucl.Instrum.Meth.*, vol. A, no. 506, pp. 250–303, 2003. (Cited on page 64.)
- [86] LHCb Collaboration, “The Gauss Project,” (Cited on page 64.)
- [87] Ameir Shaa, “Complete guide to installing MoEDAL Simulation using CERNVM SL6 v1.1,” 2017. (Cited on page 64.)
- [88] T. Whyntie, “MoEDAL Grid User Guide,” 2016. (Cited on page 64.)
- [89] T. Whyntie, “The GridPP UserGuide,” 2016. (Cited on page 64.)
- [90] J.Alwall et al., “The automated computation of tree-level and next-to-leading order differential cross sections, and their matching to parton shower simulations,” *Journal of High Energy Physics*, pp. 1–157, 2014. (Cited on pages 64 and 106.)

- [91] M. L. Mangano and F. Piccinini and A. D. Polosa and M. Moretti and R. Pittau, “ALPGEN, a generator for hard multiparton processes in hadronic collisions,” *Journal of High Energy Physics*, 2003. (Cited on page 65.)
- [92] B. P. Kersevan and E. Richter-Was, “The Monte Carlo event generator AcerMC versions 2.0 to 3.8 with interfaces to PYTHIA 6.4, HERWIG 6.5 and ARIADNE 4.1,” *Comput. Phys. Commun.*, vol. 184, 2013. (Cited on page 65.)
- [93] T. Sjostrand and S. Mrenna and P. Z. Skands, “A Brief Introduction to PYTHIA 8.1,” *Comput. Phys. Commun.*, vol. 178, pp. 852–867, 2008. (Cited on page 65.)
- [94] M. Bahr et al., “Herwig++ Physics and Manual,” *Eur. Phys. J.*, vol. C, no. 58, 2008. (Cited on page 65.)
- [95] T. Gleisberg et al., “Event generation with SHERPA 1.1,” *JHEP*, vol. 2, 2009. (Cited on page 65.)
- [96] J. Derkaoui et al., “Energy losses of magnetic monopoles and of dyons in the earth,” *Astropart. Phys.*, vol. 9, pp. 173–183, 1998. (Cited on page 65.)
- [97] S. P. Ahlen and K. Kinoshita, “Calculation of the stopping power of very low velocity magnetic monopoles,” *Phys. Rev.*, vol. D, no. 26, pp. 2347–2363, 1982. (Cited on pages 65 and 114.)
- [98] N. S. Craigie and G. Giacomelli and W. Nahm and Q. Shafi, “Theory and detection of magnetic monopoles in gauge theories,” *Singapore, Singapore: World Scientific*, 1986. (Cited on page 65.)
- [99] L. Patrizii et al., “Energy Losses of Magnetic Monopoles in Aluminum, Iron and Copper,” *arXiv*, 2016. (Cited on page 66.)
- [100] M. Fairbairn et al., “Stable Massive Particles at Colliders,” *Phys. Rept.*, vol. 438, pp. 1–63, 2007. (Cited on pages 69 and 106.)
- [101] L. Patrizii and M. Spurio, “Status of Searches for Magnetic Monopoles,” *Ann. Rev. Nucl. Part. Sci.*, vol. 65, no. 279, 2015. (Cited on pages 69, 86, and 103.)

- [102] ATLAS Collaboration, “Search for Massive Long-Lived Highly Ionising Particles with the ATLAS Detector at the LHC,” *Phys. Lett. B*, vol. 698, 2011. (Cited on pages 69, 72, and 106.)
- [103] ATLAS Collaboration, “Search for long-lived, multi-charged particles in pp collisions at  $\sqrt{s} = 7\text{TeV}$  using the ATLAS detector,” *Phys. Lett. B*, vol. 722, no. 305, 2013. (Cited on pages 69 and 72.)
- [104] ATLAS Collaboration, “Search for magnetic monopoles and stable particles with high electric charges in  $\sqrt{s} = 8\text{TeV}$  pp collisions with the ATLAS detector,” *Phys. Rev. D*, vol. 93, no. 052009, 2016. (Cited on pages 69, 72, 103, 106, and 108.)
- [105] MoEDAL Collaboration, “Search for magnetic monopoles with the MoEDAL prototype trapping detector in 8 TeV proton-proton collisions at the LHC,” *JHEP*, vol. 08, no. 067, 2016. (Cited on pages 69, 72, 87, 97, 98, 101, 103, 106, 108, 111, 114, and 115.)
- [106] MoEDAL Collaboration, “Search for magnetic monopoles with the MoEDAL forward trapping detector in 13 TeV proton-proton collisions at the LHC,” *Phys. Rev. Lett.*, vol. 118, no. 061801, 2017. (Cited on pages 69, 72, 87, 103, 106, 108, and 114.)
- [107] MoEDAL Collaboration, “Search for magnetic monopoles with the MoEDAL forward trapping detector in  $2.11\text{ fb}^{-1}$  of 13 TeV proton-proton collisions at the LHC,” *Phys. Lett. B*, vol. 782, no. 510, 2018. (Cited on pages 69, 72, 87, 103, 106, 108, 110, and 114.)
- [108] MoEDAL Collaboration, “Magnetic Monopole Search with the Full MoEDAL Trapping Detector in 13 TeV pp Collisions Interpreted in Photon-Fusion and Drell-Yan Production,” *Phys.Rev.Lett.*, vol. 123, no. 021802, 2019. (Cited on pages 69, 72, 101, 103, 106, 108, and 127.)

- [109] ATLAS Collaboration, “Search for heavy long-lived, multi-charged particles in pp collisions at  $\sqrt{s} = 8TeV$  using the ATLAS detector,” *Eur. Phys. J. C*, vol. 75, no. 362, 2015. (Cited on pages 69 and 72.)
- [110] CMS Collaboration, “Search for long-lived, charged particles in pp collisions at  $\sqrt{s} = 7TeV$  and  $8TeV$  using the ATLAS detector,” *JHEP*, vol. 07, no. 122, 2013. (Cited on pages 69 and 72.)
- [111] ATLAS Collaboration, “Search for heavy long-lived, multi-charged particles in proton-proton collisions at  $\sqrt{s} = 13TeV$  using the ATLAS detector,” *Phys. Rev. D*, vol. 99, no. 052003, 2018. (Cited on pages 69 and 72.)
- [112] The ATLAS Collaboration, “Search for Magnetic Monopoles and Stable High-Electric Charged Objects in 13 TeV Proton-Proton Collisions with the ATLAS Detector,” *Phys. Rev. Lett.*, vol. 124, no. 031802, 2020. (Cited on pages 69, 72, 98, 101, 103, 106, and 108.)
- [113] N. E. Mavromatos and V. A. Mitsou, “Magnetic monopoles revisited: Models and searches at colliders and in the Cosmos,” *Int. J. Mod. Phys.*, vol. A35, no. 23, 2020. (Cited on pages 69 and 103.)
- [114] L. Patrizzii and Z. Sahnoun and V. Togo, “Searches for cosmic magnetic monopoles: past, present and future,” *Phil. Trans. R. Soc. A*, vol. 377, no. 20180328, 2019. (Cited on page 69.)
- [115] D.Felea et al., “Prospects for discovering supersymmetric long-lived particles with MoEDAL,” *Eur. Phys. J. C*, vol. 80, no. 5, p. 572, 2020. (Cited on page 69.)
- [116] The MoEDAL Collaboration, “Prospects of searches for long-lived charged particles with MoEDAL,” *Eur. Phys. J. C.*, vol. 80, no. 6, p. 572, 2020. (Cited on page 69.)
- [117] W.S. Bae and Y.M. Cho., “Finite Energy Electroweak Dyon,” *JKPS46*, vol. 791, 2002. (Cited on page 71.)

- [118] J. S. Schwinger, “A Magnetic Model of Matter,” *Science*, vol. 165, pp. 757–761, 1969. (Cited on pages 71 and 104.)
- [119] M. Hirsch and R. Maselek and K. Sakurai, “Detecting long-lived multi-charged particles in neutrino mass models with MoEDAL,” *Eur. Phys. J. C*, vol. 81, 2021. (Cited on page 71.)
- [120] S. Coleman, “Q-balls,” *Nucl. Phys.*, vol. B262, no. 263, 1985. (Cited on pages 71 and 105.)
- [121] A. Kusenko and M. E. Shaposhnikov, “Supersymmetric Q-balls as Dark Matter,” *Phys. Lett.*, vol. B418, no. 46, 1998. (Cited on pages 71 and 105.)
- [122] B. Holdom and J. Ren, and C. Zhang, “Quark Matter May Not Be Strange,” *Phys. Rev. Lett.*, vol. 120, 2018. (Cited on pages 71 and 105.)
- [123] E. Farhi and R. Jaffe, “Strange Matter,” *Phys. Rev.*, vol. D30, no. 2379, 1984. (Cited on pages 71 and 105.)
- [124] B. Koch and M. Bleicher, and H. Stocker, “Black Holes at the LHC?,” *J. Phys.*, vol. G34, no. S535, 2007. (Cited on pages 71 and 105.)
- [125] The LHCb Collaboration, “Precision luminosity measurements at LHCb,” *JINST*, vol. 9, no. P12005, 2014. (Cited on page 72.)
- [126] W-Y Song and W. Taylor, “Pair production of magnetic monopoles and stable high-electric-charge objects in proton-proton and heavy-ion collisions,” 2021. (Cited on page 72.)
- [127] Kurochkin and I. Satsunkevich and D. Shoukavy and N. Rusakovich and Y. Kulchitsky, “On Production of Magnetic Monopoles via Fusion at High Energy p-p Collisions,” *Mod. Phys. Lett. A*, vol. 21, no. 2873, 2006. (Cited on page 73.)
- [128] Y. Kurochkin, Y. Kulchitsky, I. Satsunkevich, D. Shoukavy, V. Makhnatch, N. Rusakovich, “Modern status of magnetic monopoles,” *Unpublished*, 2007. (Cited on page 73.)

- [129] S. Baines and N. E. Mavromatos and V. A. Mitsou and J. L. Pinfold and A. Santra, “Monopole Production via Photon Fusion and Drell-Yan Processes,” *Eur. Phys. J.*, vol. C78, no. 966, 2018. (Cited on pages 73 and 106.)
- [130] T.D. Lee and C.N. Yang, “Theory of Charged Vector Mesons Interacting with the Electromagnetic Field,” *Phys. Rev.*, vol. 128, no. 885, 1962. (Cited on page 73.)
- [131] E. V Benton and W. D. Nix, “The restricted energy loss criterion for registration of charged particles in plastics,” *NIM*, vol. 67, pp. 343–347, 1969. (Cited on page 74.)
- [132] L.P. Gamberg and G.R. Kalbeisch and K.A. Milton, “Direct and Indirect Searches for Low Mass Magnetic Monopoles,” *Found. Phys.*, vol. 30, no. 543, 2000. (Cited on pages 76 and 108.)
- [133] D. Freedman and P. Diaconis, “On the histogram as a density estimator: L2 theory,” *Probability Theory and Related Fields*, vol. 57, no. 4, pp. 453–476, 1981. (Cited on pages 90 and 116.)
- [134] LHCb Collaboration, “The LHCb Detector at the LHC,” *JINST*, vol. 3, 2008. (Cited on pages 97, 108, and 114.)
- [135] Particle Data Group Collaboration, “Review of Particle Physics,” *Phys. Rev. D*, vol. 98, no. 030001, 2019. (Cited on page 103.)
- [136] J. Goldstone and R. Jackiw and R. Arnowitt and P. Nath, “Gauge Theories and Modern Field Theory,” *MIT*, p. 377, 1976. (Cited on page 104.)
- [137] P. Hasenfratz and D. Ross, “Anomalous Angular Momenta in a Quantized Theory of Monopoles,” *Nucl. Phys.*, vol. B108, no. 462, 1976. (Cited on page 104.)
- [138] E. Tomboulis and G. Woo, “Soliton Quantization in Gauge Theories,” *Nucl. Phys.*, vol. B107, no. 221, 1976. (Cited on page 104.)

- [139] N Christ and A. Guth and E. Weinberg, “Canonical Formalism for Gauge Theories with Application to Monopole Solutions,” *Nucl. Phys.*, vol. B114, no. 61, 1976. (Cited on page 104.)
- [140] E. Witten, “Dyons of Charge  $\frac{e\theta}{2\pi}$ ,” *Phys. Lett.*, vol. 86B, pp. 283–287, 1979. (Cited on page 104.)
- [141] A. Dainese et al., “Report on the Physics at the HL-LHC, and Perspectives for the HE-LHC,” p. 1418, 2019. (Cited on page 105.)
- [142] Y. M. Cho, “Physical Implications of an Electroweak Monopole,” *Phil. Trans. Roy. Soc. Lond.*, vol. A377, no. 2161, 2019. (Cited on page 105.)
- [143] C. Englert and J. Jaeckel, “Getting stuck! Using Monosignatures to Test Highly Ionizing Particles,” *Phys. Lett. B*, vol. 769, no. 513, 2017. (Cited on page 106.)
- [144] NNPDF Collaboration, “Parton Distributions with LHC Data,” *Nucl. Phys.*, vol. B867, no. 244, 2013. (Cited on page 106.)
- [145] L. P. Gamberg and K.A. Milton, “Dual Quantum Electrodynamics: Dyon-Dyon and Charge Monopole Scattering in a High-Energy Approximation,” *Phys. Rev. D*, vol. 61, 2000. (Cited on page 106.)
- [146] L. P. Gamberg and K.A. Milton, “Eikonal Scattering of Monopoles and Dyons in Dual QED,” *hep-ph/0005016*, 2000. (Cited on page 106.)
- [147] S. P. Ahlen, “Theoretical and experimental aspects of the energy loss of relativistic heavily ionizing particles,” *Rev. Mod. Phys.*, vol. 52, pp. 121–173, 1980. (Cited on page 114.)
- [148] S. Cecchini and L. Patrizii and Z. Sahnoun and G. Sirri and V. Togo, “Energy Losses of Magnetic monopoles in Al, Fe and Cu,” *arXiv:1606.01220*, 2016. (Cited on page 114.)
- [149] LHCb Collaboration, “Measurement of the inelastic  $p-p$  cross-section at  $\sqrt{s} = 13\text{TeV}$ ,” *JHEP*, vol. 06, no. 100, 2018. (Cited on page 120.)

# Chapter 5

# Appendices

## 5.1 Full Analysis of LHC Run 1 Data

### 5.1.1 HECO Acceptance Plots

Here are the extra HECO acceptance Plots.

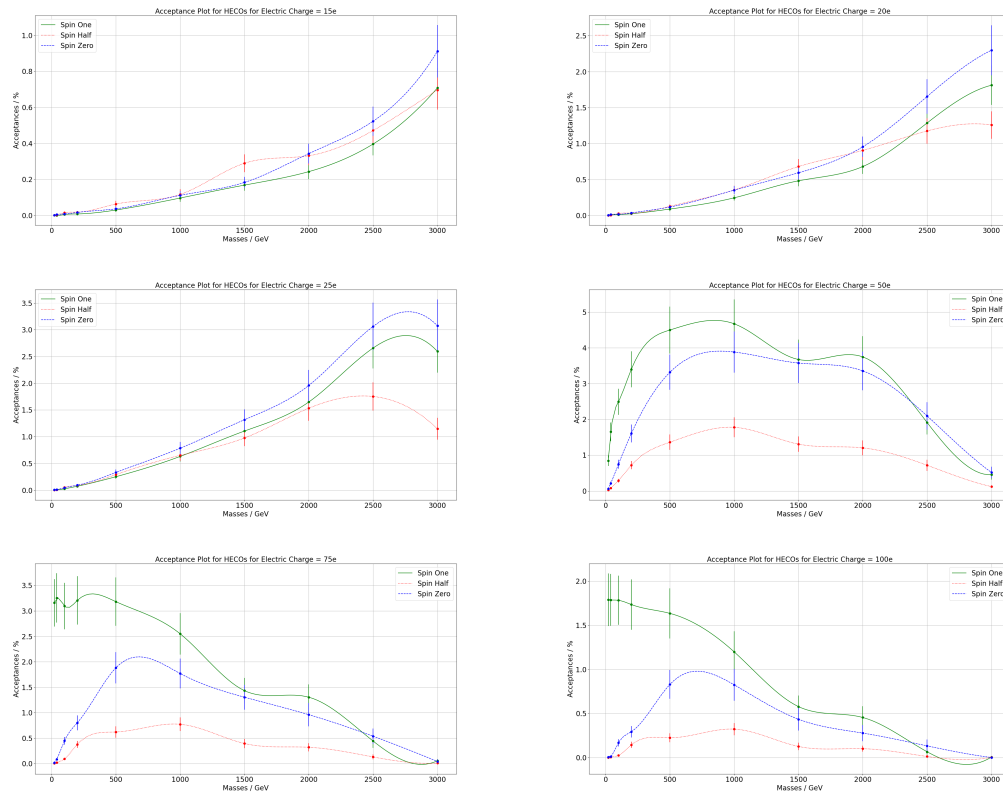


**Figure 5.1:** Run-1 HECO Acceptance Plots for Electric Charges 15e – 100e

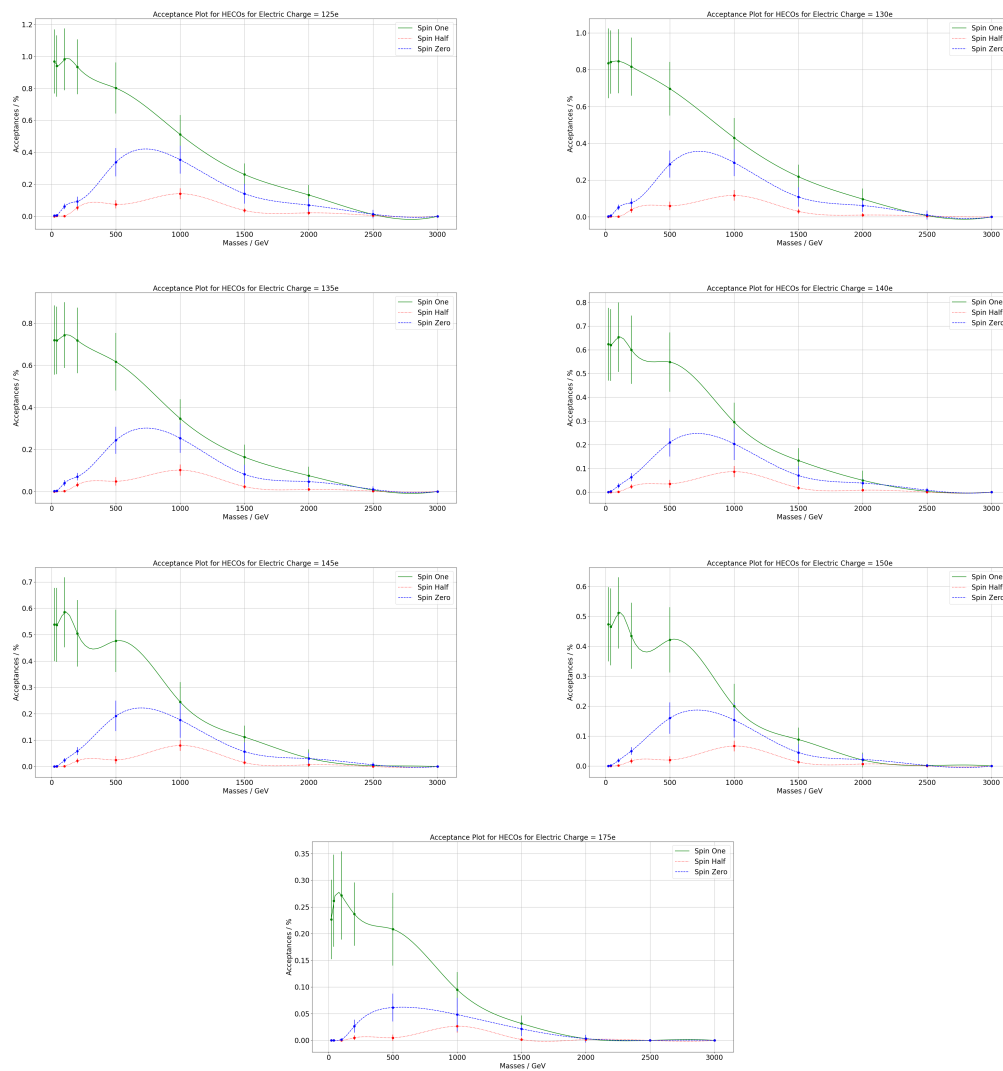


**Figure 5.2:** Run-1 HECO Acceptance Plots for Electric Charges 125e – 175e

## 5.1.2 Monopole Acceptance Plots

Here are the extra monopole acceptance Plots.

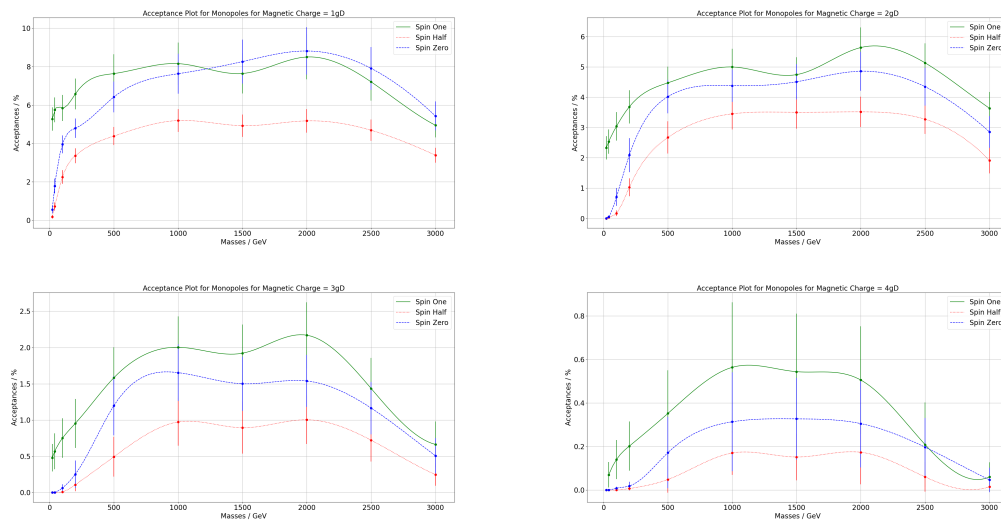


**Figure 5.3:** Run-1 Monopole Acceptance Plots for Magnetic Charges  $1g_D - 4g_D$

## 5.2 The Search for Dyons

### 5.2.1 Dyon Acceptance Plots

Here are the extra Dyon acceptance Plots.

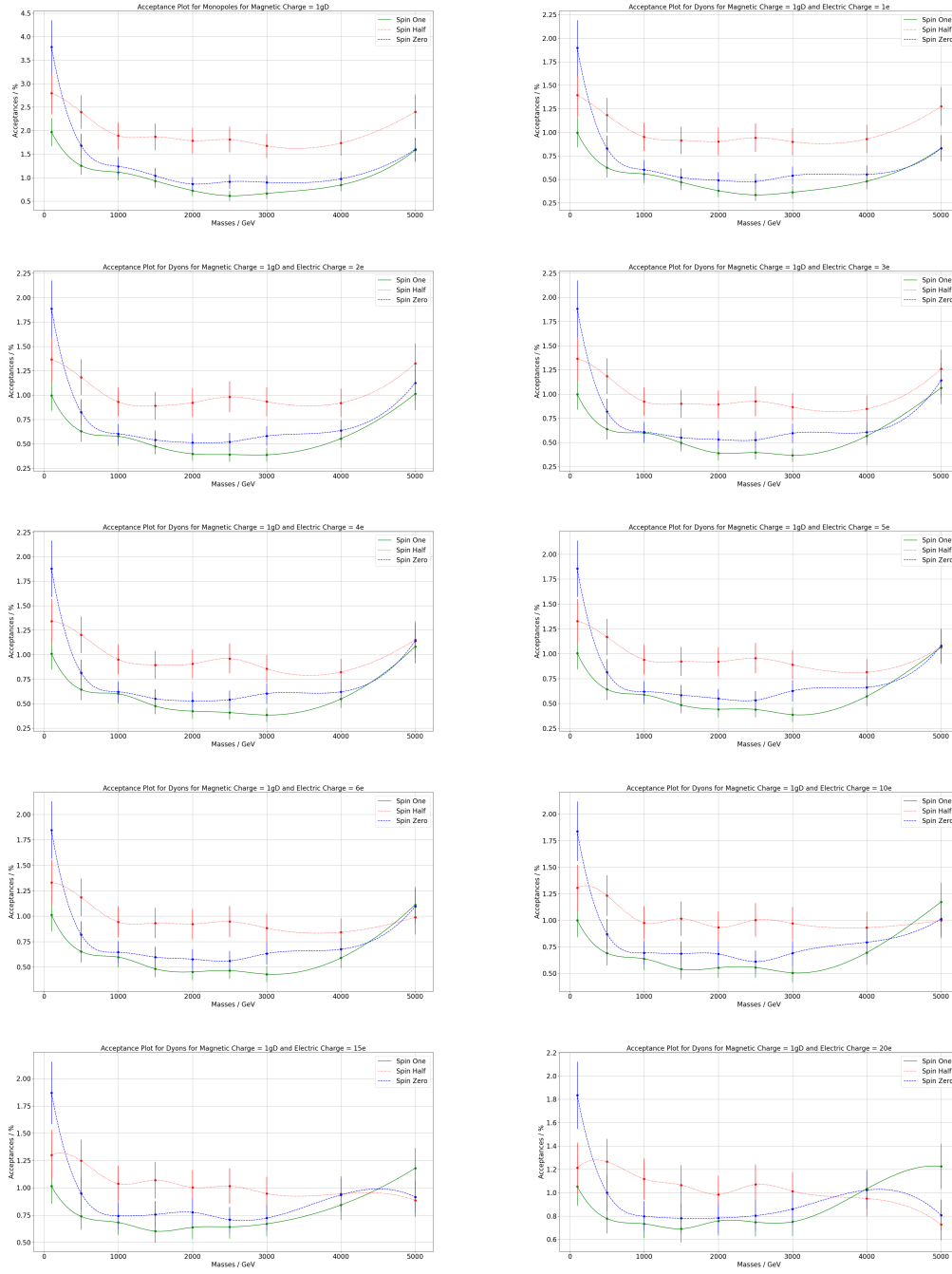


**Figure 5.4:** Run-2 Dyon Acceptance Plots for Magnetic Charge  $1g_D$  and Electric Charges  $0e - 20e$

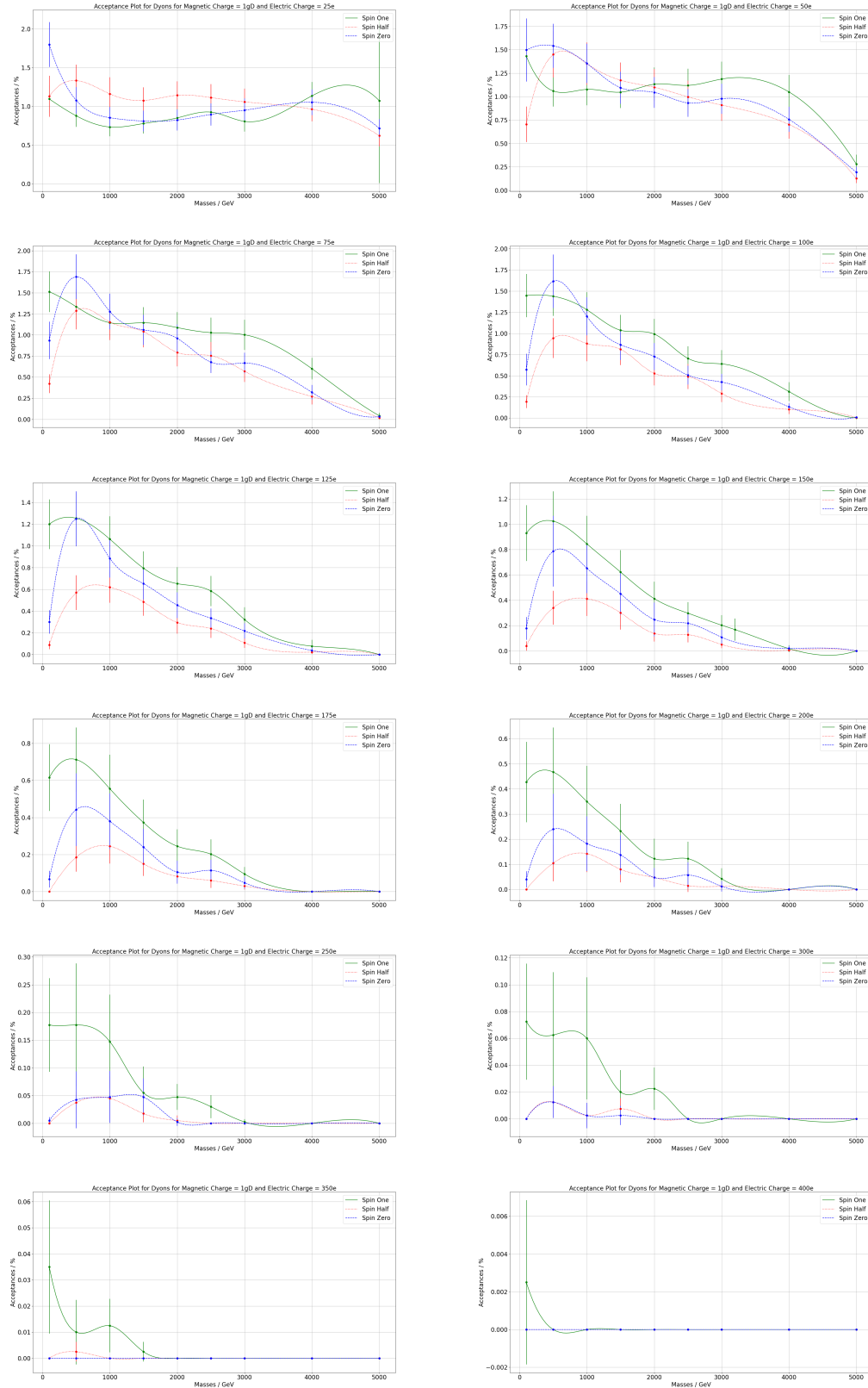
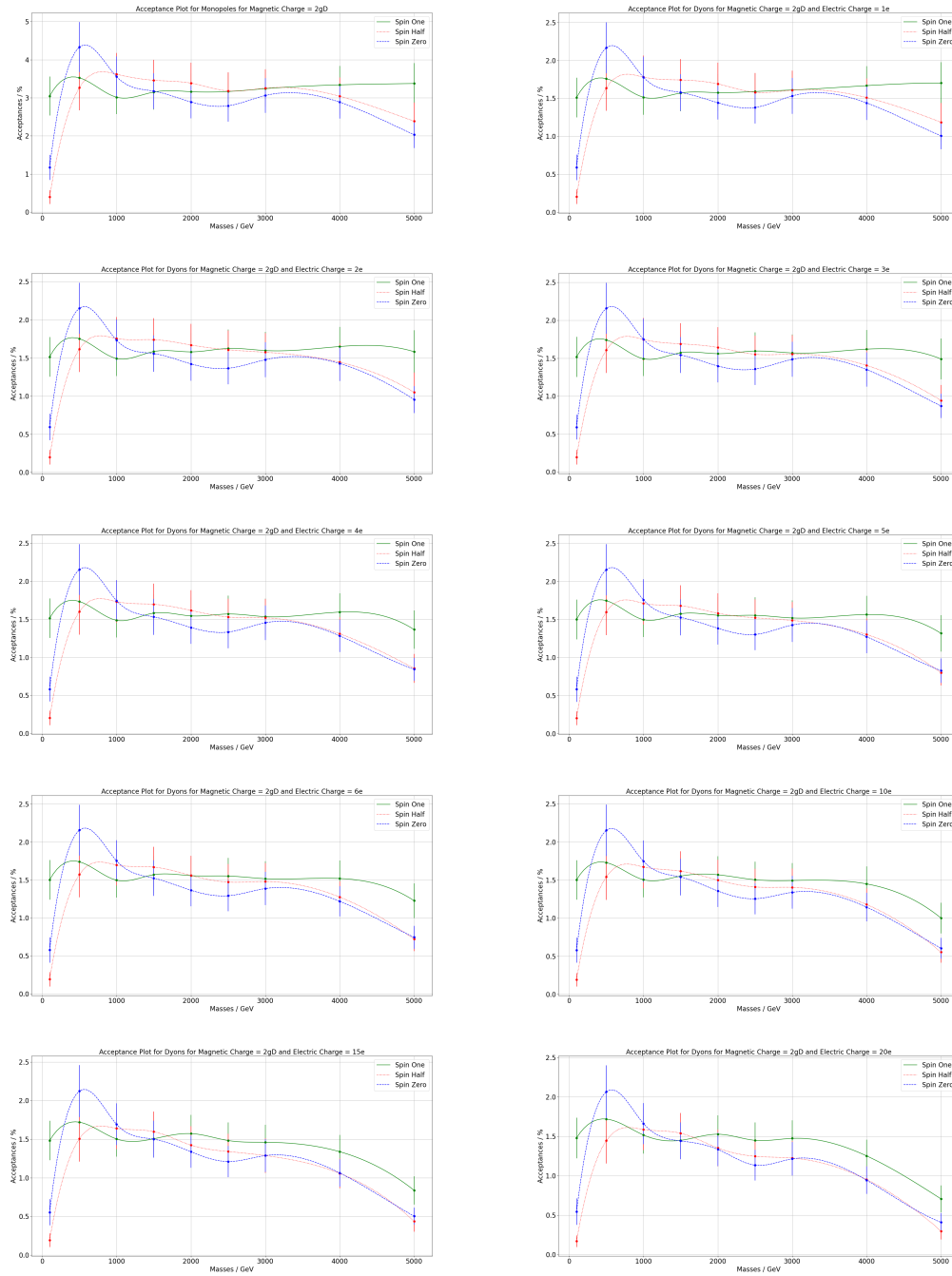
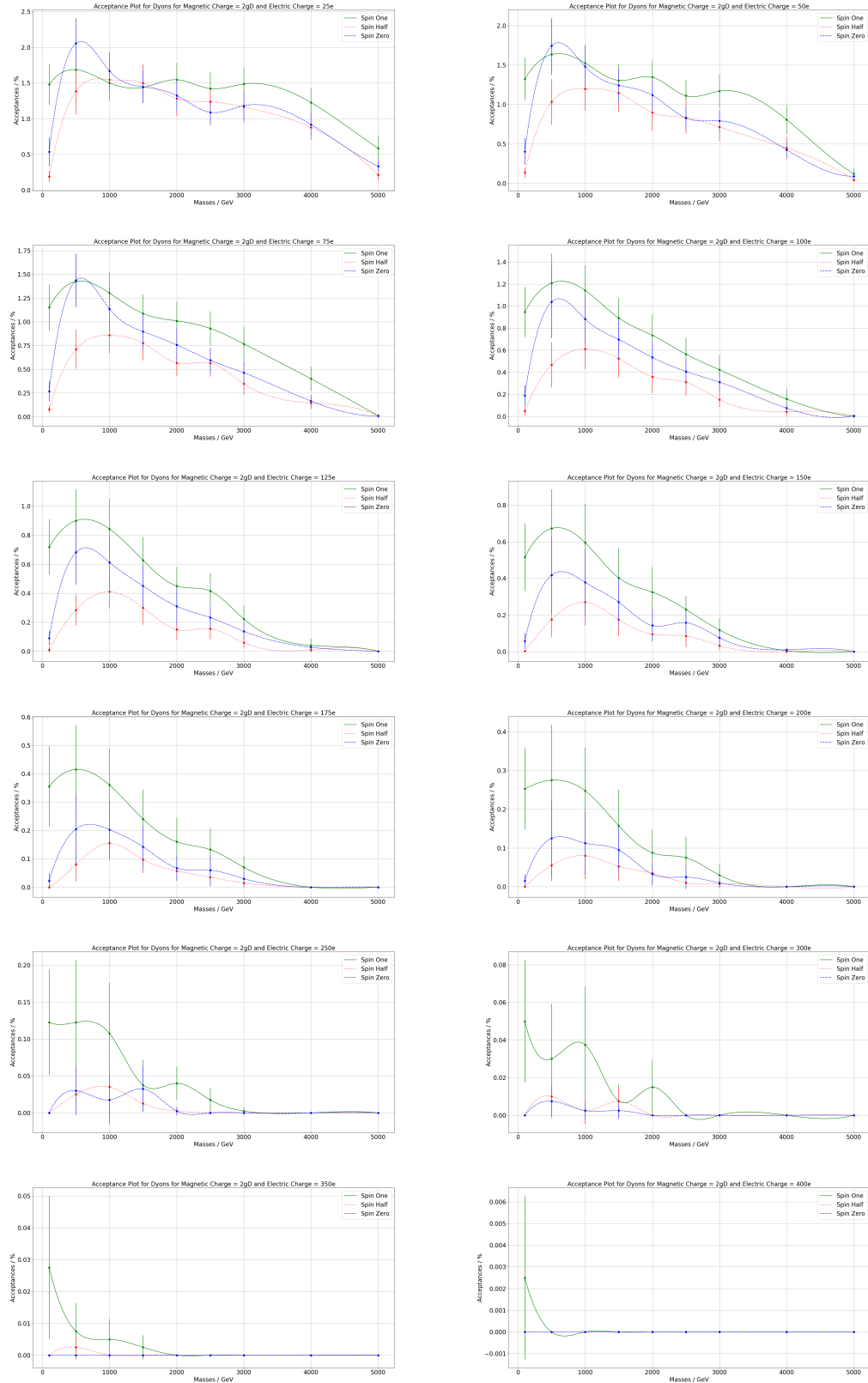


Figure 5.5: Run-2 Dyon Acceptance Plots for Magnetic Charge  $1g_D$  and Electric Charges  $25e - 400e$



**Figure 5.6:** Run-2 Dyon Acceptance Plots for Magnetic Charge  $2g_D$  and Electric Charges  $0e - 20e$



**Figure 5.7:** Run-2 Dyon Acceptance Plots for Magnetic Charge  $2g_D$  and Electric Charges  $25e - 400e$

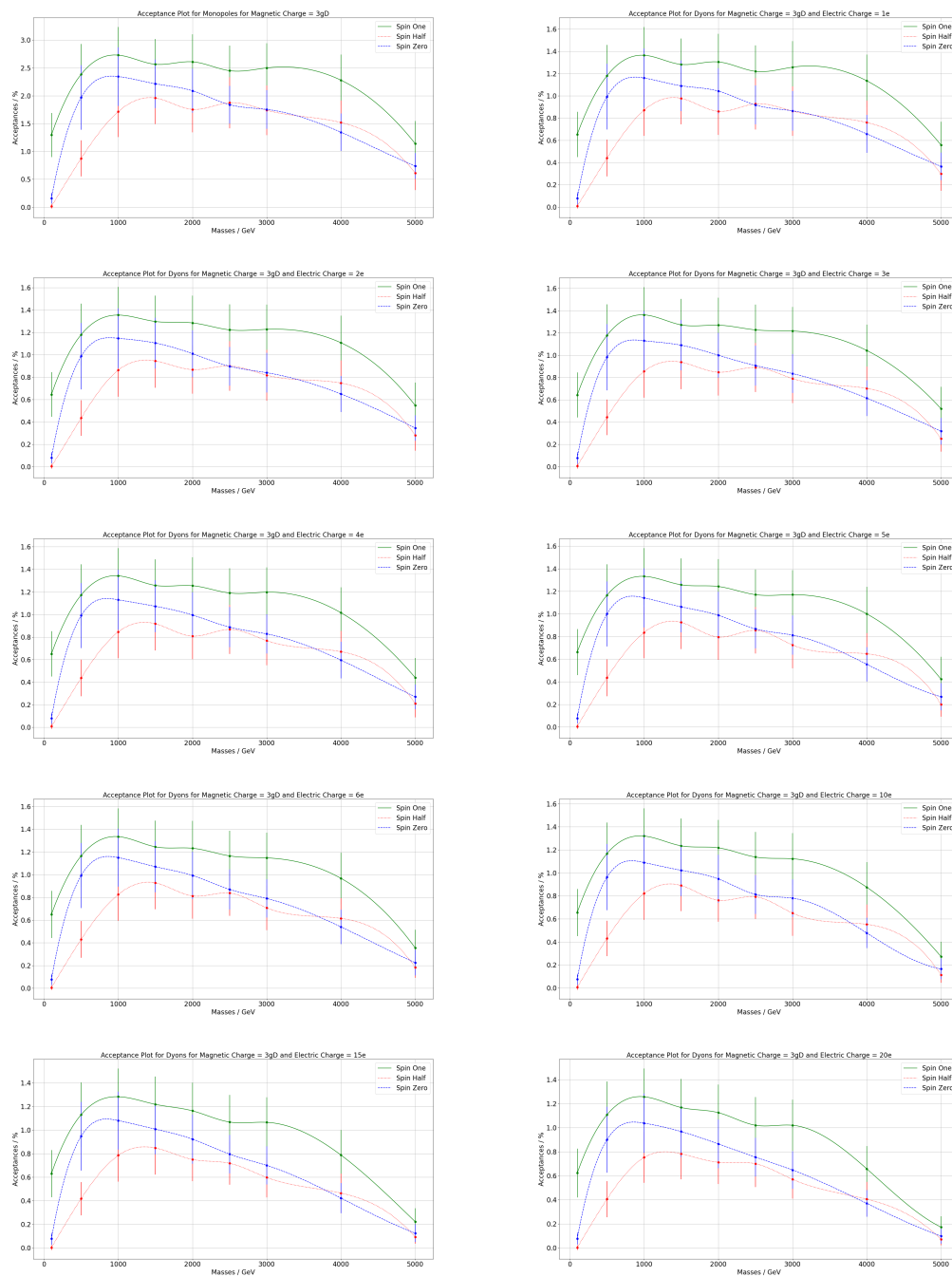


**Figure 5.8:** Run-2 Dyon Acceptance Plots for Magnetic Charge  $3g_D$  and Electric Charges  $0e - 20e$

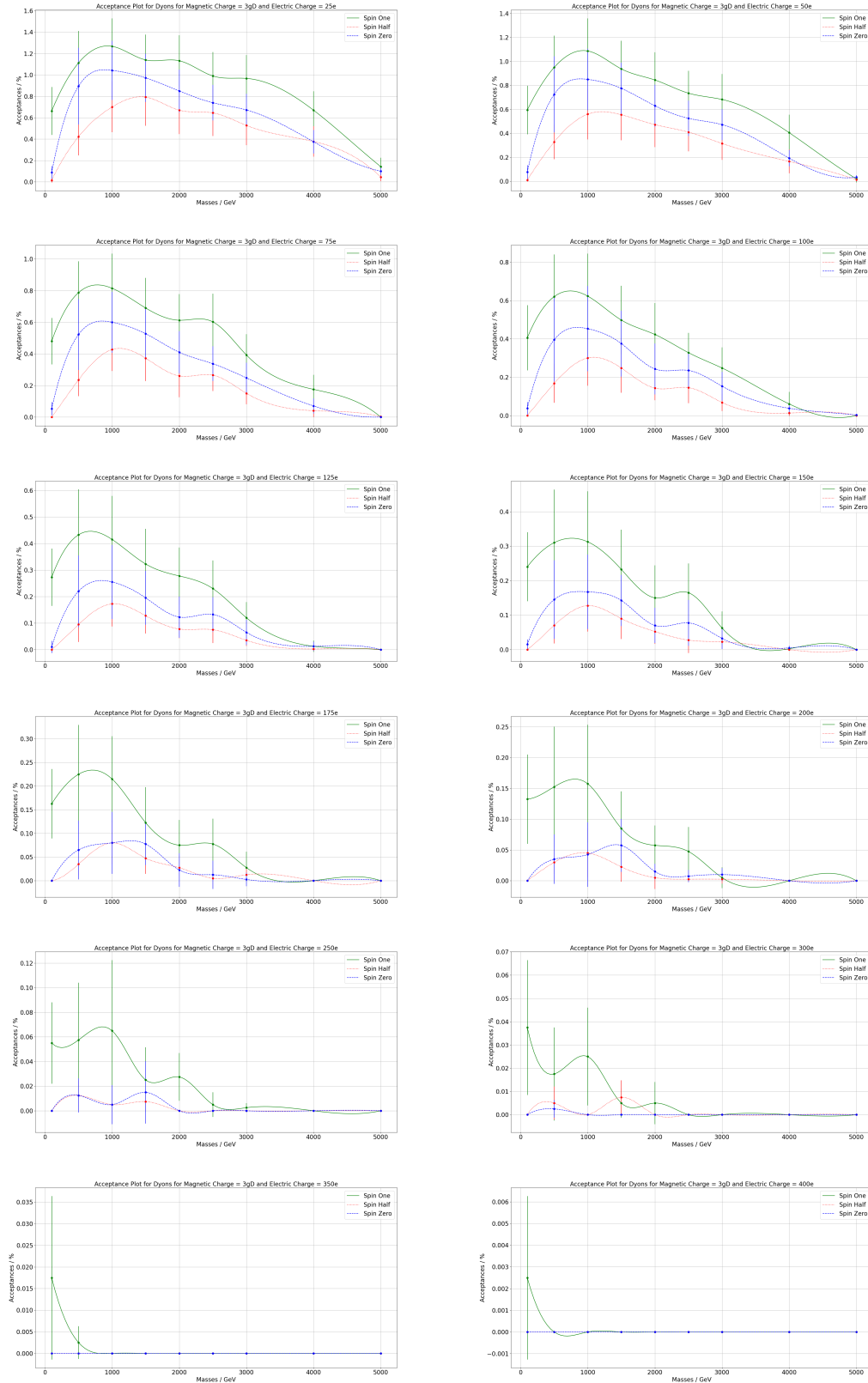
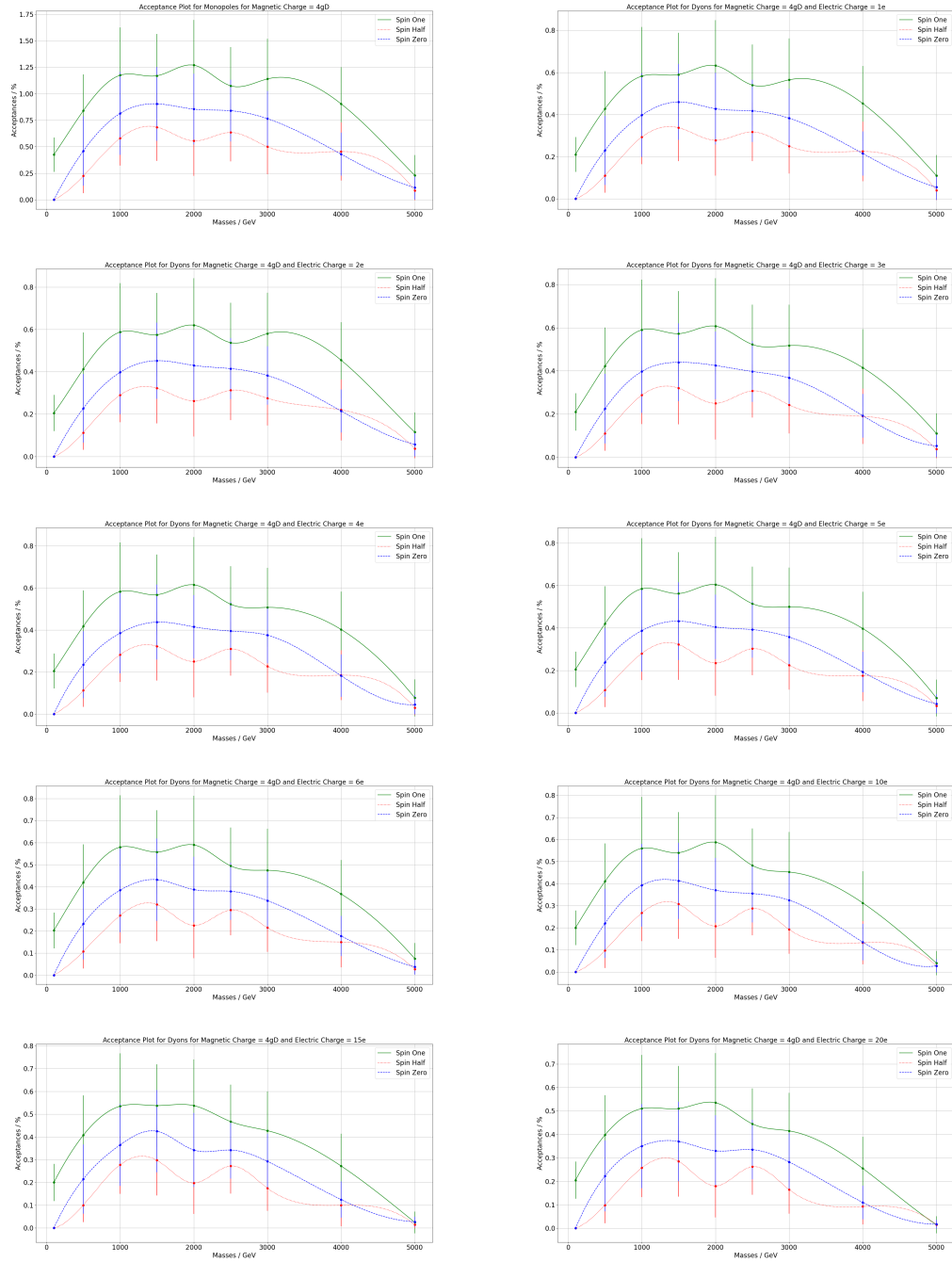


Figure 5.9: Run-2 Dyon Acceptance Plots for Magnetic Charge  $3g_D$  and Electric Charges  $25e - 400e$



**Figure 5.10:** Run-2 Dyon Acceptance Plots for Magnetic Charge  $4g_D$  and Electric Charges  $0e - 20e$

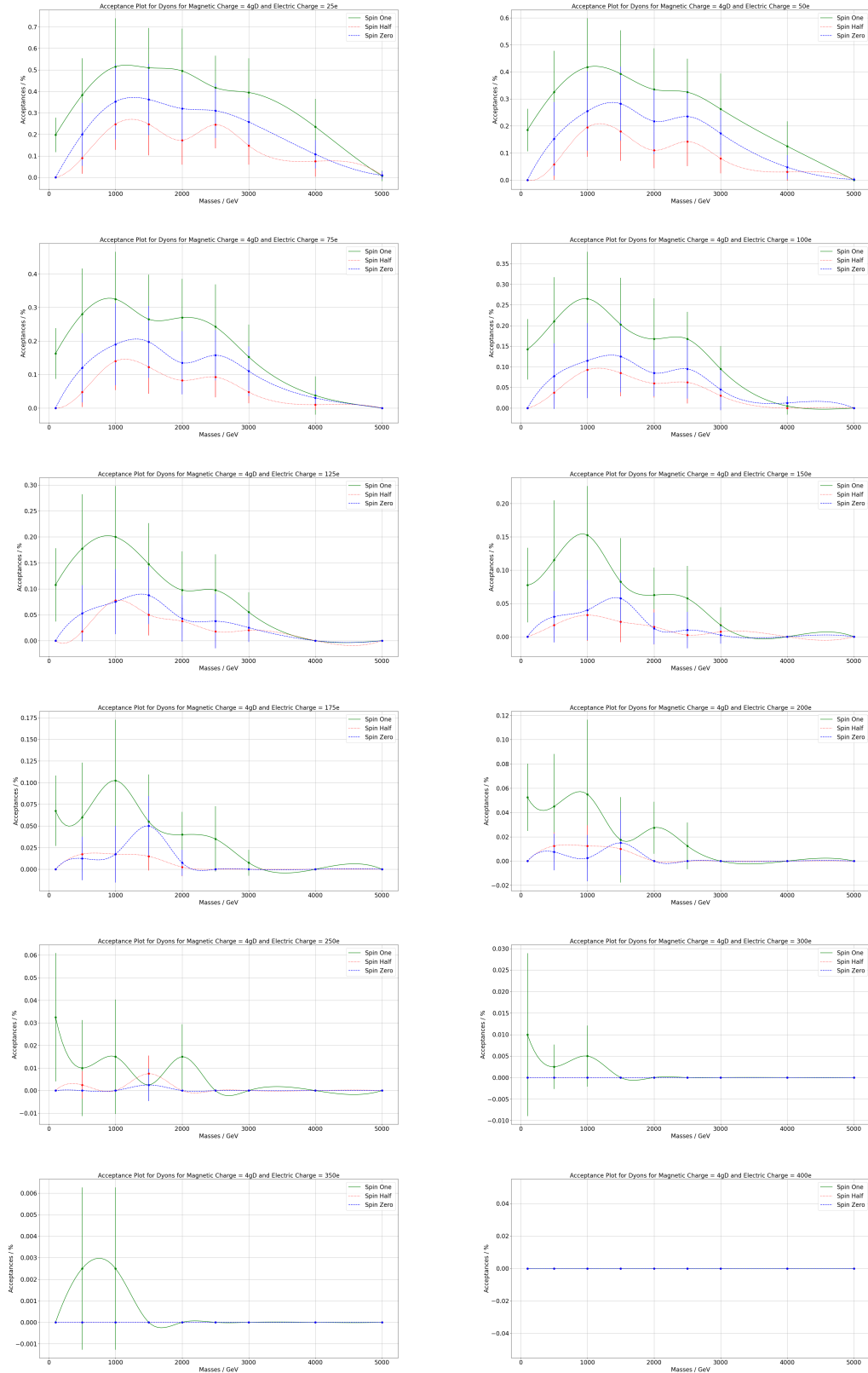
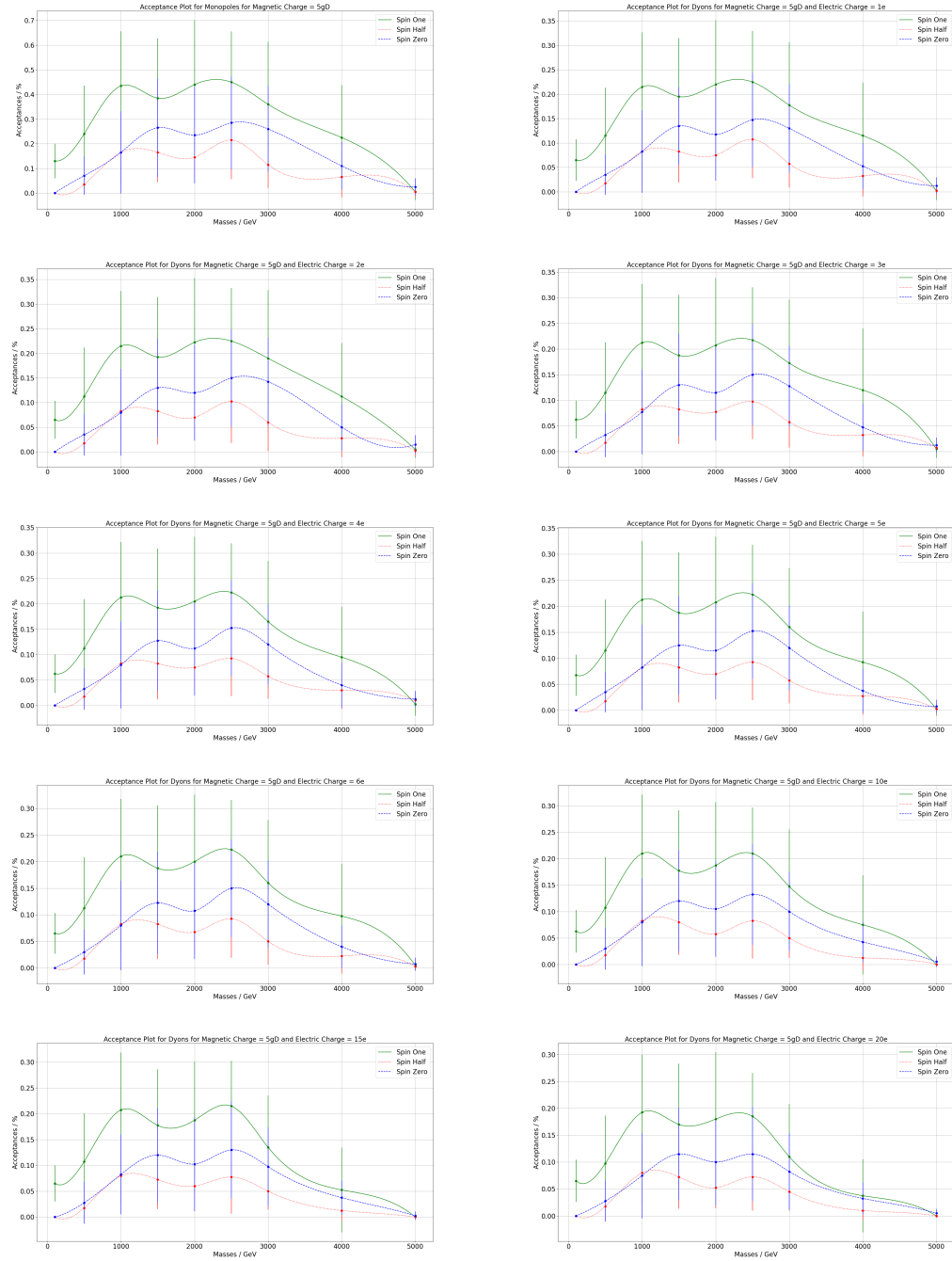
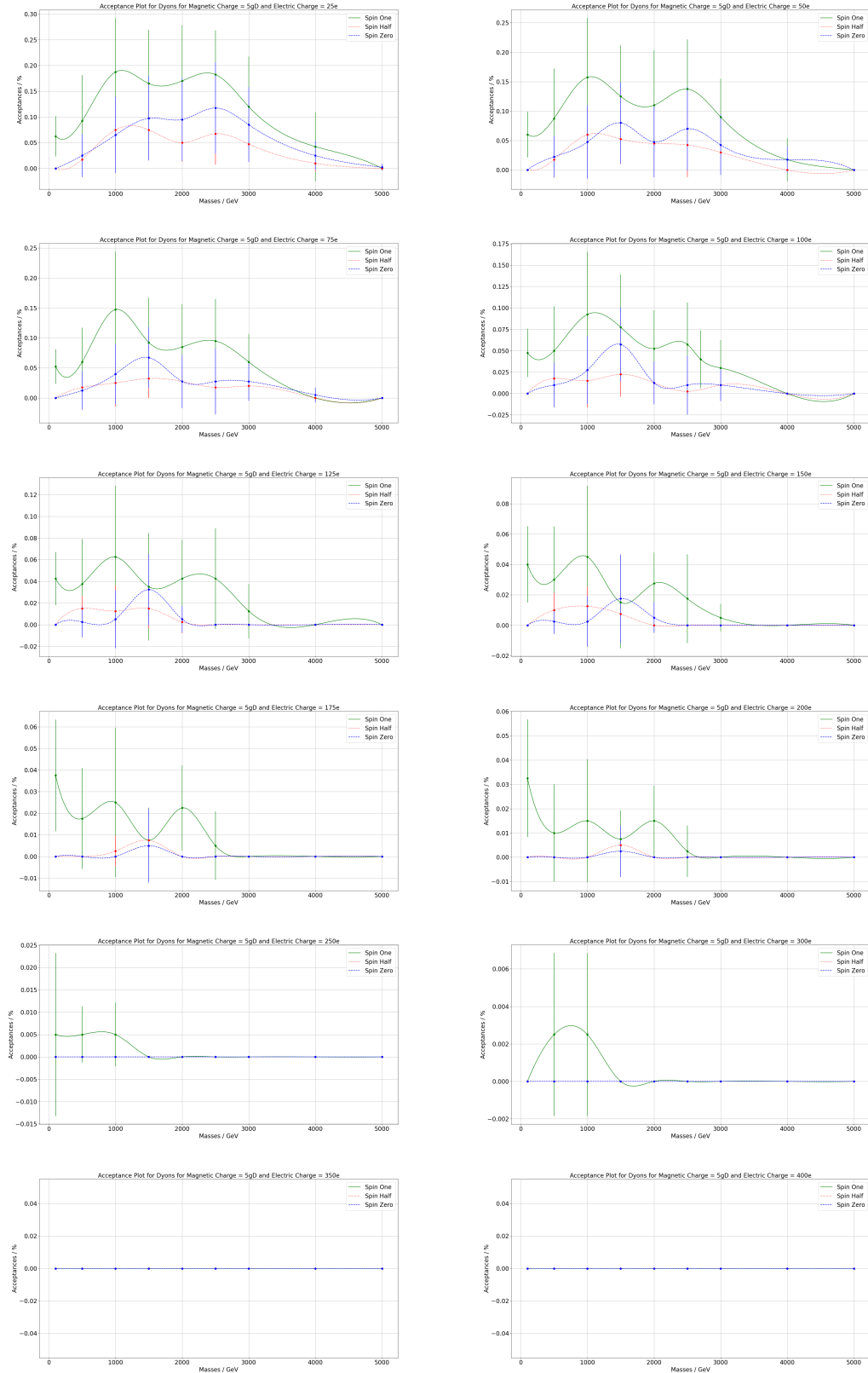


Figure 5.11: Run-2 Dyon Acceptance Plots for Magnetic Charge  $4g_D$  and Electric Charges  $25e - 400e$



**Figure 5.12:** Run-2 Dyon Acceptance Plots for Magnetic Charge  $5g_D$  and Electric Charges  $0e - 20e$



**Figure 5.13:** Run-2 Dyon Acceptance Plots for Magnetic Charge  $5g_D$  and Electric Charges  $25e - 400e$

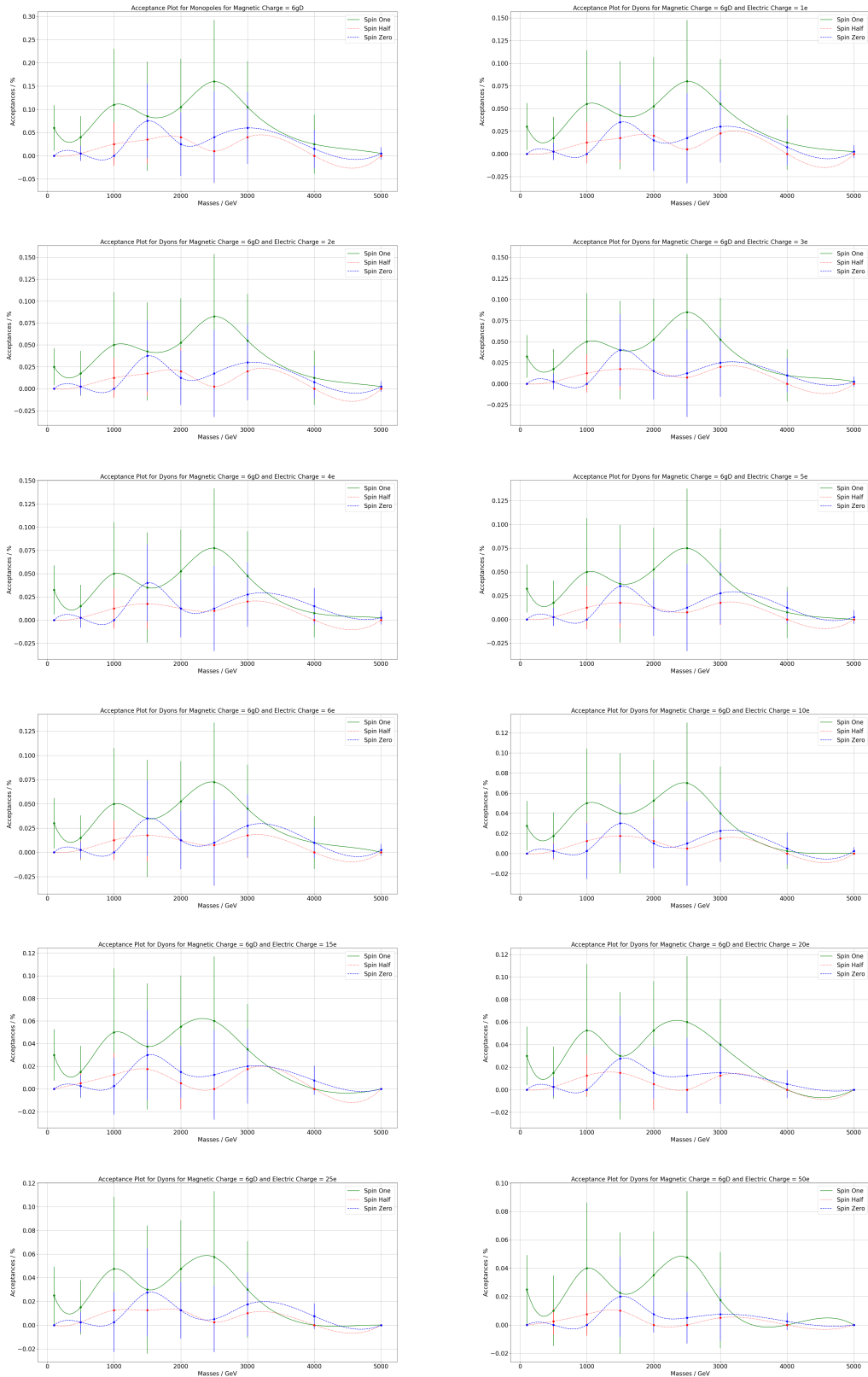


Figure 5.14: Run-2 Dyon Acceptance Plots for Magnetic Charge  $6g_D$  and Electric Charges  $0e - 50e$